Plasmonic enhancement of one-photon- and two-photon-excited single-molecule fluorescence by single gold nanorods

Zhang, W.

Citation

Zhang, W. (2018, June 27). *Plasmonic enhancement of one-photon- and two-photon-excited single-molecule fluorescence by single gold nanorods*. *Casimir PhD Series*. Retrieved from https://hdl.handle.net/1887/62864

Author: Zhang, Weichun
Title: Plasmonic enhancement of one-photon- and two-photon-excited single-molecule fluorescence by single gold nanorods
Date: 2018-06-28

Plasmonic Enhancement of One-Photon- and Two-Photon-Excited Single-Molecule Fluorescence by Single Gold Nanorods

Proefschrift

ter verkrijging van
de graad van Doctor aan de Universiteit Leiden,
op gezag van Rector Magnificus prof. mr. C.J.J.M. Stolker,
volgens besluit van het College voor Promoties
te verdedigen op woensdag 27 juni 2018
klokke 16:15 uur

door

Weichun Zhang

geboren te Anhui, China
in 1989

Promotor:

Prof. dr. M. A. G. J. Orrit	Universiteit Leiden

Copromotor:

Dr. M. Caldarola	Universiteit Leiden

Promotiecommissie:

Prof. dr. E. R. Eliel	Universiteit Leiden
Prof. dr. T. Schmidt	Universiteit Leiden
Prof. dr. E. Bouwman	Universiteit Leiden
Prof. dr. M. Lippitz	Universität Bayreuth
Prof. dr. H. Zhang	Universiteit van Amsterdam
Dr. M. J. A. de Dood	Universiteit Leiden

Keywords: Gold nanorods, surface plasmon resonance, fluorescence, single molecules, electrochemistry, two-photon, quantum dots

Printed by: Gildeprint

Front & Back: Photograph by Yang Hong.

Casimir PhD Series, Delft-Leiden 2018-20

ISBN 978-90-8593-349-6

The present work is financially supported by the Netherlands Organization for Scientific Research (NWO). The author acknowledges a Ph.D. grant from the China Scholarship Council.

Contents

1

Introduction

In this chapter, we introduce the fundamental physics involved in the thesis and the motivations of the current studies. It includes a general introduction on linear and nonlinear fluorescence, and fluorescence enhancement using plasmonics nanostructures with the focus on gold nanorods. Finally, we give an outline of the different chapters in this thesis.

1.1. Light absorption and emission

The emission of ultraviolet, visible or infrared photons from an electronically excited species is called luminescence. The excitation energy can be from chemical reactions, electric energy, light, *etc*. If the excitation is achieved by absorption of photons, the subsequent emission is then called photoluminescence. Natural materials that show photoluminescence include minerals and tissues in plants and animals. Nowadays, artificial photoluminescence materials with superior optical performances are synthesized and widely used in photoluminescence-based applications. These materials present high emitting brightness, a broad variety of colors, and good bio-compatibility. Prominent examples include synthetic organic dyes, semiconductor nanocrystals (quantum dots), and fluorescent proteins. They have become dispensable tools for biological and analytical chemical studies. In the following, we will describe in detail the processes involved in the generation of photoluminescence, with a focus on that from organic dyes.

1.1.1. Jablonski diagram

Light absorption and emission by a molecule in solution involve the electronic transition to an excited state S_1 and the subsequent relaxation to the ground state S_0. The relevant processes are schematically illustrated by a Jablonski diagram shown in Fig. 1.1. The electronic transition can be promoted in a few different ways, which will be elaborated later. The excited state can be deactivated to the ground state by emitting a photon in a time scale of sub-nanosecond to $\sim$ 10 ns for typical dye molecules. This photon emission is called fluorescence. However, not every electronic transition results in a photon emission. Other relaxation pathways compete with the fluorescence emission process, making the quantum yield (QY) of light emission less than unity. For example, the excited state energy can be dissipated as heat through nonradiative decay. Alternatively, the excited molecule can interact with another molecule to transfer energy (thereby quenching the fluorescence) or go to the lowest excited triplet state (T_1) via intersystem crossing. The sum of the decay rates of all the deactivation pathways defines the excited state lifetime.

The triplet state T_1 , which has typically microsecond lifetime, is usually a dark state at room temperature, namely, the decay from T_1 to S_0 is nonradiative. Therefore, the molecule may enter a nonfluorescent state periodically, a phenomenon known as fluorescence blinking. (At low temperature, the triplet state can also be deactivated radiatively, a process called phosphorescence. Fluorescence and phosphorescence are particular cases of luminescence.) After an internal relaxation in the ground state, the molecule is ready for another absorption-emission cycle. Most fluorophores can repeat the excitation and emission cycle many times. However, the excited states (especially the triplet excited state) are more reactive with the surrounding which can result in photobleaching: the molecule is permanently transformed and becomes unable to fluoresce. The characteristic on-off blinking and one-step blinking are important criteria to identify single molecules in single-molecule studies, which will be discussed later.

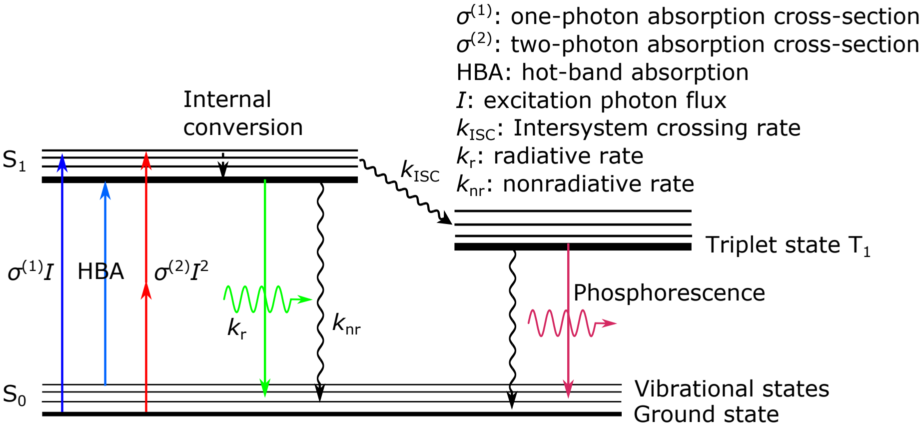

Figure 1.1: **Jablonski diagram** depicting the electronic states involved in the process of light absorption and emission.

1.1.2. One-photon-excited fluorescence

In the simplest and most conventional case, optical excitation is achieved by absorbing one single photon. Depending on the energy of the excitation photon, the molecule may be excited to higher vibration levels of the S_1 state or even to the S_2 state. The excitation rate is a linear function of the excitation photon flux I ($\text{cm}^{-2}\ \text{s}^{-1}$) in the weak excitation range below saturation, *i.e.*, $k_{\text{exc}}^{(1)} = \sigma^{(1)} I$, where $\sigma^{(1)}$ is the one-photon absorption cross-section ($\sim 10^{-16}$ cm^2 for most dyes). After excitation, the molecule relaxes to the lowest energy level of the relaxed S_1 state via a rapid ($< 10^{-12}$ s) nonradiative internal conversion. Afterwards, fluorescence is emitted from the lowest level of S_1 state irrespective of the excitation wavelength. Therefore, the emission spectra of fluorophores are usually independent of the excitation wavelength. Also, the emission is at longer wavelengths than the excitation photon because of the energy dissipation in vibrational relaxation in both the excited and ground states.

1.1.3. Two-photon-excited fluorescence

Fluorophores can also be excited by the simultaneous absorption of two photons, each with lower energy than that required for one-photon excitation, as depicted in Fig. 1.1. No intermediate states are involved. The selection rules for two-photon absorption (TPA) are different from those of for one-photon absorption, therefore the molecules may be excited to different excited states. However, the molecules emit from the lowest level of the S_1 state, independent of one- or two-photon absorption. All the molecules examined to date display the same emission spectra and lifetimes as if they were excited by one-photon absorption [1].

The first theoretical analysis of TPA dates back to 1930s when Maria Goeppert-Mayer predicted TPA in her doctoral dissertation. But it was only 30 years later that TPA was experimentally demonstrated, largely thanks to the invention of lasers. Due to the requirement of the nearly simultaneous absorption ($\sim 10^{-16}$ s) of two photons [2], the probability of occurrence of TPA is low, *i.e.*, the cross-section of TPA ($\sigma^{(2)}$) is low. Nowadays, femtosecond lasers are commonly used in conjunction with tight focusing geometries for TPA. The high peak energy of femtosecond lasers ensures a large number of excitation photons to achieve fluorescence emission from two-photon absorption.

Since the establishment of the first two-photon microscope in 1990 [3], the application of two-photon fluorescence in biological fields has been growing rapidly because of its advantages over one-photon fluorescence [2–6]. The emission spectrum of TPA is identical to one-photon fluorescence, but the excitation is at a longer wavelength than the emission, usually in the near-infrared region. Therefore, two-photon excitation is particularly suited for *in vivo* imaging due to the low absorption, autofluorescence and scattering of tissues in this wavelength range allowing for deep-tissue imaging (down to a few hundred micrometers). For TPA, the excitation rate is proportional to the squared incident light intensity, *i.e.*, $k_{\mathrm{exc}}^{(2)} = \sigma^{(2)} I^2$, where $\sigma^{(2)}$ is the two-photon absorption cross-section in terms of GM (Coppert-Mayer) units (1 GM = 10^{-50} $\mathrm{cm}^4 \mathrm{s}\ \mathrm{photon}^{-1}$). (The $\sigma^{(2)}$ of common dyes is in the range of 1 - 300 GM [7–9]. There have been efforts to synthesize fluorescent molecules with higher two-photon absorption cross-sections. There is a growing literature on fluorophores with $\sigma^{(2)}$ values higher than 1,000 GM [10–14]. Semiconductor quantum dots usually have much higher $\sigma^{(2)}$ values (> 10^4 GM) [15].) As a consequence of the nonlinear response, excitation is confined to a small volume near the focal point. This leads to inherent sectioning without the need of using additional optical elements (*e.g.* a pinhole) to reject the out-of-focus emission, which leads to higher light collection efficiency. Additionally, photobleaching and photodamage are then localized to the focal plane, which may allow imaging of living specimens over longer time periods than one-photon excitation, where photobleaching and photodamage occur across the entire thickness.

1.1.4. Hot-band absorption induced anti-Stokes luminescence

In this thesis, we also studied a special kind of light excitation termed hot-band absorption, which was first observed in 1928 [16]. A molecule can be excited from a thermally populated high vibration energy level ("hot band") by photons with longer wavelength (lower energy) than the emission wavelength to reach the excited state. The molecule then decays from the excited state back to the ground state in a same manner as in normal fluorescence. Consequently, the emission profile is the same as common fluorescence. Like two-photon fluorescence, hot-band absorption induced luminescence has anti-Stokes shift from the excitation wavelength, but hot-band absorption is a linear process. No ultrafast laser is required. From the energy conservation point of view, the additional energy is provided by the thermal energy originated from the original Boltzmann distribution of the dye molecules.

1.2. Single-molecule fluorescence spectroscopy

As discussed above, fluorescence is emitted at a different wavelength than the excitation photons. Moreover, fluorescence emission is generally a much slower process than Rayleigh or Raman scattering, which occurs on a femtosecond scale. Therefore, fluorescence signals can be well separated from background in both the time and frequency domains. These properties grant fluorescence microscopy high contrast and sensitivity. Fluorescence is capable of selectively detecting exceedingly low concentrations of molecules, down to the single-molecule level.

The first single-molecule fluorescence detection was demonstrated by Orrit and Bernard in 1990 [17] in cryogenic solids. It marked a major breakthrough in the field of optics. It greatly extended the scope of fluorescence microscopy, providing unprecedented insights into complex systems where static and dynamic heterogeneity is present [18–20]. Single fluorescent molecules are nano-scale probes for studying soft matter systems and biological mechanisms, revealing molecular dynamics with an unprecedented level of detail that may otherwise be buried in ensemble averaging in conventianal bulk measurements. Since its invention, single-molecule spectroscopy has led to several break-throughs in fundamental studies of physical and chemical phenomena and biological processes controlled by macromolecules [21], such as RNA folding [22] and protein folding [18, 23].

1.3. Plasmonic nanoantennas and fluorescence enhancement

Current single-molecule spectroscopy studies mostly rely on the high contrast against background provided by fluorescence. It is therefore highly desired to have fluorophores with emission intensities as high as possible. The emission of an overwhelming majority of absorbers, however, can be extremely weak if non-radiative relaxation is much faster than spontaneous emission of the excited state, or if the transition is nearly forbidden, as happens in lanthanide ions. Compared with one-photon-excited fluorescence, two-photon and hot-band absorption materials are typically weaker emitters due to the lower absorption probabilities. The aim of the current study is to increase the emission of weak emitters by exploiting the localized surface plasmons of metallic nanoparticles. Weak emitters will then be bright enough to be detected and studied individually. We can thus generalize single-molecule fluorescence spectroscopy to weakly emitting species which are currently undetectable by conventional single-molecule techniques.

1.3.1. Localized surface plasmons

When the size of the metal is of the order of the wavelength of light, localized surface plasmons (LSPs) occur. LSPs are collective oscillations of conduction electrons in metallic nanoparticles. The system is analogous to a damped harmonic oscillator with a resonance eigenfrequency. If the excitation frequency is in resonance with the eigenfrequency of the system, the oscillation of the conduction electrons reaches a resonance known as localized surface plasmon resonance (LSPR). The LSPR can be directly excited by visible light and leads to strong absorption and scattering of the metal nanoparticle. The LSPR of metal nanoparticles (primarily gold and silver) of various morphologies has attracted much scientific attention [24–29] because it gives rise to remarkable optical properties and applications in many areas, including imaging [30], (bio-)sensing [31], and photothermal therapy [32–34].

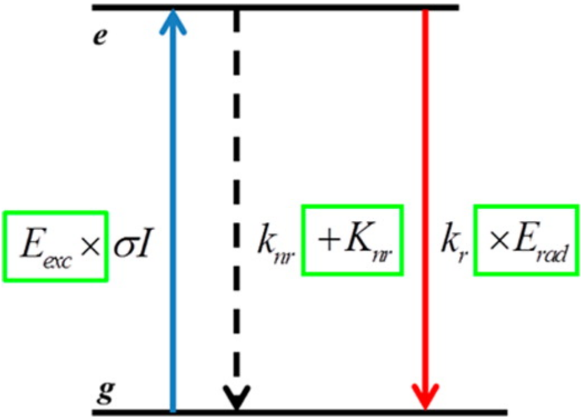

Figure 1.2: Simplified Jablonski diagram describing the transition rates of a molecule without and with (changes highlighted in green boxes) a nanoantenna. Reprinted from Ref. [39]

1.3.2. Fluorescence enhancement

It is well known that the emission rate of a quantum emitter (that emits only one photon at a time, *e.g.* a molecule or a quantum dot) is highly dependent on the local environment. Particularly, plasmonic nanoparticles (*e.g.* nanospheres, nanoshells and nanorods) have been used to work as nanoantennas to enhance the emission of adjacent emitters. See a good review on this topic [35]. As depicted in Fig. 1.2, considering a two-level model, such an enhancement involves a combined effect of three different near-field interactions between the emitter and the nanostructure [36, 37]. (i) Firstly, the excitation rate k_{exc} is increased because of the highly concentrated electromagnetic intensity at the vicinity of the nanoparticle. This part of enhancement is known as excitation enhancement E_{exc}. For one-photon excitation, the excitation rate enhancement is proportional to the enhancement of the local field intensity, while for two-photon excitation, the relation is quadratic. (ii) Secondly, plasmonic nanostructures enhance the spontaneous radiative rate (k_{r}) of neighboring emitters via the Purcell effect, leading to an increased spontaneous emission [38]. This contribution is called radiative enhancement (E_{rad}). (iii) Finally, the fluorescence may be quenched by energy transfer to dark modes of the nanoparticle and eventually converted to Ohmic heat in the metal. In other words, the nanoparticle opens up additional non-radiative decay pathways (K_{nr}) for the emitter.

The overall enhancement is a result of the complicated interplay between the three factors. Under weak excitation well below saturation, the overall enhancement is expressed as [39]

$$E_{\mathrm{all}} = E_{\mathrm{exc}} E_{\mathrm{rad}} \frac{k_{\mathrm{r}} + k_{\mathrm{nr}}}{k_{\mathrm{nr}} + K_{\mathrm{nr}} + E_{\mathrm{rad}} k_{\mathrm{r}}}.$$

E_{all} strongly depends upon the shape of nanoantennas, the emitter's position and orientation with respect to the antenna, and the overlap of its emission spectrum with the resonance of the antenna. Therefore, widely varying fluorescence enhancement dynamics have been reported for different emitter-nanoantenna systems [40–44].

1.3.3. Gold nanorods

Gold nanorods as plasmonic nanoantennas

Among many types of metallic nanoparticles, wet-chemically synthesized gold nanorods are the most extensively explored. They can be fabricated in a cheap way without the need of lithography or deposition equipments. A typical image of gold nanorods measured with scanning electron microscopy is presented in Fig. 1.3(a). Gold nanorods have relatively simple and well-defined morphology, which makes them easy to model and understand. Nanorods have two primary plasmonic modes: the transverse mode, where the plasmon oscillation occurs perpendicular to the major axis of the nanoparticle, and the longitudinal mode, where the plasmon oscillation is parallel to the major axis of the nanoparticle. Which of the modes is excited is determined by the alignment of the nanorod with the polarization of the incident light and the wavelength. The longitudinal LSPR is at a longer wavelength and more intense than the transverse LSPR and thus more often used [25].

Nanorods' narrow and strong longitudinal LSPR benefiting from the single-crystalline structure contribute to high fluorescence enhancement. Figure 1.3(c) shows the electric field intensity map around a nanorod whose longitudinal LSPR is excited. Strong electric field is concentrated at the tips of the nanorod. Moreover, the longitudinal LSPR is sensitive to the nanorod shape. Figure 1.3(b) shows the aspect-ratio (AR) dependence of the longitudinal LSPR. As the AR increases, the longitudinal LSPR becomes more intense and shifts from visible to near-infrared. This provides valuable parametric flexibility to study the plasmon-fluorophore system, *e.g.*, one can select the suited nanorods according the fluorophore for the best enhancement. Compared to nanogap antennas, such as bow-ties, dimers or particles on mirror, nanorods present a more open near field, which can accommodate molecules of various sizes. Important for biotechnological applications, gold nanorods are nontoxic and biocompatible [45]. Moreover, the gold surface has high reactivity towards thiol-modified molecules, allowing convenient chemical functionalization. For these advantages, we use gold nanorods to enhance fluorescence throughout the thesis. Systematic studies and precise understanding of the interaction of quantum emitters with such a simple yet versatile structure as a gold nanorod are of general fundamental interest and will ultimately lead to design strategies for optimizing molecular fluorescence enhancement.

Photoluminescence from gold nanorods

Benefiting from the presence of the LSPR, apart from strong absorption and scattering, gold nanoparticles also exhibit intense photoluminescence emission. Bulk gold is a very poor light emitter with an emission quantum yield (QY) of $\sim 10^{-10}$, as first discovered by Mooradian [46] in 1969. The weak luminescence originates from the creation of an electron-hole pair in the 5d and 6sp bands of bulk gold. Gold nanoparticles, however, show dramatically increased luminescence emission by the plasmon resonance. It is generally thought that such an increase is a result of a plasmon resonance coinciding with the difference between d-band and sp-band energy levels, increasing the radiative decay rate and therefore increasing the emission quantum yield [47, 48]. The typical quantum yield is in the order of $\sim 10^{-6}$ for gold nanorods [49], several orders of magnitude lower than organic dyes (QY $\sim 10^{-1}$). Photoluminescence emission is further amplified by the large absorption cross-section in the order of $10^{-2}\mu\text{m}^2$, 6 orders of magnitude higher than typical fluorescent molecules.

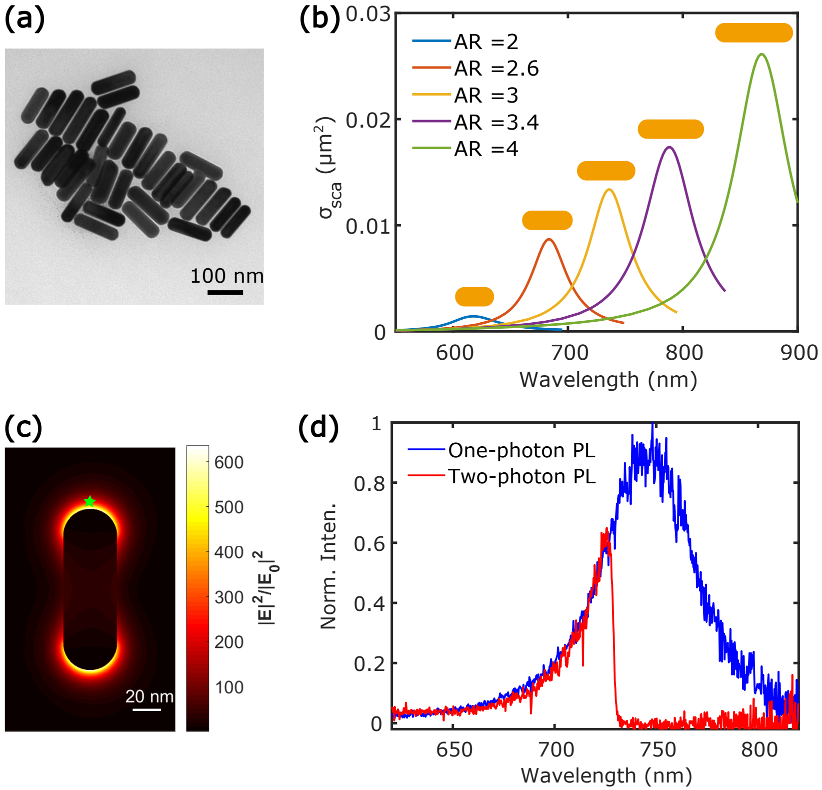

Figure 1.3: **Properties of gold nanorods**. (a) Scanning electron microscopy (SEM) image of gold nanorods. (b) Size dependence of the longitudinal surface plasmon resonance of gold nanorods. The solid lines in different colors plot the calculated (using a discrete dipole approximation method) scattering spectra for gold nanorods of various aspect ratios (ARs) immersed in water. The longitudinal resonance peak shifts to longer wavelengths by increasing the length while keeping a constant diameter of 25 nm. (c) Calculated (using a finite-element method) electric field intensity profile around a 38 nm × 114 nm nanorod in water excited by a circularly polarized plane wave of 775 nm. The green star represents an optical emitter located in the near field of the nanorod. (d) One-photon- and two-photon-excited luminescence spectra measured on a same single gold nanorod immobilized on a glass coverslip and immersed in methanol. Only the blue wing of the two-photon spectrum is present due to a shortpass filter used to cut the excitation laser (775 nm). The spectra have been corrected for the wavelength-dependent response of the optical setup. PL = photoluminescence. See Chapter 4 for the details.

Therefore, the photoluminescence brightness of a gold nanoparticle is comparable with that of a good fluorescent dye molecule.

Due to the plasmonic nature of photoluminescence from gold nanoparticles, the emission spectrum will be particularly enhanced for frequencies around the plasmon resonance. Indeed, previous research has already shown a good resemblance between the luminescence and the scattering spectra of gold nanoparticles [49]. Therefore, throughout this thesis we characterize the plasmon resonance of gold nanorods by measuring the photoluminescence spectra by exciting the interband transition and the transverse plasmon resonance at 532 nm instead of more commonly used scattering spectra. Figure 1.3 (d) shows a typical luminescence spectrum from a single gold nanorod excited by a 532-nm continuous-wave laser.

Photoluminescence of nanoparticles can be excited by both linear and nonlinear absorption. Two-photon- and multi-photon-excited luminescence have been demonstrated by using ultrafast lasers [50–54]. Figure 1.3 (d) shows a typical two-photon luminescence spectrum from a single gold nanorod excited by a 775-nm femtosecond laser. The luminescence from the gold nanorod is usually a background when studying the fluorescence enhancement effect of gold nanorods on fluorescent molecules or quantum dots.

Photothermal reshaping of anisotropc nanoparticles

Since metal nanoparticles have a very low quantum yield, the absorption of light leads to the heating of the nanocrystal, which is known as a photothermal effect. By exciting a nanoparticle at its plasmon resonance, a lot of energy can be absorbed and transformed into heat, and subsequently lead to a high temperature increase for the nanoparticle [55]. Much higher lattice temperature can be reached when the particle is heated by femtosecond laser pulses. The reason is that on longer time scales the nanoparticle starts to exchange its energy with the surroundings and thereby cools itself down [56]. As a consequence, when a femtosecond laser is used to study anisotropic nanoparticles, a major concern is the shape instability of the nanoparticles. At elevated temperatures, anisotropic nanoparticles will transform towards their thermodynamically stable shapes, which are truncated octahedrons determined by the so-called Wulff construction, through surface atom diffusion. Typically, it was found that the reshaping of anisotropic nanoparticles happens at temperatures below the bulk melting point [57–60].

For our applications of gold nanorods for fluorescence enhancement, photothermal reshaping is undesired because when a nanorod deforms towards a more spherical shape its plasmonic properties are lost and the enhancement effect is ruined. Figure 1.4 that the LSPR of a nanorod blue-shifts by 10 nm after irradiated by a femtosecond pulsed laser for 30 s. The LSPR moves farther away from the excitation wavelength, thus the local field is weakened. Severe photothermal reshaping of gold nanorods under ultrafast laser irradiation limits the laser intensity one could use to illuminate molecules and thus limits the number of photons one could collect from single molecules. It makes enhancing two-photon-excited fluorescence much more difficult than enhancing one-photon fluorescence.

1.4. Outline of the thesis

The topic of this thesis is fluorescence enhancement by gold nanorods. In the first part (Chapters 2 to 4), we focus on the enhancement of conventional one-photon-excited fluo-

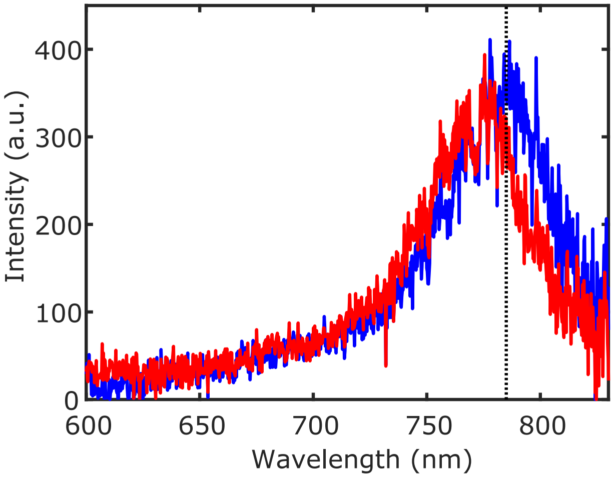

Figure 1.4: **Photothermal reshaping of a gold nanorod**. The blue curve shows the original photoluminescence spectrum ($\lambda_{\text{exc}} = 532$ nm) of a gold nanorod. The nanorod is immobilized on a glass coverslip and immersed in methanol. After irradiated by a femtosecond pulsed laser (785 nm, 6.2 kW/cm^2) for 30 s, the resonance wavelength of the nanorod blue-shifts (red curve) and becomes 10 nm farther away from the excitation wavelength. The dashed vertical line represents the laser wavelength.

rescence and applications. In the second part (Chapters 5 and 6), we work on enhancing nonlinear two-photon-excited fluorescence and luminescence.

Chapter 2. In the studies of interactions between single molecules and metal nanostrctures, reliable and efficient experimental strategies to place the molecule of interest at the right position with respect to the nanostructure with nanometer accuracy are highly desired. In this chapter, we use the free diffusion of single molecules and reversible hybridization of complementary short DNA oligomers (transient binding) as the positioning approach to visualize single-molecule enhancement events. We examine the reliability and photostability of two variants of the transient-binding strategy. We find 3,500-fold fluorescence enhancement of single molecules of IRDye800CW, a near-infrared dye with a low quantum yield of 7%, using single gold nanorods. We also perform numerical simulations for the molecule-nanorod system, which predict consistent enhancement with the experiment.

Chapter 3. This chapter demonstrates an application of fluorescence enhancement. In this chapter, we demonstrate single-molecule electrochemical measurements of the famous redox-sensitive dye Methylene Blue (QY = 4%). Observation of single molecules immobilized on the glass substrate are enabled by the fluorescence enhancement provided by isolated single gold nanorods. The redox state of a single molecule can thus be read out in real time by observing the fluorescence of the molecule as Methylene Blue is fluorescent in the oxidized state and non-fluorescent in the reduced state. Fluorescence blinking induced by redox-state turnovers was studied at different redox potentials on a *same* molecule. The on-off times are found to follow the Nernst equation, through which the mid-point potential of each individual single molecule can be determined.

Chapter 4. In this chapter, gold nanorods are used to enhance anti-Stokes luminescence of single molecules. The studied anti-Stokes luminescence is a linear optical process where a molecule is excited to the excited state from a vibrational energy level and generates radiation with shorter wavelength than the excitation wavelength. We first characterize the hot-band absorption induced anti-Stokes luminescence of a squaraine dye Seta 670. We then use single gold nanorods to enhance the anti-Stokes luminescence of single Seta 670 molecules and obtain an enhancement factor of 350. Here we rely on the transient sticking of molecules onto the glass substrate to visualize enhancement events.

Chapter 5. In marked contrast to the comprehensive efforts on enhancing the conventional one-photon-excited fluorescence, much fewer attempts have been reported on enhancing two-photon-excited fluorescence/luminescence. Two-photon-excited emission is expected to display much larger signal enhancement since it is proportional to squared intensity of the local electric field. Enhancing two-photon emission is apparently very interesting because of all the advantages and wide-spread applications of two-photon microscopy. However, it turns out much more challenging to enhance two-photon-excited fluorescence of single molecules. The main obstacle is the low emission brightness of common fluorescent dyes, leading to an inadequate number of photons detectable from a single molecule, even if the molecule is close to a gold nanorod. Photothermal reshaping of gold nanorods under ultrafast laser irradiation limits the laser intensity one could use to illuminate molecules. To circumvent this difficulty, in this chapter, we choose to enhance the two-photon-excited luminescence of single quantum dots, which are much brighter with typically three orders of magnitude higher two-photon absorption cross-sections than normal dye molecules. We demonstrate two-photon-excited luminescence enhancement of more than four orders of magnitude for single quantum dots transiently stuck near a single nanorod. We also perform numerical simulations to verify the observed enhancement. The good consistency between simulations and measurements suggests that two-photon luminescence enhancement is not notably affected by the transient broadening of the plasmon resonance after femtosecond excitation. An electromagnetic model is adequate to describe the system.

Chapter 6. In this chapter, we demonstrate two-photon-excited fluorescence enhancement for an ensemble of Rhodamine 6G molecules. By increasing the concentration of fluorescent molecules we are able to detect enough two-photon-excited fluorescence while keeping the laser intensity below the photothermal reshaping threshold of gold nanorods. Our result shows that due to the presence of a single gold nanorod, fluorescence of the molecules in the near field is enhanced, on average, by a factor of 4,500. We find that the enhancement is independent on the excitation power, which further supports that two-photon enhancement is not affected by ultrafast plasmon broadening.

References

[1] J. R. Lakowicz, *Principles of Fluorescence Spectroscopy*, 3rd ed. (Springer US, 2006) p. 954.

[2] W. R. Zipfel, R. M. Williams, and W. W. Webb, *Nonlinear magic: multiphoton microscopy in the biosciences,* Nature Biotechnology **21**, 1369 (2003).

[3] W. Denk, J. H. Strickler, and W. W. Webb, *Two-photon laser scanning fluorescence microscopy,* Science **248**, 73 (1990).

[4] M. Pawlicki, H. Collins, R. Denning, and H. Anderson, *Two-photon absorption and the design of two-photon dyes,* Angewandte Chemie International Edition **48**, 3244 (2009).

[5] A. Diaspro and M. Robello, *Two-photon excitation of fluorescence for three-dimensional optical imaging of biological structures,* Journal of Photochemistry and Photobiology B: Biology **55**, 1 (2000).

[6] M. Rubart, *Two-photon microscopy of cells and tissue,* Circulation Research **95**, 1154 (2004).

[7] M. A. Albota, C. Xu, and W. W. Webb, *Two-photon fluorescence excitation cross sections of biomolecular probes from 690 to 960 nm,* Applied Optics **37**, 7352 (1998).

[8] A. Nag and D. Goswami, *Solvent effect on two-photon absorption and fluorescence of rhodamine dyes,* Journal of Photochemistry and Photobiology A: Chemistry **206**, 188 (2009).

[9] C. Xu and W. W. Webb, *Measurement of two-photon excitation cross sections of molecular fluorophores with data from 690 to 1050 nm,* JOSA B **13**, 481 (1996).

[10] M. Albota, D. Beljonne, J.-L. Brédas, J. E. Ehrlich, J.-Y. Fu, A. A. Heikal, S. E. Hess, T. Kogej, M. D. Levin, and S. R. Marder, *Design of organic molecules with large two-photon absorption cross sections,* Science **281**, 1653 (1998).

[11] K. Podgorski, E. Terpetschnig, O. P. Klochko, O. M. Obukhova, and K. Haas, *Ultra-bright and-stable red and near-infrared squaraine fluorophores for in vivo two-photon imaging,* PloS one **7**, e51980 (2012).

[12] O. V. Przhonska, S. Webster, L. A. Padilha, H. Hu, A. D. Kachkovski, D. J. Hagan, and E. W. Van Stryland, *Two-photon absorption in near-ir conjugated molecules: design strategy and structure–property relations,* in *Advanced Fluorescence Reporters in Chemistry and Biology I* (Springer, 2010) pp. 105–147.

[13] C.-K. Wang, P. Macak, Y. Luo, and H. Ågren, *Effects of π centers and symmetry on two-photon absorption cross sections of organic chromophores,* The Journal of Chemical Physics **114**, 9813 (2001).

[14] C.-L. Sun, Q. Liao, T. Li, J. Li, J.-Q. Jiang, Z.-Z. Xu, X.-D. Wang, R. Shen, D.-C. Bai, Q. Wang, *et al.*, *Rational design of small indolic squaraine dyes with large two-photon absorption cross section,* Chemical Science **6**, 761 (2015).

[15] D. R. Larson, W. R. Zipfel, R. M. Williams, S. W. Clark, M. P. Bruchez, F. W. Wise, and W. W. Webb, *Water-soluble quantum dots for multiphoton fluorescence imaging in vivo,* Science **300**, 1434 (2003).

[16] R. Wood, *Xxix. anti-Stokes radiation of fluorescent liquids,* The London, Edinburgh, and Dublin Philosophical Magazine and Journal of Science **6**, 310 (1928).

[17] M. Orrit and J. Bernard, *Single pentacene molecules detected by fluorescence excitation in a p-terphenyl crystal,* Physical Review Letters **65**, 2716 (1990).

[18] B. Schuler and W. A. Eaton, *Protein folding studied by single-molecule FRET,* Current Opinion In Structural Biology **18**, 16 (2008).

[19] S. Weiss, *Fluorescence spectroscopy of single biomolecules,* Science **283**, 1676 (1999).

[20] X. S. Xie and H. P. Lu, *Single-molecule enzymology,* Journal of Biological Chemistry **274**, 15967 (1999).

[21] W. E. Moerner, *New directions in single-molecule imaging and analysis,* Proceedings of the National Academy of Sciences **104**, 12596 (2007).

[22] R. Roy, S. Hohng, and T. Ha, *A practical guide to single-molecule FRET,* Nature methods **5**, 507 (2008).

[23] E. Rhoades, E. Gussakovsky, and G. Haran, *Watching proteins fold one molecule at a time,* Proceedings of the National Academy of Sciences **100**, 3197 (2003).

[24] C. F. Bohren and D. R. Huffman, *Absorption and scattering of light by small particles* (John Wiley & Sons, 2008).

[25] S. Link and M. A. El-Sayed, *Spectral properties and relaxation dynamics of surface plasmon electronic oscillations in gold and silver nanodots and nanorods,* The Journal of Physical Chemistry B (1999).

[26] P. Zijlstra and M. Orrit, *Single metal nanoparticles: optical detection, spectroscopy and applications,* Reports on Progress in Physics **74**, 106401 (2011).

[27] J. R. Lakowicz, *Plasmonics in biology and plasmon-controlled fluorescence,* Plasmonics **1**, 5 (2006).

[28] J. Pérez-Juste, I. Pastoriza-Santos, L. M. Liz-Marzán, and P. Mulvaney, *Gold nanorods: synthesis, characterization and applications,* Coordination Chemistry Reviews **249**, 1870 (2005).

[29] L. Vigderman, B. P. Khanal, and E. R. Zubarev, *Functional gold nanorods: synthesis, self-assembly, and sensing applications,* Advanced Materials **24**, 4811 (2012).

[30] S. Yao, H.-H. Cai, M. Liu, and P.-H. Yang, *Fluorescent labeling of cellular targets and multicolor imaging with gold nanorods,* Dyes and Pigments **101**, 286 (2014).

[31] P. Zijlstra, P. M. Paulo, and M. Orrit, *Optical detection of single non-absorbing molecules using the surface plasmon resonance of a gold nanorod,* Nature Nanotechnology **7**, 379 (2012).

[32] D. P. O'Neal, L. R. Hirsch, N. J. Halas, J. D. Payne, and J. L. West, *Photo-thermal tumor ablation in mice using near infrared-absorbing nanoparticles,* Cancer Letters **209**, 171 (2004).

[33] X. Huang, I. H. El-Sayed, W. Qian, and M. A. El-Sayed, *Cancer cell imaging and photothermal therapy in the near-infrared region by using gold nanorods,* Journal of the American Chemical Society **128**, 2115 (2006).

[34] X. Huang, P. K. Jain, I. H. El-Sayed, and M. A. El-Sayed, *Plasmonic photothermal therapy (pptt) using gold nanoparticles,* Lasers in Medical Science **23**, 217 (2008).

[35] J. Wenger, *Fluorescence spectroscopy enhancement on photonic nanoantennas,* arXiv preprint arXiv:1709.06749 (2017).

[36] S. Kühn, U. Håkanson, L. Rogobete, and V. Sandoghdar, *Enhancement of single-molecule fluorescence using a gold nanoparticle as an optical nanoantenna,* Physical Review Letters **97**, 017402 (2006).

[37] T. Härtling, P. Reichenbach, and L. Eng, *Near-field coupling of a single fluorescent molecule and a spherical gold nanoparticle,* Optics Express **15**, 12806 (2007).

[38] O. Muskens, V. Giannini, J. Sanchez-Gil, and J. Gomez Rivas, *Strong enhancement of the radiative decay rate of emitters by single plasmonic nanoantennas,* Nano Letters **7**, 2871 (2007).

[39] S. Khatua, P. M. R. Paulo, H. Yuan, A. Gupta, P. Zijlstra, and M. Orrit, *Resonant plasmonic enhancement of single-molecule fluorescence by individual gold nanorods,* ACS Nano **8**, 4440 (2014).

[40] A. Kinkhabwala, Z. Yu, S. Fan, Y. Avlasevich, K. Müllen, and W. Moerner, *Large single-molecule fluorescence enhancements produced by a bowtie nanoantenna,* Nature Photonics **3**, 654 (2009).

[41] D. Punj, M. Mivelle, S. B. Moparthi, T. S. van Zanten, H. Rigneault, N. F. van Hulst, M. F. Garcia-Parajo, and J. Wenger, *A plasmonic 'antenna-in-box' platform for enhanced single-molecule analysis at micromolar concentrations,* Nature Nanotechnology **8**, 512 (2013).

[42] G. Acuna, F. Möller, P. Holzmeister, S. Beater, B. Lalkens, and P. Tinnefeld, *Fluorescence enhancement at docking sites of DNA-directed self-assembled nanoantennas,* Science **338**, 506 (2012).

[43] P. Anger, P. Bharadwaj, and L. Novotny, *Enhancement and quenching of single-molecule fluorescence.* Physical Review Letters **96**, 113002 (2006).

[44] H. Yuan, S. Khatua, P. Zijlstra, M. Yorulmaz, and M. Orrit, *Thousand-fold enhancement of single-molecule fluorescence near a single gold nanorod.* Angewandte Chemie International Edition **52**, 1217 (2013).

[45] X. Nan, P. A. Sims, and X. S. Xie, *Organelle tracking in a living cell with microsecond time resolution and nanometer spatial precision,* ChemPhysChem **9**, 707 (2008).

[46] A. Mooradian, *Photoluminescence of metals,* Physical Review Letters **22**, 185 (1969).

[47] E. Dulkeith, T. Niedereichholz, T. Klar, J. Feldmann, G. Von Plessen, D. Gittins, K. Mayya, and F. Caruso, *Plasmon emission in photoexcited gold nanoparticles,* Physical Review B **70**, 205424 (2004).

[48] C. Sönnichsen, T. Franzl, T. Wilk, G. von Plessen, J. Feldmann, O. Wilson, and P. Mulvaney, *Drastic reduction of plasmon damping in gold nanorods,* Physical Review Letters **88**, 077402 (2002).

[49] M. Yorulmaz, S. Khatua, P. Zijlstra, A. Gaiduk, and M. Orrit, *Luminescence quantum yield of single gold nanorods,* Nano Letters **12**, 4385 (2012).

[50] C. Molinaro, Y. El Harfouch, E. Palleau, F. Eloi, S. Marguet, L. Douillard, F. Charra, and C. Fiorini-Debuisschert, *Two-photon luminescence of single colloidal gold nanorods: revealing the origin of plasmon relaxation in small nanocrystals,* The Journal of Physical Chemistry C **120**, 23136 (2016).

[51] H. Wang, T. B. Huff, D. A. Zweifel, W. He, P. S. Low, A. Wei, and J.-X. Cheng, *In vitro and in vivo two-photon luminescence imaging of single gold nanorods,* Proceedings of the National Academy of Sciences of the United States of America **102**, 15752 (2005).

[52] M. Eichelbaum, B. Schmidt, H. Ibrahim, and K. Rademann, *Three-photon-induced luminescence of gold nanoparticles embedded in and located on the surface of glassy nanolayers,* Nanotechnology **18**, 355702 (2007).

[53] R. A. Farrer, F. L. Butterfield, V. W. Chen, and J. T. Fourkas, *Highly efficient multiphoton-absorption-induced luminescence from gold nanoparticles,* Nano Letters **5**, 1139 (2005).

[54] P. Zijlstra, J. W. Chon, and M. Gu, *Five-dimensional optical recording mediated by surface plasmons in gold nanorods,* Nature **459**, 410 (2009).

[55] A. O. Govorov and H. H. Richardson, *Generating heat with metal nanoparticles,* Nano today **2**, 30 (2007).

[56] G. Baffou and H. Rigneault, *Femtosecond-pulsed optical heating of gold nanoparticles,* Physical Review B **84**, 035415 (2011).

[57] A. B. Taylor, A. M. Siddiquee, and J. W. M. Chon, *Below melting point photothermal reshaping of single gold nanorods driven by surface diffusion,* ACS Nano **8**, 12071 (2014).

[58] P. Zijlstra, J. W. Chon, and M. Gu, *White light scattering spectroscopy and electron microscopy of laser induced melting in single gold nanorods,* Physical Chemistry Chemical Physics **11**, 5915 (2009).

[59] W. Albrecht, T.-S. Deng, B. Goris, M. A. van Huis, S. Bals, and A. van Blaaderen, *Single particle deformation and analysis of silica-coated gold nanorods before and after femtosecond laser pulse excitation,* Nano Letters **16**, 1818 (2016).

[60] P. Buffat and J. P. Borel, *Size effect on the melting temperature of gold particles,* Physical Review A **13**, 2287 (1976).

2

Plasmonic enhancement of a near-infrared fluorophore using DNA transient binding

Fluorescence enhancement by plasmonic nanostructures enables the optical detection of single molecules with weak fluorescence, extending the scope of molecular fluorescence imaging to new materials and systems. In this work, we make use of the reversible hybridization of fluorophore-carrying short DNA oligomers to their complementary docking strands (immobilized on the surface of gold nanorods or the glass substrate) to visualize single-molecule enhancement events near individual gold nanorods. Docking strands attached to the glass substrate are found to be more photo-stable. We find over 3,000-fold fluorescence enhancement of single molecules of IRDye800CW, a near-infrared dye with a low quantum yield of 7%. This strong enhancement, consistent with numerical simulations, arises from the combined effect of local field enhancement and the competition between radiative and nonradiative decay rate enhancements.

2.1. Introduction

Noble metal nanoparticles of varous morphologies have been at the center of research (see reviews [1–6] and references therein) because of their remarkable optical properties derived from their localized surface plasmons. A wealth of applications based on plasmonic nanoparticles have been explored, such as imaging [7], (bio-)sensing [8], and photothermal therapy [9–11]. The strong local fields generated around nanoparticles upon resonant excitation can modify the interaction of neighbouring molecules with light, giving rise to diverse applications such as surface-enhanced Raman spectroscopy [12, 13] and metal-enhanced fluorescence [14–19].

In metal-enhanced fluorescence, plasmonic nanoparticles can be described as optical nano-antennas interacting strongly with fluorophores, enhancing their excitation and radiative rates, and opening new non-radiative dissipation channels (quenching), and consequently influencing their fluorescence emission [14, 15, 20]. Fluorescence enhancement of fluorophores emitting at wavelengths in the near-infrared region is of particular interest. Due to the absence of autofluorescence and deeper penetration depth under near-infrared excitation, near-infrared dyes have extensive *in vivo* applications in biosensing and molecular fluorescence bioimaging [21, 22]. Unfortunately, most biocompatible near-infrared-emitting dyes (*e.g.* Indocyanine Green) are weak fluorophores with low quantum yields [23]. Gold nanoparticles have been used to enhance the fluorescence brightness of near-infrared-emitting fluorophores by two orders of magnitude, improving significantly the detection limits of near-infrared fluorescence imaging [24–27]. At the single-molecule level, the enhancement is more pronounced because of the absence of ensemble averaging over many molecules, most of which are not in the plasmonic hot spots. If a single fluorophore is placed in the right position, plasmonic nanoparticles can enhance its fluorescence by two to four orders of magnitude upon radiation with a resonant laser [28–30]. Herein, we demonstrate that plasmonic nanoparticles enable sensitive detection of near-infrared fluorophores, even at the single-molecule level.

One of the major difficulties of studying single molecules by fluorescence enhancement is the accurate positioning of the molecule of interest with respect to the nanostructures at the nanometer scale. Different approaches were proposed, including slow free diffusion [31], non-specific transient sticking [29, 32, 33], and immobilization of single molecules [28, 30, 34–36]. The observation time of single molecules for diffusion and immobilization methods is often limited. Diffusion times in the near field are often shorter than 1 ms, making it difficult to study slower dynamics and to detect fluorescence enhancement with low photon rates. While molecules can be immobilized almost permanently close to the nanoantennas, the observation time is limited by photobleaching. Consequently, each nanoantenna can be studied with only one or a few molecules at best.

Transient binding approaches offer an elegant solution for the photobleaching problem while giving a reasonable observation time. However, non-specific sticking is dependent on many factors including the properties of the diffuser, the surrounding medium, as well as the surface conditions of the substrate, leading to an unpredictable sticking time. Here we make use of the sequence-specific and reversible hybridization of complementary DNA strands to study the fluorescence enhancement of single molecules of a near-infrared dye by an individual plasmonic nanostructure. DNA hybridization offers a reliable, reproducible and controllable mechanism for transient binding thanks to highly predictable base pairing and binding energy [37]. Reversible hybridization of short DNA strands facilitates the targeting of the surface of objects by diffusing flourorescent probes, which is the key principle of a super-resolution imaging technique known as DNA-PAINT [38–40] (points accumulation for imaging in nanoscale topography).

Similar to the idea of DNA-PAINT, we use the transient binding and dissociation of short dye-labeled DNA strands ("imager strand") in solution to their complementary target strands ("docking strands") immobilized either on the surface of gold nanorods or the glass substrate to bind fluorescent molecules in the hot spot of a nanostructure. In contrast to immobilizing fluorophores, the DNA-based strategy is limited by photobleaching because photobleached molecules are continuously replenished with fresh ones. Furthermore, the binding time of the imager strand to the docking strand can be adjusted by the electrolyte concentration, the number of complementary base pairs and the temperature. The chemistry and kinetics of DNA hybridization have been extensively characterized [38, 41].

The selected plasmonic nanostrucutre for our study is individual gold nanorods. Such nanoparticles are widely explored for several applications such as plasmonic sensing [3, 42], nanoheating [43] and for fluorescence enhancement [29, 44], as they offer narrow and tunable surface plasmon resonances (SPR) from the visible to the near-infrared "water window". They also provide highly confined nanometric volumes with easy access for molecules near their tips. Gold surfaces can be readily functionalized with thiolated molecules, taking advantage of the strong Au-S bond. Moreover they are easy to fabricate with wet-chemical methods and they can be used in solution, without the need of a supporting substrate.

We studied two different approaches to enhance the fluorescence of single molecules using DNA transient binding. i). The docking DNAs are immobilized on the nanorod surface; ii). The docking DNAs are immobilized to the glass substrate surface. We characterized the enhancement factors, the binding times, and the photo-stability. We found a maxium enhancement factor of 3,500-fold, which is in good agreement with numerical calculations.

2.2. Materials and methods

IRDye800CW molecules were used for the enhancement study. An IRDye800CW molecule is conjugated to a short oligonucleotide strand of 10 base pairs (Integrated DNA Technologies, Inc.). IRDye800CW is a near-infrared dye with a low quantum yield of 7% [25]. The absorption maximum of the imager construct (DNA plus dye) is observed at 780 nm, and the fluorescence emission maximum appears at 796 nm in HEPES buffer (Fig. 2.1(a)).

Attachment of docking strands. Clean coverslips were first functionalized with (3-mercaptopropyl)trimethoxysilane to create a thiol-terminated surface. Individual gold nanorods were adsorbed onto the functionalized surface from a dilute aqueous suspension of gold nanorods (Nanopartz Inc.). The resulting density of nanorods was limited to $6/(100\ \mu\mathrm{m}^2)$ so that there was only one nanorod in the focus of the fluorescence microscope. The average size of the nanorods was 38 nm $\times$118 nm by diameter and length. This size was chosen such that the longitudinal plasmon resonance overlaps well with both the excitation wavelength and the emission wavelength of the dye (Fig. 2.1(b)), ensuring a high fluorescence enhancement factor [29, 44].

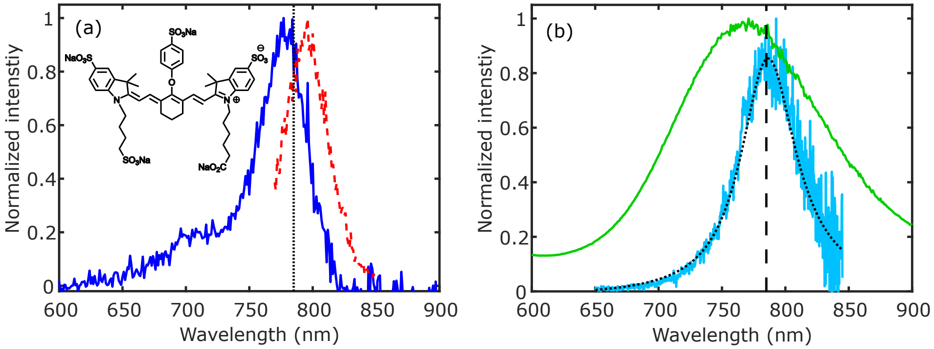

Figure 2.1: **Spectra of IRDye800CW and gold nanorods**. (a) Absorption and emission spectra of IRDye800CW conjugated with the imager DNA strand in HEPES buffer are shown as the blue solid line and red dashed line, respectively ($\lambda_{\mathrm{max-abs}} \sim 780$ nm, $\lambda_{\mathrm{max-em}} \sim 796$ nm). The absence of the shoulder in the emission spectrum corresponding to the vibronic absorption band is attributable to the low near-infrared response of the spectrofluorometer. Inset: chemical structure of IRDye800CW. (b) The green line shows the bulk extinction spectrum of gold nanorods used in this work dispersed in water. The extinction maximum was observed at 771 nm. The broad extinction band stems from the size distribution of nanorods in the suspension. The light blue curve shows the photoluminescence spectrum of a single gold nanorod. The spectrum is corrected for the wavelength-dependence collecting efficiency of the setup and fitted with a Lorentzian line shape (balck doted line), yielding a resonance wavelength of 786.4 ± 0.4 nm. The wavelength of the excitation laser (785 nm) is represented by the dashed vertical lines in the plots.

Docking DNA strands were attached, either onto the nanorod surfaces or the glass substrate, as described in detail in the Supporting Information. Briefly, to functionalize the nanorod surface with docking strands, the nanorod-loaded coverslips were treated with dithiol-derived oligonucleotides and thiol-derived polyethylene glycol (PEG-SH). The oligonucleotide contains dithiol phosphoramidite at one terminus and 15 base pairs, 10 of which are complementary to those of the imager strand. Both the oligonucleotides and PEG chains can bind to the nanorods. The ratio of docking strands and PEG molecules was kept at around 1 : 1000 to ensure only single or a few docking strands at the tips of a nanorod. The coverslip surface was further covered with bovine serumalbumin (BSA) using 4-(p-maleimidophenyl)butyrate (SMPB) as a cross-linker to minimize non-specific adsorption of the fluorophores on the surface.

To functionalize the coverslip surface with docking strands, a layer of NeutrAvidin molecules was attached to the coverslips with gold nanorods using SMPB as the linker. Biotin-terminated docking strands were then tethered to the substrate via biotin-NeutrAvidin interactions. The docking strand contains 20 base pairs, 10 of which are complementary to those of the imager strand. The coverslip surface was thus saturated with docking DNA strands that could hybridize with the imager strands while the nanorod surface had no docking strands attached. See the Supporting Information for the details of sample preparation.

Confocal microscopy. Single-molecule fluorescence enhancement studies were performed on a home-built sample-scanning microscope at room temperature. A linearly polarized diode laser (785 nm, continuous-wave, Toptica Photonics) or a circularly polarized 532-nm continuous-wave laser (532 nm, continuous-wave, Shanghai Laser & Optics Century Co., Ltd) was reflected by a 10/90 beam splitter into an oil immersion objective (100 ×, NA=1.4, Zeiss) to excite the dye molecules or to measure the photoluminescence spectra of gold nanorods. Emission from the focal volume was collected by the same objective and transmitted by the beam splitter. After the scattered light from the excitation laser was filtered out by suitable notch filters, fluorescence was focused on a multi-mode optical fiber with a core of 62 μm in diameter. The optical fiber is equivalent to a confocal pinhole. The output of the optical fiber was detected by an avalanche photodiode (SPCM-AQR-16, PerkinElmer). The setup was equipped with a spectrometer with a liquid-nitrogen-cooled CCD (Acton SP-500i, Princeton Instruments). The photoluminescence spectra were corrected for the low near-infrared response of the optics (Fig. S2.2, Supporting Information). Figure 2.1(b) shows the photoluminescence spectrum of a single gold nanorod, which shows a narrow Lorentzian spectral shape. Thus aggregates of nanoparticles can be easily recognized and excluded from further studies [45].

2.3. Results and discussion

2.3.1. Binding sites on the nanorod surface

Thiolated docking DNA strands were tethered to the surface of gold nanorods together with thiolated competitor molecules to regulate the density of binding sites. The concentration of dye-labeled imager strand was 100 nM with 500 mM NaCl in HEPES pH 7.0 buffer. NaCl provides the necessary ion strength required for the desired DNA-binding kinetics. The distance between the chromophore and nanorod surface is set by the number of base pairs in the DNA docking-imager construct. We estimated a total distance of 4 nm using an inter-base pair distance of 0.33 nm and considering the length of the linker to the gold surface.

When the 785-nm laser was focused on the individual immobilized nanorods, we recorded fluorescence time traces, which showed fluorescence bursts corresponding to transient hybridization of the imager strand to the docking strands immobilized near the tips of the nanorod. The excitation was kept at a very low power (2 nW) to minimize photobleaching of the dye molecules while detecting enough fluorescence intensity to identify transient enhancement events of single molecules.

Since the competition of binding to the gold surface between the docking strands and competitor molecules is a random process, the number and position of docking strands on the nanorod surface vary from nanorod to nanorod. Therefore, fluorescence bursts with different intensity levels may be identified on the time traces taken on different nanorods. Figure 2.2(b) shows a time trace with only one observable docking site. In such a scenario, many refreshing single molecules can be studied *at the same* position in the plasmonic hot spot, evidenced by the stable high level intensity measured. Every binding site can be measured, in theory, over unlimited period of time. This opens the study of different kinds of single molecules in the same nanoscale environment with significant statistics. With such an experimental scheme, a rich variety of single-molecule studies can be envisioned. One such example is to study the enhancement factors for molecules with different quantum efficiencies with great control over their positions with respect to plasmonic nanostructures.

The binding time of the imager to the docking strands depends on many factors including

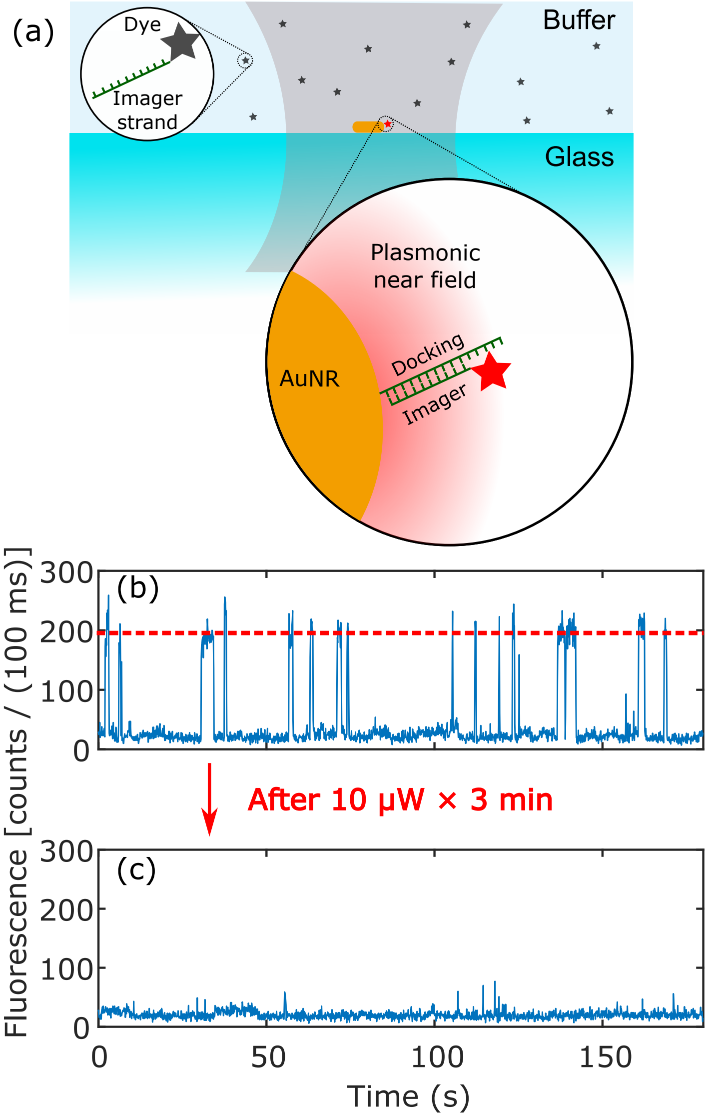

Figure 2.2: **Fluorescence enhancement with the docking strands on the nanorods**. (a) Schematic of transient binding. Immobilized nanorods are functionalized with docking strands. The imager-IRDye800CW strands in the solution are shown as gray stars representing unenhanced fluorescence. One of the imagers is hybridizing to a docking strand attached to the tip of the nanorod and is shown as a red star representing plasmon-enhanced fluorescence emission. (b) Typical time trace with one observable docking site (intensity height indicated by the red dashed line) taken on a nanorod under an excitation of a 2-nW, 785-nm laser. After irradiating by the same laser with 10 μW for 3 minutes, the nanorod no longer shows fluorescence bursts, indicating that the docking strand is no longer operational. (c) Time trace taken on the same nanorod shown in (b) after the high-power laser irradiation. There is no observable docking site.

the number of complementary base pairs, the salt concentration, and the temperature. The average burst duration of the fluorescence bursts in Fig. 2.2(b) is 0.93 ± 0.36 s. A long binding time is favorable for collecting enough photons to identify single molecule enhancement events, particularly when the fluorescence count rate is low. Jungmann *et. al.* reported an average bound time of 5 s for a duplex length of 10 base pairs at similar conditions [38], which is in agreement with the order of magnitude we obtained here. We attribute the small difference to photobleaching and blinking of the fluorophores.

The weak background in Fig. 2.2(b), ~ 20 counts in 100 ms, comes from the detector's dark counts, from all the fluorescent molecules in the focal volume of the excitation laser as well as from some photoluminescence of the gold nanorod. The average intensity of the fluorescence bursts is 200 counts in 100 ms, corresponding to a count rate of 1,800 counts/s from a nanorod-enhanced IRDye800CW molecule excluding the background. To quantify the fluorescence enhancement, we measured the average count rate from a molecule when not enhanced by measuring the size of the focal volume and the count rate from all the molecules in it, as described in the Supporting Information. These measurements yielded a molecular brightness of 2.0 ± 0.3 counts/s/molecule. Therefore, the bursts in Fig. 2.2 (b) correspond to an enhancement factor of 900.

Concerned with the stability of the transient binding, we deliberately applied high laser power to the nanorods and found that transient binding events typically disappear under continuous irradiation of some μW for a few minutes. For example, after measuring trace of Fig. 2.2(b) we irradiated the nanorod with the 785-nm continuous-wave laser at 10 μW for 3 minutes. We then measured again with low power and found no DNA-binding events, as shown in Fig. 2.2(c). The remaining short and low-intensity events are attributed to unspecific sticking to the glass surface as found previously [29, 32].

We then aim to explore the possible reasons for the disappearance of the bursts. Firstly we consider a perturbation of the hybridization equilibrium due to an increased local temperature due to plasmonic heating of the nanorod [43]. We estimated the surface temperature of the nanorod under the illumination conditions used in this work and found an increase of 5.3 K with a laser power of 10 μW (Supporting Information). It appears that the docking strand was permanently removed or damaged by irradiation of high laser intensity, namely, the reactivity of the base pairs on the docking strand was lost or the gold-thiol bond was broken, followed by the release of the entire docking strand. Light-induced breaking of gold-thiol bond in such a nanoparticle-DNA system has been observed under irradiation of pulsed lasers, and is usually attributed to the excitation of hot electrons at the surface of the nanoparticle [46, 47]. Continuous-wave lasers were only observed to affect dehybridization of DNAs by photothermally increasing the bulk temperature of the solution. However, the intensity of resonant irradiation we applied (8.8 kW/cm^2) was at least three orders of magnitude higher than previous bulk measurements [46, 48]. Thus, our conditions generate much more hot electrons, resulting in enhanced photo-induced reactions and hence the loss of docking strands attached to the gold surface.

To further test this hypothesis, we investigated nanorods with multiple observable docking strands. We found that docking strands associated with higher enhancement were generally more vulnerable to laser illumination. Figure 2.3(a) shows a time trace from a nanorod with two observable docking sites (recorded with an excitation power of 2 nW), evidenced by the fluorescent bursts with two distinct heights. After increasing the laser power to 10

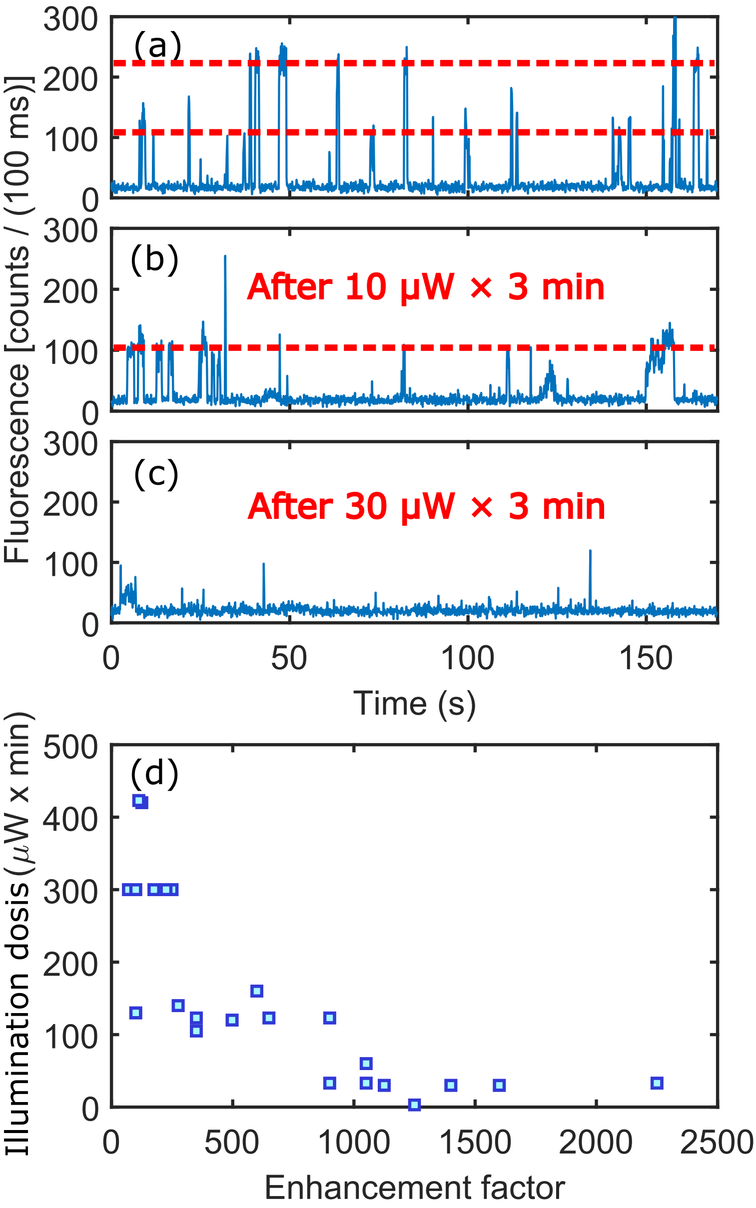

Figure 2.3: (a-c) Fluorescence time traces taken on the same gold nanorod at an excitation power of 2 nW. The original time trace (a) shows 2 observable binding sites (indicated by the red dashed lines). (b) After irradiating with the same laser at 10 μW for 3 minutes, the fluorescence bursts with higher enhancement have disappeared. (c) After irradiating at 30 μW for another 3 minutes, fluorescence bursts with lower enhancement also disappear. (d) Negative correlation between the enhancement factor that each docking site produces and the "dose of irradiation" that was applied before it was completely damaged.

μW and irradiating for 3 minutes, the time trace measured at 2 nW showed only one observable binding site (Fig. 2.3(b)). The only short and high burst is attributable to non-specific sticking of imager strands to the substrate near the nanorod. We further increased the laser power to 30 μW and irradiated for another 3 minutes, after which the nanorod showed no transient binding at all (Fig. 2.3(c)).

Further examination of more nanorods showed that the breaking of docking sites is also dependent on the duration of irradiation. We define the product of the laser power and irradiation time as the "illumination dose” and correlate the enhancement factor that each docking site produces with the dose of irradiation that was applied before it was completely damaged, as shown in Fig. 2.3(d). Although the applied dose of irradiation should be higher than the real threshold of photo-damage, we see a general correlation between higher enhancement factor and lower applied irradiation dose.

Our observations cannot be explained by DNA-melting since the disappearance is irreversible. The mechanism behind this irreversible disappearance cannot be laser-induced heating of the nanorod since the steady-state temperature distribution is uniform over the entire gold nanorod due to the high thermal conductivity of gold [49]. Thus, we attribute this irreversible breakage of the DNA-transient binding to hot electrons damage of the Au-S bonds.

2.3.2. Binding sites on the substrate

In a second approach, the substrate surface was saturated with docking strands. The concentration of dye-labeled imager strand was 5 nM with 500 mM NaCl in HEPES pH 7.0 buffer, as shown schematically in Fig. 2.4(a) . If a dye-labeled imager strand binds to a docking strand near a gold nanorod, we see a fluorescence burst in the time trace, as shown in the upper panel of Fig. 2.4(b). The excitation power was also 2 nW. The photoluminescence spectrum of this nanorod shows a plasmon resonance at 786 nm, as shown in Fig. 2.1(b). Imager strands bind to different docking strands at random positions in the near-field, giving rise to fluorescence bursts with different intensities.

We irradiated the nanorod with increasing laser intensity and tested the presence of transient binding by measuring time traces with low laser intensity afterwards, in the same way as for the first approach. The lower panel of Fig. 2.4(b) shows the time trace recorded at 2 nW after the nanorod was irradiated under 100 μW for 3 minutes. Imager strands are still binding to the docking strands and producing long fluorescent bursts. The possible reason is that, unlike in the first approach, hot electrons generated on the surface of nanorods cannot reach the molecules that are immobilized on the substrate surface or the hot electrons cannot break the bond between the glass and the DNA docking strand.

The strongest fluorescent burst in Fig. 2.4(b) shows a count rate of $\sim$ 7100 counts/s against a background fluorescence of $\sim$ 200 counts/s, yielding a fluorescent enhancement factor of 3,500. This is a 4 $\times$ higher enhancement that the one found in the case of the DNA docking strand was attached to the gold nanorod. We attribute this to the higher spatial sampling of the plasmonic near field in the case of the DNA attached to the glass, since we saturated the glass surface with docking strands. In the case of the docking bound to the gold surface we have a few docking sites thus it is unlikely it will be at the best enhancement position.

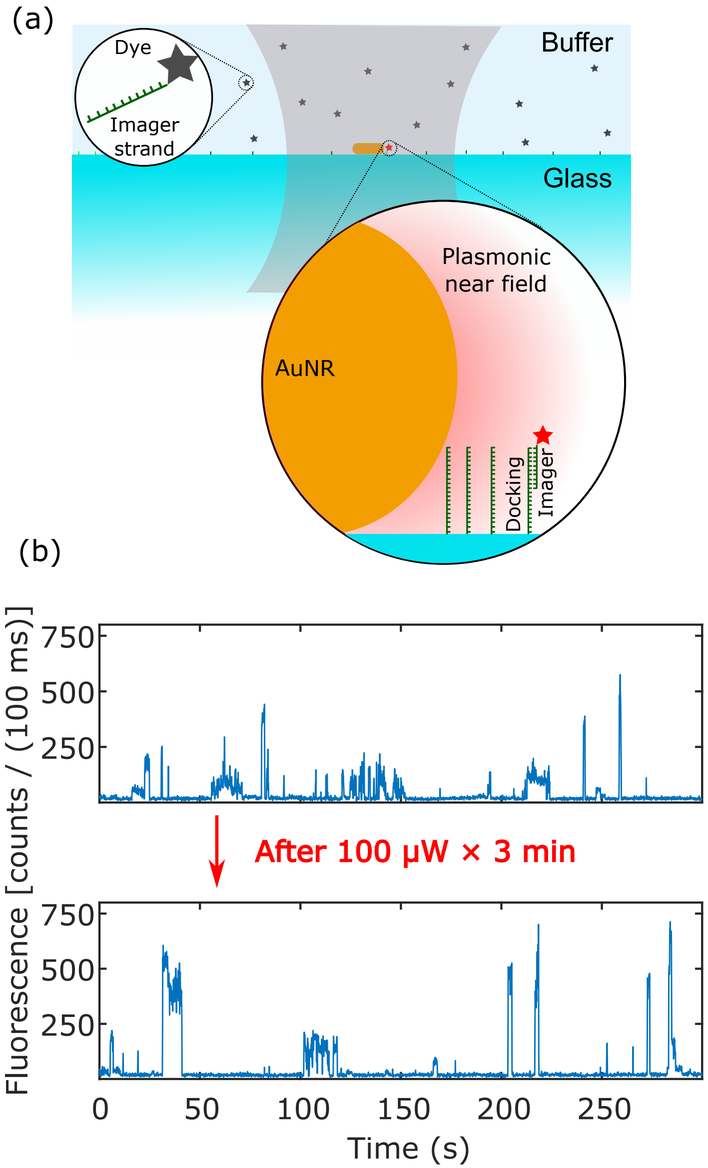

Figure 2.4: **Fluorescence enhancement with the docking strand on the coverslip surface**. (a) Schematic of transient binding. The entire glass substrate is functionalized with docking strands. The imager-IRDye800CW strands in the solution are shown in gray representing unenhanced fluorescence. One of the imagers is hybridizing to a docking strand tethered to the substrate in the near field of the nanorod and is shown in red representing plasmon-enhanced fluorescence emission. (b) The upper pannel shows a fluorescence time trace taken on a nanorods under a 2-nW, 785- nm illumination. After irradiated under the same laser with 100 μW for 3 minutes, the nanorod still produces intense fluorescence bursts.

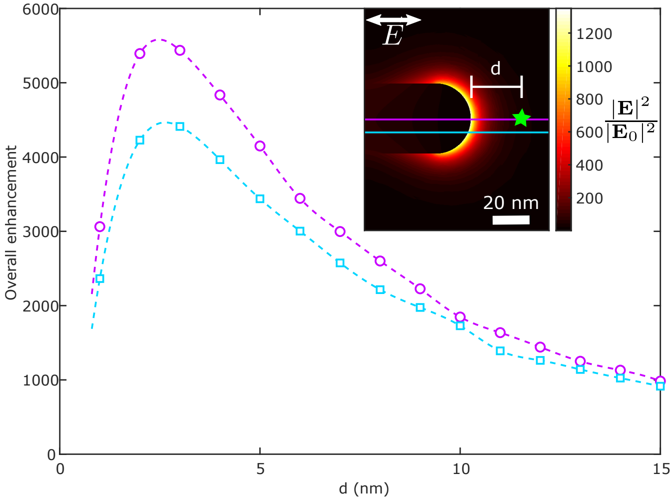

Figure 2.5: Calculated overall fluorescence enhancement factor as a function of the distance between the nanorod and an IRDye800CW molecule, *d*, for two different heights, as shown in the near-field map in the inset. The size of the nanorod is 38 nm × 116 nm, associated with a surface plasmon resonance wavelength of 784 nm in water.

2.3.3. Numerical simulations

We performed numerical simulations using a finite-element method (Comsol Multiphysics) and a boundary element method (SCUFF-EM) [50, 51] to understand the experimentally observed fluorescence enhancement. The details of the simulations is outlined in the Supporting Information. The nanorod in the simulation has a size of 38 nm × 116 nm. The calculated longitudinal surface plasmon resonance of the nanorod is 784 nm in water, providing a good spectral match with the excitation wavelength. We assume that the molecule is placed along the revolution axis of the nanorod. The polarization of the incident plane wave and the transition dipole moment of the molecule are parallel to the long axis of the nanorod. These settings are certainly not always valid in the experiments, but we used them to calculate the largest possible fluorescence enhancement. Figure 2.5 shows the overall enhancement factor as a function of distance between an IRDye800CW molecule and a nanorod. The optimum distance is about 4 nm to obtain the maximum fluorescence enhancement. If the molecule is too close, fluorescence quenching due to additional nonradiative decay pathways becomes dominant (Fig. S2.5) and the overall enhancement decreases; for longer distances, fluorescence enhancement diminishes because of a weaker electromagnetic field. Despite the presence of fluorescence quenching, a high maximum fluorescence enhancement factor of over 5,000 is expectable if the molecule is aligned properly with respect to the gold nanorod, which is in line with the experimentally observed enhancements, considering the isotropic distribution of molecular dipole moments.

2.4. Conclusions and outlook

In summary, we have demonstrated the fluorescence enhancement of near-infrared emitting single molecules by individual gold nanorods thanks to their intense localized fields close to the rod tips. A DNA-based transient binding method is implemented to transiently tether single fluorescent molecules in the plasmonic near field for approximately 1 s. Binding and unbinding of short DNA strands were directly visualized thanks to enhanced fluorescence. Any molecular dynamics that leads to a fluorescence intensity change from the labeled fluorophore within the binding time could also be visualized near the nanorods. Transient binding disappears upon irradiation of strong laser intensity if the docking strands are attached to the surface of the gold nanorods through Au-thiol bonds, probably due to hot electron induced DNA release. It is therefore advised to immobilize the docking strands on the glass substrate to prevent DNA release, especially when a pulsed laser is used.

Using the strategy of immobilizing the docking strands on the glass substrate, a remarkable 3,500-fold enhancement in fluorescence intensity from single molecules was observed, which agrees well with numerical simulations. This drastic increase in fluorescence intensity is potentially valuable for enhancing the detection sensitivity and contrast of molecular bioimaging. The position of the emitter and the duration of the emitter-plasmon interaction can be manipulated by proper DNA engineering. The experimental methods presented here can be readily extended to other dyes and nanostructures.

2.5. Supporting information

2.5.1. Sample preparation

Materials. Methanol (99.8%), 3-Mercaptopropyl) trimethoxysilane (MPTS, 95%), cysteamine (98%), 4-(2-Hydroxyethyl) piperazine-1-ethanesulfonic acid (HEPES, 99.5%), bovine serum albumin (BSA, 96%), tris(2-carboxyethyl) phosphine hydrochloride (TCEP, 98%) were purchased from Sigma-Aldrich; Sodium acetate (CH3COONa, 99%) from Merck; NeutrAvidin (NA) protein and succinimidyl 4-(p-maleimidophenyl)butyrate (SMPB) from ThermoFisher. HEPES buffer (10 mM) was prepared by dissolving HEPES in milli-Q water and the pH was adjusted to 7. Acetate buffer (pH 4) was prepared from acetic acid and sodium acetate. All the DNA oligonucleotides including the single strand DNA labeled with IRDye800CW (imager-IRDye800CW) were purchased from Integrated DNA Technologies, Inc. The sequence of imager-IRDye800CW is 3'-TAT GTA GAT C-5'-IRDye800CW. Gold nanorods were purchased from Nanopartz Inc. (A12-40-780-CTAB). The average size is 38 nm × 118 nm by diameter and length.

Silanization of the coverslip surface. Glass coverslips (Menzel-Gläser, ϕ = 25 mm, No. 1) were cleaned and silanized before further functionalization. The coverslips were sonicated in water (20 min) and ethanol (20 min). They were dried with a clean nitrogen flow and then immersed for 30 minutes with gentle stirring in a methanol solution containing 1% (3-mercaptopropyl)trimethoxysilane (Sigma-Aldrich) and 5% glacial acetic acid in a Teflon incubator. Thereafter, the silanized slides were washed thoroughly with methanol and dried with a nitrogen flow. This results in binding of the silane groups to the active hydroxyl groups and creates a thiol surface that can be used for conjugation with gold nanorods and for passivation of the substrate surface. If not immediately used for the next step, they were stored inside a desiccator to maintain the activity of the thiol groups.

Gold nanorod immobilization. The suspension of gold nanorods we purchased is stabilized with cetyl trimethyl ammoniumbromide (CTAB). In order to immobilize the nanorods on a thiolated glass surface, we decreased the concentration of CTAB by centrifugation and resuspension in milliQ. This solution of nanorods was in contact for with the thiol-activated glass coverslip for 30 minutes. Unbound gold nanorods were washed away with milliQ water. This procedure resulted in around 6 isolated single gold nanorods per 100 μm^2 area immobilized on the substrate.

Docking DNA on gold nanorods. The coverslip with gold nanorods was treated with a mixture of thiolated docking DNA strands, methoxy-poly(ethylene glycol)-thiol (mPEG7-SH, MW = 350), 5 mM NaCl and 1 mM Tris(2-carboxyethyl)phosphine hydrochloride (TCEP) in 0.1 M acetate buffer at pH = 4. The sequence of the docking strand was DTPA-5'-ATA CAT CTA GAA ATT-3'. DTPA represents dithiol phosphoramidite, which strongly binds the docking strands to the gold nanorods. The average number of docking strands on a gold nanorod can be controlled by the concentration ratio between docking strands and mPEG7-SH, which was kept at around 1:1000 to ensure only a few docking strands sat at the tips of a nanorod. TCEP was used to prevent the formation of disulfide bonds and thus maintain the reactively of thiol groups. The incubation lasted overnight and the coverslip was washed extensively with HEPES buffer.

To prevent nonspecific sticking of imager strands to the surface, the rest of the glass surface was passivated with bovine serumalbumin (BSA). This was achieved by incubating the coverslips with 1 mM succinimidyl 4-(p-maleimidophenyl)butyrate (SMPB), 20 μM BSA and 1 mM TCEP in HEPES buffer for 2 hours. SMPB is a cross-linker that contains an amine-reactive end (N-hydroxysuccinimide ester) and a thiol-reactive end (maleimide), thereby binding BSA to the substrate. The unreacted chemicals were removed by washing with HEPES buffer. The functionalized coverslip was used immediately or stored in HEPES buffer. The chemical structure used for this situation is shown in Fig. S2.1(a).

Docking DNA on a glass substrate. The coverslip with gold nanorods was treated with 100 μM cysteamine and TCEP in 0.1 M acetate buffer at pH = 4 for at least 2 hours to passivate the surface of nanorods. After the slide was washed with HEPES buffer, it was treated with a solution with 1 μM NeutrAvidin (NA), 10 μM SMPB and 1 mM TCEP in HEPES buffer (pH = 7). SMPB is a cross-linker that immobilizes NA protein molecules onto the glass substrate. The incubation lasted 90 min and excess reagents were washed away by HEPES buffer. Lastly, 100 nM docking DNA strand in HEPES buffer was applied to the coverslip. The sequence of the docking strand was biotinTEG-5'-A GCT ATA TTT ATA CAT CTA G-3'. Biotin-TEG increases the oligo-biotin distance to 15 atoms using a triethyleneglycol (TEG) spacer. The biotinylated oligonucleotides binds strongly to the NeutrAvidin molecules. After 30 minutes, the coverslip was washed with HEPES buffer. The functionalized coverslip was used immediately or stored in HEPES buffer. The chemical structure used for this situation is shown in Fig. S2.1(b).

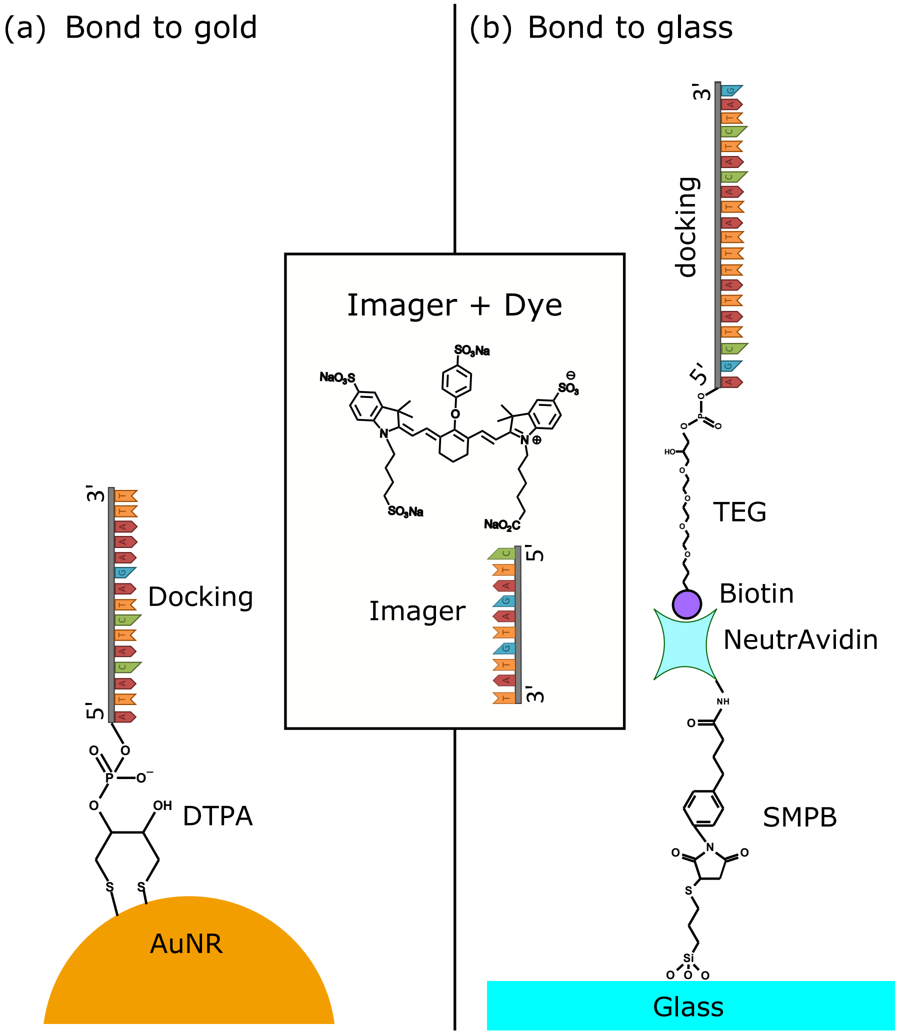

Figure S2.1: Schematic representation of the bonds used to attach the docking strand to the gold surface (a) and glass surface (b). The inset in the middle shows the imager DNA strand and the dye structure, which is the same for both cases.

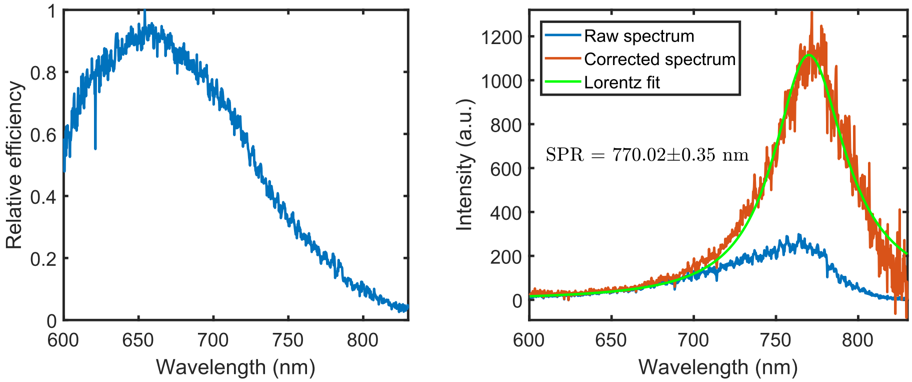

Figure S2.2: Left: Relative detection efficiency of the setup as a function of wavelength. (Right) The one-photon photoluminescence raw (blue) and corrected (red) spectra of a single nanorod. The corrected spectrum was fitted with Lorentzian line shape (green), yielding a resonance wavelength of 770.02 ± 0.35 nm.

2.5.2. Correction of gold nanorod spectra

The photoluminescence emission of gold nanorods is in the near-infrared range, where the collection efficiency of the optical setup is poor. Therefore, the measured raw spectra have to be normalized by the spectral response of the setup. To this end, we used a standard fluorophore for the near-infrared range, 4-dimethylamino-4'-nitrostilbene (4,4'-DMANS, Sigma-Aldrich), excited with the 532-nm laser. The wavelength-dependent relative detection efficiency was obtained by normalizing the measured fluorescence spectrum by the real emission spectrum of the standard dye [52]. The left panel of Fig. S2.2 shows the relative response of the setup as a function of wavelength. The measured spectra of nanorods, with the background spectra subtracted, were corrected for the spectral response function and further fitted with a Lorentzian profile to obtain the localized surface plasmon resonance wavelength. The right panel of Fig. S2.2 shows an example spectrum of a single nanorod with spectral correction and Lorentzian fitting.

2.5.3. Size of the confocal volume

We measured the size of the confocal volume by imaging gold nanorods, which are smaller than the diffraction limited point spread function (PSF) of the instrument [53]. We scanned three-dimensional photoluminescence images of a gold nanorod in water excited with the 785-nm laser. As an example, Fig. S2.3 shows the *yz* section of the point spread function (*z* is along the optical axis). All three sections (*xy*, *xz* and *yz*) of the point spread function were fitted with two-dimensional Gaussian functions. Taking the *xy* plane as an example, the model is

$$I = I_0 + I_{\mathrm{max}}\mathrm{exp}\left\{-2\left[\left(\frac{x-x_0}{w_x}\right)^2 + \left(\frac{y-y_0}{w_y}\right)^2\right]\right\}. \tag{2.1}$$

(x_0, y_0) is the coordinate of the center of the section and w_x, w_y are the $1/e^2$ radii of the point spread function in the fitting plane. $I_{\max}$ is the maximum photoluminescence intensity and I_0 is the background signal.

Table 2.1 shows the resulting lateral and axial dimensions from the fitting. The confocal volume is calculated from the mean dimensions in each axis as

$$V_{\text{conf}} = \left(\frac{\pi}{2}\right)^{3/2} w_x w_y w_z = 0.164 \pm 0.002 \text{ fL}. \tag{2.2}$$

Table 2.1: Dimensions of the point spread function determined from 2D Gaussian fits

Section	w_x / nm	w_y / nm	w_z / nm
xy	320.8 ± 4.6	275.6 ± 3.8	-
xz	326.6 ± 2.8	-	873.2 ± 7.8
yz	-	299.8 ± 2.6	912.4 ± 8.0
Mean	323.7 ± 2.7	287.7 ± 2.3	892.8 ± 5.6

2.5.4. Saturation of IRDye800CW

We measured the fluorescence intensity from the dye as a function of the excitation power to find the saturation intensity. Figure S2.4 shows the fluorescence signal from a solution of 100 nM imager-IRDye800CW in HEPES buffer as a function of the excitation power. Fluorescence scales linearly with the excitation power for power lower than 10 μW. With higher power, the curve deviates from the linear relation. The fluorescence intensity decreases with increasing power for excitation power higher than $\sim$ 40 μW, which is attributed to photobleaching. The saturation power is 5000 times higher than that is incident to the gold nanorods for the enhancement experiment. The saturation intensity is well above the local field intensity that can be achieved by the nanorods used in our study. Therefore, molecules in the close vicinity of gold nanorods are still well below saturation.

By extrapolating the data and fitting shown in Figure S2.4, we predict the fluorescence count rate to be 19.7 ± 3.1 counts/s if excited at 2 nW. For a solution of 100 nM, there are 9.9 ± 0.1 molecules in the focal volume. These yield a molecular brightness of 2.0 ± 0.3 counts/s/molecule.

2.5.5. Numerical simulations of fluorescence enhancement

Under weak excitation well below saturation (Fig. S2.4), the overall enhancement factor is the product of excitation enhancement and emission enhancement [44]. The excitation enhancement arises from the concentrated high local field due to the resonant excitation of the localized surface plasmons. The emission enhancement is a result of the competition between emission rate enhancement due to Purcell effect and fluorescence quenching due to the additional non-radiative decay pathways provided by gold.

The excitation enhancement was calculated with a finite-element method using Comsol Multiphysics. The near-field intensity map of a single gold nanorod with a size of 38 nm

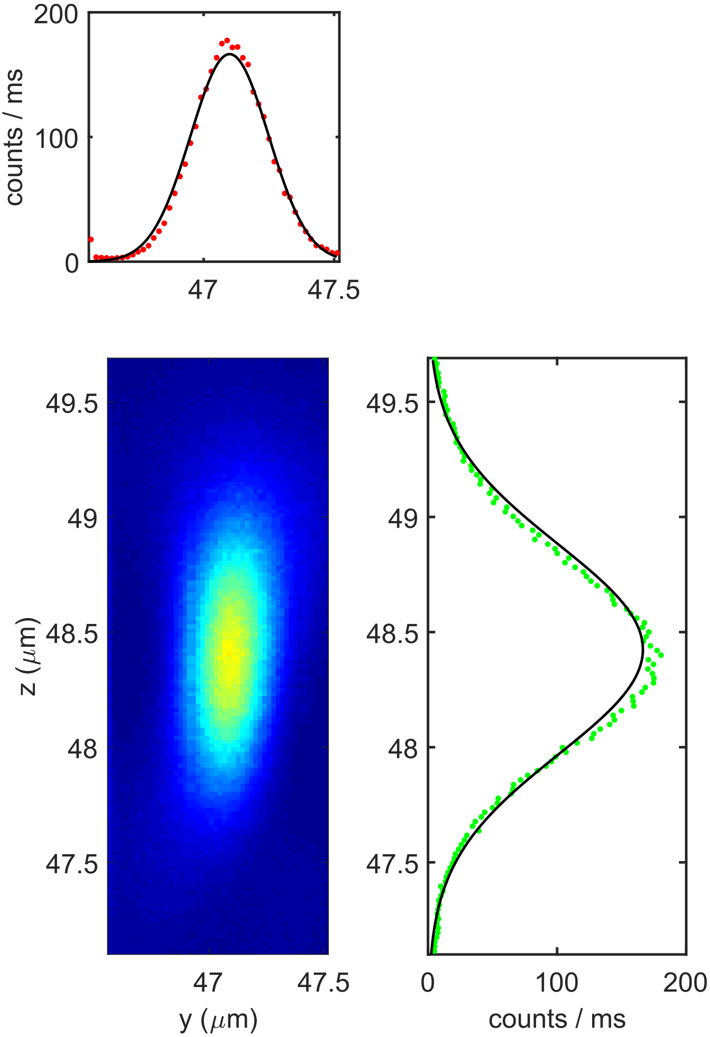

Figure S2.3: *yz* section of the point spread function measured with a gold nanorod. Line profiles through the center are shown. Experimental data are shown as red (along the *y* axis) and green (along the *z* axis) dots and the Gaussian fits are represented by black lines.

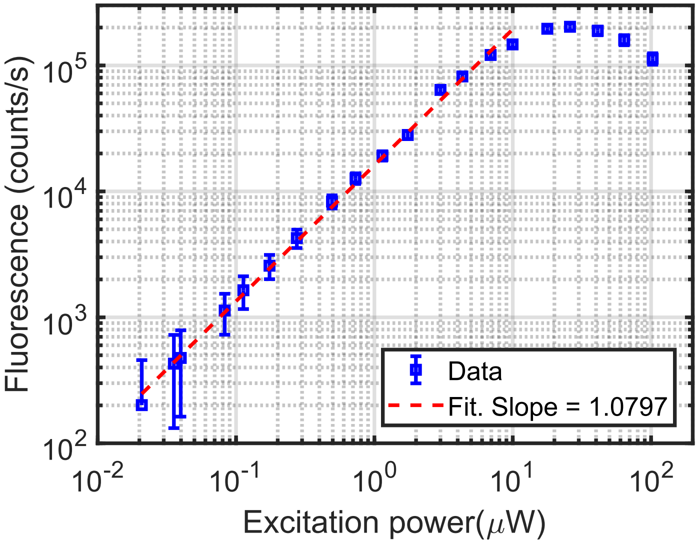

Figure S2.4: Fluorescence signal from a solution of 100 nM imager-IRDye800CW in HEPES buffer as a function of the excitation power. We found a saturation power of 10 μW.

× 116 nm in water excited at 785 nm are calculated. The nanorod is found to be associated with a surface plasmon resonance at 784 nm by calculating extinction cross-sections as functions of wavelength. This size was chosen to ensure the best spectral overlap with the excitation laser and, hence, the largest enhancement factor. The incident plane wave was linearly polarized parallel to the long axis of the nanorod. The dielectric permitivity for gold was taken from Johnson and Christy[54], and the refractive index of the ambient medium was taken as 1.33. The excitation enhancement E_{exc} is the ratio of local field intensities with and without the nanorod, $E_{\text{exc}} = |\mathbf{E}|^2/|\mathbf{E}_0|^2$, at the emitter's position.

We used a boundary element method (SCUFF-EM) to evaluate the modifications of decay rates and emission enhancement using a classical electrodynamics approach [50, 51]. An IRDye800CW molecule was modeled as a radiating point dipole oscillating at a frequency which corresponds to the emission wavelength of the molecule. It was assumed that the point dipole is placed along the long axis of the nanorod with a certain distance from the tip and oriented parallel to the revolution axis of the nanorod. All the results were averaged over the actual luminescence spectrum of the molecule. The diameter and length of the nanorod were set as 38 nm and 116 nm respectively. The refractive index of the ambient medium was 1.33, and the dielectric constant for gold was taken from Johnson and Christy [54].

Figure S2.5(a) plots the modified radiative (k_{r}) and nonradiative (K_{nr}) decay rates relative to the intrinsic radiating rate of the dipole (k_{r}^0) against the separation between dipole and rod. The competition between k_{r} and K_{nr} leads to an emission enhancement that is represented by the green diamonds in Fig. S2.5(b). The orange triangles in Fig. S2.5 show the excitation enhancement, which is calculated by a finite-element method.

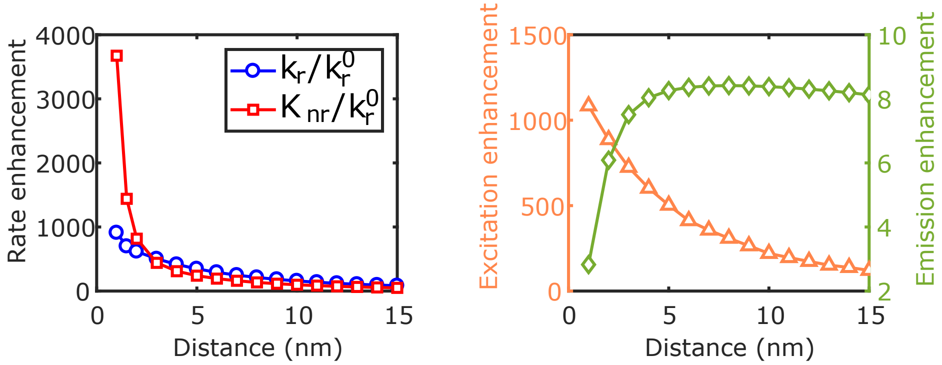

Figure S2.5: (a) Calculated radiative rate enhancement ($k_\mathrm{r}/k_\mathrm{r}^0$, blue circles) and relative additional nonradiative rate ($K_\mathrm{nr}/k_\mathrm{r}^0$, red squares) of an IRDye800CW molecule as a function of the distance to the tip of the nanorod. (b) Calculated excitation enhancement (orange triangles, left axis) and emission enhancement (green diamonds, right axis) as functions of the distance to the tip of the nanorod.

2.5.6. Calculation of nanorod temperature increase

Because the nanorods are only sparsely scattered on the substrate, bulk heating of the solution can be neglected. Each individual nanorod can be considered as an independent light-induced heat source. The local temperature increase of a nanorod depends upon the absorption cross-section, laser intensity, geometry of the nanorod, and thermal conductivities of the immersion medium and supporting substrate, as illustrated by the following equation [49]:

$$\Delta T_\mathrm{NR} = \frac{\sigma_\mathrm{abs} I}{4\pi R_\mathrm{eq} \beta \bar{\kappa}}, \tag{2.3}$$

where σ_abs is absorption cross section, I intensity of illumination, R_eq the radius of a sphere with the same volume as the nanorod, β a nanorod geometry-dependent coefficient and κ the averaged thermal conductivities of water and glass.

In the calculation, we considered a nanorod with a size of 38 nm × 116 nm by diameter and length. σ_abs at 785 nm was calculated using Comsol Multiphysics to be 5×10^{-14} m^2. $I = 8.8$ kW/cm^2 at the center of the laser focus. For a nanorod, $\beta = 1 + 0.96587 \ln^2(\mathrm{AR}) = 2.2$ (AR is the aspect ratio of the nanorod). $\bar{\kappa} = (\kappa_\mathrm{water} + \kappa_\mathrm{glass})/2 = 1$ W/(m·K). On the basis of these parameters, we calculated a temperature increase of 5.3 K at the surface of the nanorod. Such a local temperature is well below that required for thermally breaking a Au-S bond [46].

References

[1] C. F. Bohren and D. R. Huffman, *Absorption and scattering of light by small particles* (John Wiley & Sons, 2008).

[2] S. Link and M. A. El-Sayed, *Spectral properties and relaxation dynamics of surface*

plasmon electronic oscillations in gold and silver nanodots and nanorods, The Journal of Physical Chemistry B **103**, 8410 (1999).

[3] P. Zijlstra and M. Orrit, *Single metal nanoparticles: optical detection, spectroscopy and applications,* Reports on Progress in Physics **74**, 106401 (2011).

[4] J. R. Lakowicz, *Plasmonics in biology and plasmon-controlled fluorescence,* Plasmonics **1**, 5 (2006).

[5] J. Pérez-Juste, I. Pastoriza-Santos, L. M. Liz-Marzán, and P. Mulvaney, *Gold nanorods: synthesis, characterization and applications,* Coordination Chemistry Reviews **249**, 1870 (2005).

[6] L. Vigderman, B. P. Khanal, and E. R. Zubarev, *Functional gold nanorods: synthesis, self-assembly, and sensing applications,* Advanced Materials **24**, 4811 (2012).

[7] S. Yao, H.-H. Cai, M. Liu, and P.-H. Yang, *Fluorescent labeling of cellular targets and multicolor imaging with gold nanorods,* Dyes and Pigments **101**, 286 (2014).

[8] P. Zijlstra, P. M. Paulo, and M. Orrit, *Optical detection of single non-absorbing molecules using the surface plasmon resonance of a gold nanorod,* Nature Nanotechnology **7**, 379 (2012).

[9] D. P. O'Neal, L. R. Hirsch, N. J. Halas, J. D. Payne, and J. L. West, *Photo-thermal tumor ablation in mice using near infrared-absorbing nanoparticles,* Cancer Letters **209**, 171 (2004).

[10] X. Huang, I. H. El-Sayed, W. Qian, and M. A. El-Sayed, *Cancer cell imaging and photothermal therapy in the near-infrared region by using gold nanorods,* Journal of the American Chemical Society **128**, 2115 (2006).

[11] X. Huang, P. K. Jain, I. H. El-Sayed, and M. A. El-Sayed, *Plasmonic photothermal therapy (pptt) using gold nanoparticles,* Lasers in Medical Science **23**, 217 (2008).

[12] K. Kneipp, H. Kneipp, I. Itzkan, R. R. Dasari, and M. S. Feld, *Ultrasensitive chemical analysis by Raman spectroscopy,* Chemical Reviews **99**, 2957 (1999).

[13] J. F. Li, Y. F. Huang, Y. Ding, Z. L. Yang, S. B. Li, X. S. Zhou, F. R. Fan, W. Zhang, Z. Y. Zhou, D. Y. Wu, B. Ren, Z. L. Wang, and Z. Q. Tian, *Shell-isolated nanoparticle-enhanced Raman spectroscopy,* Nature **464**, 392 (2010).

[14] S. Kühn, U. Håkanson, L. Rogobete, and V. Sandoghdar, *Enhancement of single-molecule fluorescence using a gold nanoparticle as an optical nanoantenna,* Physical Review Letters **97**, 017402 (2006).

[15] P. Anger, P. Bharadwaj, and L. Novotny, *Enhancement and quenching of single-molecule fluorescence,* Physical Review Letters **96**, 113002 (2006).

[16] Y. Fu, J. Zhang, and J. R. Lakowicz, *Plasmonic enhancement of single-molecule fluorescence near a silver nanoparticle,* Journal of Fluorescence **17**, 811 (2007).

[17] P. Bharadwaj, P. Anger, and L. Novotny, *Nanoplasmonic enhancement of single-molecule fluorescence,* Nanotechnology **18**, 044017 (2006).

[18] J. Lakowicz and Y. Fu, *Modification of single molecule fluorescence near metallic nanostructures,* Laser Photonics Reviews **3**, 221 (2009).

[19] P. Bharadwaj and L. Novotny, *Spectral dependence of single molecule fluorescence enhancement,* Optics Express **15**, 14266 (2007).

[20] T. Taminiau, F. Stefani, F. B. Segerink, and N. Van Hulst, *Optical antennas direct single-molecule emission,* Nature Photonics **2**, 234 (2008).

[21] M. Van Oosten, T. Schäfer, J. A. Gazendam, K. Ohlsen, E. Tsompanidou, M. C. De Goffau, H. J. Harmsen, L. M. Crane, E. Lim, K. P. Francis, *et al.*, *Real-time in vivo imaging of invasive-and biomaterial-associated bacterial infections using fluorescently labelled vancomycin,* Nature Communications **4**, ncomms3584 (2013).

[22] T. Iijima, T. Aoyagi, Y. Iwao, J. Masuda, M. Fuse, N. Kobayashi, and H. Sankawa, *Cardiac output and circulating blood volume analysis by pulse dye-densitometry,* Journal of Clinical Monitoring **13**, 81 (1997).

[23] R. Benson and H. Kues, *Fluorescence properties of indocyanine green as related to angiography,* Physics in Medicine & Biology **23**, 159 (1978).

[24] N. Gandra, C. Portz, L. Tian, R. Tang, B. Xu, S. Achilefu, and S. Singamaneni, *Probing distance-dependent plasmon-enhanced near-infrared fluorescence using polyelectrolyte multilayers as dielectric spacers,* Angewandte Chemie International Edition **53**, 866 (2014).

[25] R. Bardhan, N. K. Grady, J. R. Cole, A. Joshi, and N. J. Halas, *Fluorescence enhancement by au nanostructures: nanoshells and nanorods,* ACS Nano **3**, 744 (2009).

[26] F. Tam, G. P. Goodrich, B. R. Johnson, and N. J. Halas, *Plasmonic enhancement of molecular fluorescence,* Nano Letters **7**, 496 (2007).

[27] R. Bardhan, N. K. Grady, and N. J. Halas, *Nanoscale control of near-infrared fluorescence enhancement using au nanoshells,* Small **4**, 1716 (2008).

[28] Y. Fu, J. Zhang, and J. R. Lakowicz, *Plasmon-enhanced fluorescence from single fluorophores end-linked to gold nanorods,* Journal of the American Chemical Society **132**, 5540 (2010).

[29] H. Yuan, S. Khatua, P. Zijlstra, M. Yorulmaz, and M. Orrit, *Thousand-fold enhancement of single-molecule fluorescence near a single gold nanorod,* Angewandte Chemie International Edition **52**, 1217 (2013).

[30] W. Zhang, M. Caldarola, B. Pradhan, and M. Orrit, *Gold nanorod enhanced fluorescence enables single-molecule electrochemistry of methylene blue,* Angewandte Chemie International Edition **56**, 3566 (2017).

[31] B. Pradhan, S. Khatua, A. Gupta, T. Aartsma, G. Canters, and M. Orrit, *Gold-nanorod-enhanced fluorescence correlation spectroscopy of fluorophores with high quantum yield in lipid bilayers,* Journal of Physical Chemistry C **120**, 25996 (2016).

[32] A. A. Kinkhabwala, Z. Yu, S. Fan, and W. E. Moerner, *Fluorescence correlation spectroscopy at high concentrations using gold bowtie nanoantennas,* Chemical Physics **406**, 3 (2012).

[33] S. Khatua, H. Yuan, and M. Orrit, *Enhanced-fluorescence correlation spectroscopy at micro-molar dye concentration around a single gold nanorod,* Physical Chemistry Chemical Physics **17**, 21127 (2015).

[34] A. Puchkova, C. Vietz, E. Pibiri, B. Wünsch, M. Sanz Paz, G. P. Acuña, and P. Tinnefeld, *DNA origami nanoantennas with over 5000-fold fluorescence enhancement and single-molecule detection at 25 μm,* Nano Letters **15**, 8354 (2015).

[35] A. Kinkhabwala, Z. Yu, S. Fan, Y. Avlasevich, K. Müllen, and W. Moerner, *Large single-molecule fluorescence enhancements produced by a bowtie nanoantenna,* Nature Photonics **3**, 654 (2009).

[36] C. Vietz, I. Kaminska, M. Sanz Paz, P. Tinnefeld, and G. P. Acuña, *Broadband fluorescence enhancement with self-assembled silver nanoparticle optical antennas,* ACS Nano **11**, 4969 (2017).

[37] G. Acuna, F. Möller, P. Holzmeister, S. Beater, B. Lalkens, and P. Tinnefeld, *Fluorescence enhancement at docking sites of DNA-directed self-assembled nanoantennas,* Science **338**, 506 (2012).

[38] R. Jungmann, C. Steinhauer, M. Scheible, A. Kuzyk, P. Tinnefeld, and F. C. Simmel, *Single-molecule kinetics and super-resolution microscopy by fluorescence imaging of transient binding on DNA origami,* Nano Letters **10**, 4756 (2010).

[39] A. Sharonov and R. M. Hochstrasser, *Wide-field subdiffraction imaging by accumulated binding of diffusing probes,* Proceedings of the National Academy of Sciences of the United States of America **103**, 18911 (2006).

[40] J. Schnitzbauer, M. T. Strauss, T. Schlichthaerle, F. Schueder, and R. Jungmann, *Super-resolution microscopy with DNA-PAINT,* Nature Protocols **12**, 1198 (2017).

[41] A. Sassolas, B. D. Leca-Bouvier, and L. J. Blum, *DNA biosensors and microarrays,* Chemical Reviews **108**, 109 (2008).

[42] S. Khatua and M. Orrit, *Probing, sensing, and fluorescence enhancement with single gold nanorods,* Journal of Physical Chemistry Letters **5**, 3000 (2014).

[43] G. Baffou and R. Quidant, *Thermo-plasmonics: using metallic nanostructures as nano-sources of heat,* Laser & Photonics Reviews **7**, 171 (2013).

[44] S. Khatua, P. M. R. Paulo, H. Yuan, A. Gupta, P. Zijlstra, and M. Orrit, *Resonant plasmonic enhancement of single-molecule fluorescence by individual gold nanorods,* ACS Nano **8**, 4440 (2014).

[45] M. Yorulmaz, S. Khatua, P. Zijlstra, A. Gaiduk, and M. Orrit, *Luminescence quantum yield of single gold nanorods,* Nano Letters **12**, 4385 (2012).

[46] A. M. Goodman, N. J. Hogan, S. Gottheim, C. Li, S. E. Clare, and N. J. Halas, *Understanding resonant light-triggered DNA release from plasmonic nanoparticles,* ACS Nano **11**, 171 (2016).

[47] S. Simoncelli, Y. Li, E. Cortés, and S. A. Maier, *Nanoscale control of molecular self-assembly induced by plasmonic hot-electron dynamics,* ACS Nano **12**, 2184 (2018).

[48] R. Huschka, J. Zuloaga, M. W. Knight, L. V. Brown, P. Nordlander, and N. J. Halas, *Light-induced release of DNA from gold nanoparticles: Nanoshells and nanorods,* Journal of the American Chemical Society **133**, 12247 (2011).

[49] G. Baffou, R. Quidant, and F. J. García de Abajo, *Nanoscale control of optical heating in complex plasmonic systems,* ACS Nano **4**, 709 (2010).

[50] M. T. Homer Reid and S. G. Johnson, *Efficient Computation of Power, Force, and Torque in BEM Scattering Calculations,* ArXiv e-prints (2013), "arXiv":1307.2966 ["physics.comp-ph"] .

[51] Http://homerreid.com/scuff-EM.

[52] J. R. Lakowicz, *Principles of Fluorescence Spectroscopy*, 3rd ed. (Springer US, 2006) p. 954.

[53] S. Rüttinger, V. Buschmann, B. Krämer, R. Erdmann, R. Macdonald, and F. Koberling, *Comparison and accuracy of methods to determine the confocal volume for quantitative fluorescence correlation spectroscopy,* Journal of Microscopy **232**, 343 (2008).

[54] P. B. Johnson and R.-W. Christy, *Optical constants of the noble metals,* Physical Review B **6**, 4370 (1972).

3

Gold nanorod-enhanced fluorescence enables single-molecule electrochemistry of methylene blue

Redox reactions are central to energy conversion and life metabolism. Here we present electrochemical measurements with fluorescent readout of the redox-sensitive dye Methylene Blue (MB), at the single-molecule (SM) level. To overcome the low fluorescence quantum yield of MB we enhanced fluorescence by individual gold nanorods to achieve the required sensitivity. By measuring the same molecule at different electrochemical potentials we determined the mid-point potential of each single molecule through its redox-induced fluorescence blinking dynamics.

This chapter has been published in Angewandte Chemie International Edition **56**, 13 (2017) [1].

3.1. Introduction

Understanding electrochemical processes is important for a variety of fields such as electrocatalysis [2, 3], nanostructured material synthesis [4, 5], detection of ions [6] and biological processes [7, 8], among others. As redox reactions are extremely sensitive to the local environment, single-molecule (SM) techniques are naturally suited for such studies, since they provide local probes in the subnanometer range, with high sensitivity to changes of the physical and chemical properties of their local surroundings [9]. Electrochemistry with single-molecule sensitivity, proven for the first time by Fan and Bard [10], was an important step towards understanding the environment's influence on electron transfer reactions. An alternative approach to the electrical output is the combination of electrochemical control and optical readout of the molecules involved in the reaction [11]. Such an approach has proved successful with single-molecule sensitivity thanks to surface enhanced Raman spectroscopy (SERS) [12–14]. However, the behavior of molecules in the hot spots responsible for SERS signals is heavily influenced by interactions with the metal, in particular by possible hybridization of molecular orbitals with metal electronic states. Methods for the study of free molecules are thus needed.

Alternatively, fluorescence spectroscopy was also used as a readout of the oxidation or reduction state, relying on the switching of a high quantum yield fluorophore between fluorescent and non-fluorescent states [15]. With this approach, however, SM electrochemical information cannot be accessed due to the fast diffusion of the molecules in solution. Here we worked with immobilized molecules to access millisecond time scales and took advantage of fluorescence enhancement provided by individual gold nanorods (AuNRs) to enable electrochemistry with fluorescence readout at single-molecule level, even for weak emitters. The enhancement factors in the near field of nanorods is much weaker than those in SERS hot spots, but they are felt at much larger distances, of the order of 10 nm, enabling the study of isolated molecules, free from interaction with the metal.

3.2. Results and discussion

We studied the well-known redox-sensitive molecule Methylene Blue (MB), which is widely used for tissue staining [16, 17] and for biochemical studies as a redox indicator [18, 19]. MB is a brightly blue-colored, non-toxic, cationic thiazine dye [20]. MB undergoes the reversible one-proton, two-electron transfer redox reaction shown in Fig. 3.1(a). The product of the reaction is colorless *leuco*-Methylene Blue, which does not absorb visible light [21]. Due to their low quantum yield [22] of $\sim$ 4% it is difficult to detect single MB molecules by fluorescence. We performed a calibration experiment with MB molecules in solution to estimate the signal from an individual MB molecule and obtained 14 counts s^{-1}, which is well below our detection limit due to dark counts in the detector. Therefore, to achieve SM sensitivity, we propose to employ a fluorescence enhancement scheme.

For this purpose, we used AuNRs with an average size of 40 nm × 81 nm and a longitudinal surface plasmon resonance at about 660 nm. This plasmon resonance was selected to favor both excitation enhancement, *i.e.*, concentration of the excitation field at the laser wavelength (635 nm) at the tips of the AuNR, and emission enhancement, which depends on the overlap between the emission spectrum of the dye and the plasmon spectrum [23, 24], as

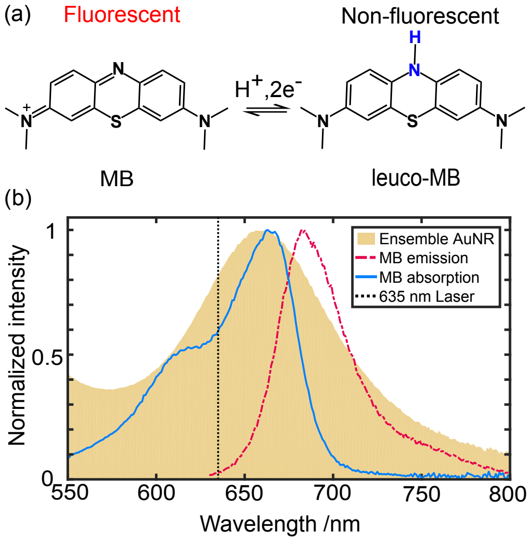

Figure 3.1: (a) Two-electron reduction/oxidation reaction of Methylene Blue (MB). The reduced species, *leuco*-Methylene Blue is non-fluorescent under visible excitation. (b) Absorption (blue) and emission (dashed red) spectra for MB in water. The shaded curve shows the UV-Vis extinction spectrum of a suspension of AuNRs in water. The vertical dotted line shows the wavelength used for fluorescence excitation of MB, on the blue wing of the longitudinal plasmon mode.

can be appreciated for the bulk spectra in Fig. 3.1(b). With these AuNRs we expect enhancement factors as high as 10^3, which will allow detection of SM events above the fluorescence background from unenhanced molecules.

In order to perform electrochemical measurements with fluorescent readout, we used a confocal microscope previously described [25], combined with the electrochemistry setup shown schematically in Fig. 3.2(a). The electrochemical cell presented three electrodes, consisting of a 30-nm thick gold layer deposited on the coverslip with a hole for optical access as the working electrode (WE), a saturated calomel electrode (SCE) as the reference electrode (RE), and a platinum wire as the counter electrode (CE). All the potentials throughout this work were reported relative to SCE. Isolated AuNRs and MB molecules were immobilized on the gold-free area of the coverslip. To allow reliable measurements of SMs, the MB layer had a concentration such that there was on average about 1 molecule in the electromagnetic near field of a AuNR. Because the MB molecules did not have direct electrical contact with the electrodes we used phenazine ethosulfate as an electron mediator to establish the redox potential of the medium surrounding the MB molecules. The working buffer was a pH = 2 HCl-KCl buffer, in which the mid-point potential of phenazine ethosulfate matches that of MB so that the redox potential in the electrochemical cell can be controlled conveniently by the potentiostat. For further details about the experimental configuration and sample preparation, see the Supporting Information.

Firstly, we used the electrochemistry-coupled fluorescence microscope to measure how the fluorescence of a small ensemble of $\sim$ 260 unenhanced molecules immobilized on the glass surface responded to a static redox potential. We applied different potentials and

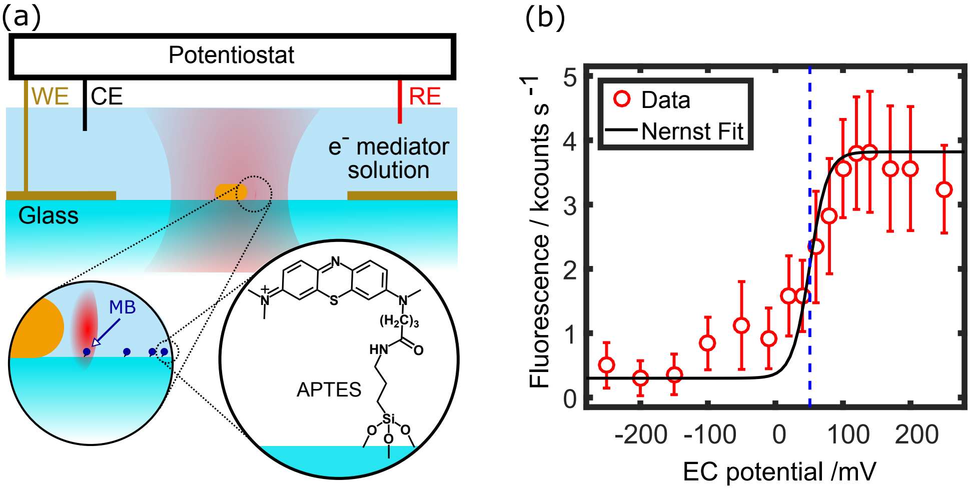

Figure 3.2: Electrochemistry with fluorescent readout. (a) Scheme of the combined electrochemical-confocal setup and sample (WE: working electrode, CE: counterelectrode, RE: reference electrode). Individual AuNRs (not to scale) and MB molecules were immobilized on the glass surface. Phenazine ethosulfate mediates electron transfer between MB molecules and the gold film controlled via the potensiostat. (b) Ensemble fluorescence response of $\sim$ 260 unenhanced MB molecules to the electrochemical potential, showing the controlled switching from the reduced state at low potentials to the oxidized state at high potentials. The black curve is a fit using the Nernst equation and the dashed line illustrates the obtained mid-point potential (51 ± 4 mV).

recorded the corresponding fluorescence counts under 5 W/cm^2 illumination once the equilibrium was established. Figure 3.2(b) shows the intensity measured as a function of the applied voltage, where the switching of MB molecules from the dark to the bright state can be seen. We assign the hump at around -50 mV to molecule-substrate interactions, as it was not observed when doing the same measurement with MB solutions (data not shown). We modeled the ensemble of MB molecules with the Nernst equation (see the Supporting Information) and obtained a mid-point potential of 51 ± 4 mV. This shows our capability of performing electrochemical experiments through fluorescence monitoring of a small ensemble.

Secondly, we turned to SM experiments, which are possible thanks to the enhancement provided by the AuNRs. We worked in the situation presented in Fig. 3.2(a), with one molecule in the near-field of the AuNR and several molecules in the confocal volume, contributing to the total signal. The low QY of MB has the advantage of providing a low background from those unenhanced molecules which does not obscure the signal from the enhanced molecule, *i.e.*, the signal from the enhanced molecule is high compared to the background. At SM level we expect to see fluorescence blinking induced by the dynamic equilibrium of the redox reaction. When the potential is set to the mid-point potential, we expect the molecule to spend half of the time reduced and half of the time oxidized, which will be evidenced by equal on- and off-times for the blinking. With the same reasoning, for reducing (oxidizing) potentials we expect that the molecule will spend more time in the off (on) state.

The fluorescence time trace of a single enhanced MB molecule is shown in Fig. 3.3(a),

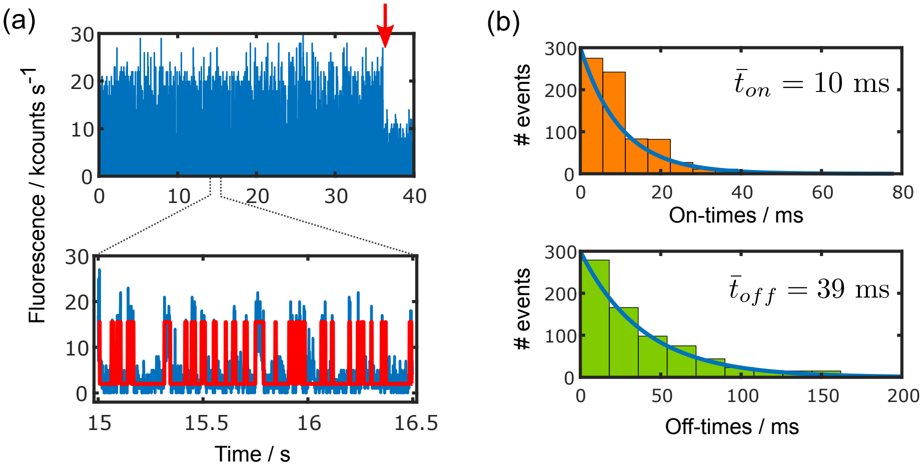

Figure 3.3: Single-molecule measurements at a fixed potential. (a) (top) Fluorescent time trace from a AuNR-enhanced single molecule (binned to 1 ms) under an electrochemical potential of 80 mV. The arrow shows the one-step bleaching event. (bottom) Expansion that evidences the blinking behavior. The red trace was obtained through a step-detection algorithm. For this particular SM we estimated an enhancement factor value of $\sim$ 800. (b) Blinking events histograms for the on- (top) and off-times (bottom), showing an exponential distribution. The estimated mean times from single-exponential fits (blue solid lines) are shown on each plot.

where SM reduction and oxidation events can be clearly distinguished, as well as a single-step bleaching event. The laser excitation peak intensity was 5 W/cm^2 . The bin time of 1 ms was chosen so that the on/off states can be clearly observed (for further discussion on this point, refer to the Supporting Information). A step-detection algorithm [26] was used to extract the times associated to the switching events, shown in the figure in red. The obtained on- and off-times follow an exponential distribution with mean on- and off-times of $\bar{t}_{\mathrm{on}} = 10.0 \pm 0.7$ ms and $\bar{t}_{\mathrm{off}} = 39 \pm 2$ ms.

We further studied the blinking behavior of the *same* molecule at different electrochemical potentials. We detected the enhanced fluorescence from the same single molecules at different potentials successively under the same illumination conditions as before. Figure 3.4a shows three time traces (binned to 1 ms) obtained from such a molecule, where the blinking dynamics is evidently responding to the electrochemical potential. The comparison of the traces shows that the on-time increases when the potential is increased while the off-time decreases, in accordance with the expected behavior. This general trend is observed in all the studied molecules.

To model the electrochemical switching of single molecules more quantitatively, we used the Nernst equation:

$$E = E_0 + \frac{k_{\mathrm{B}}T}{ne} \ln\left(\frac{\bar{t}_{\mathrm{on}}}{\bar{t}_{\mathrm{off}}}\right) , \tag{3.1}$$

where E is the applied potential, E_0 the mid-point potential, k_{B} the Boltzmann constant, T the absolute ambient temperature, n the number of electrons involved in the reaction, e the electron charge and $\bar{t}_{\mathrm{on}}$, $\bar{t}_{\mathrm{off}}$ the mean on and off blinking times. Figure 3.4(b) shows several

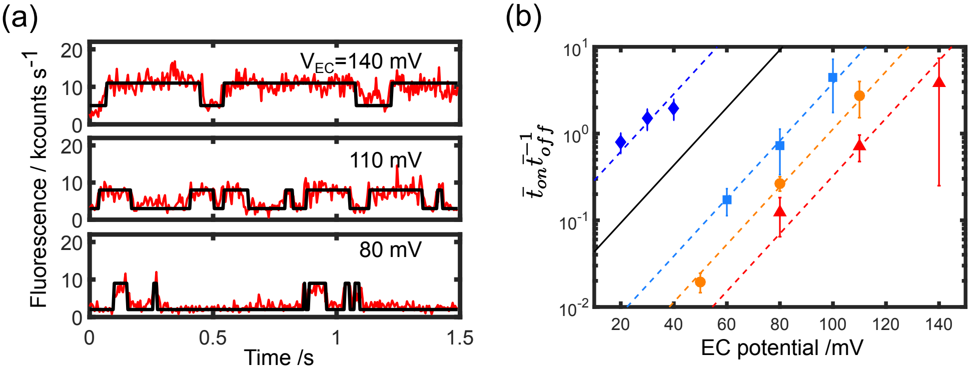

Figure 3.4: SM electrochemistry with fluorescence readout. (a) Fluorescence time traces of the same single molecule at different potentials, where different blinking dynamics can be seen. (b) The ratio $\bar{t}_{\mathrm{on}}/\bar{t}_{\mathrm{off}}$ is plotted as a function of the potential for some measured single molecules. Different symbols and colors represent different molecules. The red triangles correspond to the traces in a). The dashed lines are fits using the Nernst equation to extract the mid-point potential E_0 for each molecule, while the black solid line corresponds to the ensemble mid-point value extracted from data in Fig. 3.2(b).

$\bar{t}_{\mathrm{on}}/\bar{t}_{\mathrm{off}}$ values (symbols) and fits with the Nernst equation to obtain E_0 (dotted lines). The measured distribution of mid-point potentials for single molecules can be modeled by a Gaussian with a central value of $\left\langle E_0^{\mathrm{SM}} \right\rangle = 78.3 \pm 0.1$ mV and a dispersion of $\sigma^{\mathrm{SM}} = 21.1 \pm 0.1$ mV (see Fig. S3.5).

The average SM mid-point potential is significantly higher than the ensemble value for the laser intensity used (51 mV, see Fig. 3.2(b). To address this discrepancy, we performed the same ensemble measurements as in Fig. 3.2(b) with varying excitation intensities and observed a clear increase in mid-point potential with increasing intensity (see Fig. S3.6). This presents a possible explanation for the mentioned shift in the average mid-point potential: a molecule in the vicinity of the AuNR is excited by an enhanced field that can be as high as 300-fold [24], therefore the expected mid-point potential for such a molecule will be shifted to higher values by the strong irradiation. In order to further support this interpretation, we performed power dependence measurements on single molecules, shown in Fig. S3.7. We found that the same molecule shows higher mid-point potential when excited at higher intensity (see Fig. S3.7(a)), supporting further that laser irradiation has some influence on the redox reaction. A quantitative characterization and a mechanistic study of this photo-induced redox reaction require more experimental and theoretical work.

3.3. Conclusions

In conclusion, we have presented a scheme to study electrochemical properties of Methylene Blue at single-molecule level using fluorescence readout. Despite the low quantum yield of MB we were able to detect SM fluorescence blinking due to the high enhancement factors given by individual gold nanorods. Our single-molecule study of the *same* molecule at different redox potentials reveals that a single molecule's fluorescence emission responds to the ambient redox potential according to the Nernst equation, albeit the effective mid-point potential may be altered by the probing light. Our technique could be applied to measure the local redox potential in chemical or biological systems by single molecules and opens up the possibility of single-molecule electrochemical studies of a broader set of weakly fluorescent molecules.

3.4. Supporting information

3.4.1. Experimental setup

Combined electrochemical-optical measurements

The optical setup for fluorescence microscopy was described previously [27]. Briefly, fluorescence images and single-molecule fluorescence intensity trajectories were recorded using a home-built sample-scanning confocal microscope, equipped with an oil immersion objective (100×, NA=1.4, Zeiss), an avalanche photodiode (APD, SPCM-AQR-14, PerkinElmer) and time-correlated single-photon counting (TCSPC) electronics (Timeharp 200, PicoQuant). A 635 nm pulsed laser (LDH-P-C-635B, PicoQuant) was used for exciting the dye. A 532 nm Nd:YAG laser was used to measure the photoluminescence spectra of AuNRs, which closely resemble their scattering spectra [28]. These photoluminescence spectra were used to confirm that the nanostructure in use was an individual nanorod, which has a well-defined near-field intensity distribution.

All electrochemical experiments were carried out in a specially-designed electrochemical cell that fits the microscope. It has a gold wire connected to the gold film on the glass coverslip as the working electrode, a saturated calomel electrode as the reference electrode, a platinum wire coil as the counter electrode (see Fig.3.2(a) in the main text) and is controlled by a potentiostat (CHI832B, CH Instrument). The working solution was 100 μM phenazine ethosulfate (PES, Santa Cruz Biotechnology) dissolved in a KCl-HCl buffer (pH = 2.0, 50 mM KCl). The solution (5 mL) was inside a Teflon tube and supported by the glass sample.

Controlling the redox potential

We used the potentiostat and PES (mid-point potential E_0 = 67 mV *vs.* saturated calomel electrode at pH = 2) as an electron mediator to control the redox potential around Methylene Blue molecules. PES in the oxidized state (PES_{ox}) may receive electrons from the electrode and get reduced to PES_{red}. MB molecules studied in the experiment were very close (within 40 μm) to the working electrode (which is the gold film) [29]. In this close vicinity of the working electrode, the redox potential is controlled by the concentration ratio of $[\text{PES}_{\text{ox}}]/[\text{PES}_{\text{red}}]$, which in turn is determined by the electrical potential applied on the gold film *via* the Nernst equation. In this way, through the redox equilibrium between PES and MB, the redox potential around MB was controlled by the potential applied to the working electrode.

Since the establishment of the redox potential relies on the diffusion of the electron mediator, the actual redox potential sensed by an MB molecule is dependent on the time after an external electrical potential is applied as well as on its distance to the working electrode. In our experiments, we waited long enough time (at least 2 minutes) after applying a new potential and measured only molecules close to (within 40 μm) the edge of the gold film electrode. In this way, the measured molecules were in a redox potential which is close enough to the electrical potential applied to the gold working electrode. To test this idea

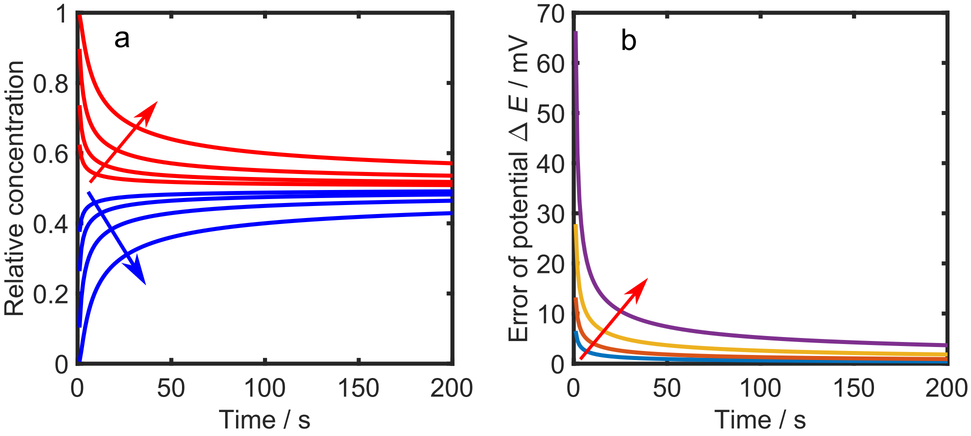

Figure S3.1: Control of the redox potential relies on the diffusion of the electron mediator. a) Calculated concentration evolution at positions with different distances to the electrode (10 μm, 20 μm, 40 μm and 80 μm) after the mid-point potential is applied at $t = 0$ to a solution of $\mathrm{PES_{ox}}$. The arrows indicate increasing distance. The concentrations of oxidized (red) and reduced (blue) PES are scaled by the original concentration of $\mathrm{PES_{ox}}$. b) Calculated error of redox potential compared to the applied potential at different distances away from the electrode (10 μm, 20 μm, 40 μm and 80 μm) after the mid-point potential is applied at $t = 0$. The arrow indicates increasing distance. The diffusion coefficient of PES in the aqueous buffer is assumed to be $5 \times 10^{-6}\mathrm{cm}^2/\mathrm{s}$ in the calculations.

more quantitatively, we assumed that the mid-point potential of PES (67 mV) is applied to a solution of $\mathrm{PES_{ox}}$ at $t = 0$. $\mathrm{PES_{ox}}$ will be reduced on the electrode surface and the concentration ratio of $[\mathrm{PES_{ox}}]/[\mathrm{PES_{red}}]$ on the electrode surface will immediately be 1. We calculated the time evolution of $[\mathrm{PES_{ox}}]$ (red) and $[\mathrm{PES_{red}}]$ (blue) near the working electrode using a linear diffusion model [29] (Fig. S3.1(a)). We see that $[\mathrm{PES_{ox}}]$ decreases while $[\mathrm{PES_{red}}]$ increases because $[\mathrm{PES_{red}}]$ generated on the electrode surface diffuses into the solution. $[\mathrm{PES_{ox}}]/[\mathrm{PES_{red}}]$ is approaching 1 over time, namely, the local redox potential is approaching 67 mV. Moreover, the local redox potential at closer distance to the electrode surface goes faster to the applied potential. We further estimated the error of the local redox potential compared to the applied potential (Fig. S3.1(b)) using

$$\Delta E = \frac{59.2\ \mathrm{mV}}{2} \log_{10} \frac{[\mathrm{PES_{ox}}]}{[\mathrm{PES_{red}}]}, \tag{3.2}$$

since 2 electrons are involved in the redox reaction. Figure S3.1b shows, for instance, that 100 s after the potential is applied, the redox potential 40 μm away from the electrode is only 2.60 mV higher than the applied potential. Therefore in our experiment we used the applied potential as the redox potential around the MB molecules.

3.4.2. Sample preparation

Gold nanorod immobilization. The average dimension of the gold nanorods (AuNRs) was 40 nm × 81 nm according to the manufacturer (Nanoseedz). The concentration of hexadecyl-trimethyl-ammonium bromide (CTAB) in the nanorod suspension was reduced

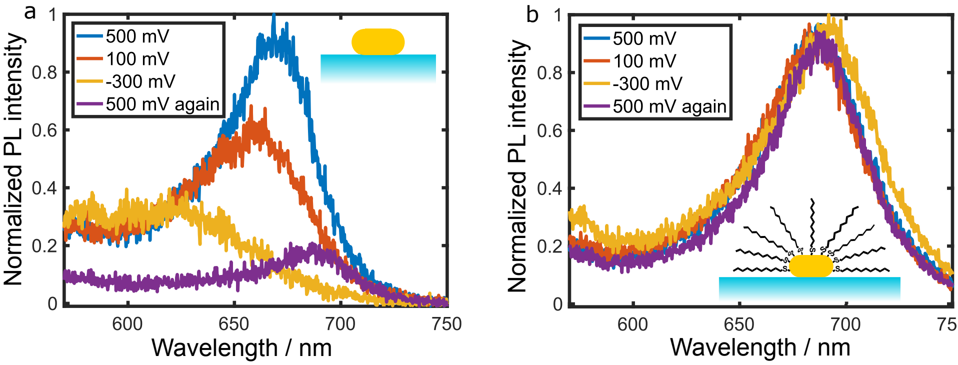

Figure S3.2: a) The PL spectra of a single bare AuNR (shown schematically in the inset) at different electrochemical potentials. The spectral changes took place within a few seconds after a new potential was applied. b) The PL spectra of a coated AuNR (shown schematically in the inset, not to scale) at different electrochemical potentials. No significant spectral changes of AuNRs could be observed after passivation.

by centrifugation and resuspension in Milli-Q water to less than 10 μM to ensure successful immobilization. Number 1 glass coverslips (Menzel-Gläser, ϕ = 25 mm) were used for all immobilizations. The coverslips were sonicated in water (20 min) and ethanol (20 min). They were then dried with a clean nitrogen flow and cleaned with ultraviolet-ozone cleaner (model 42-220, Jelight) for 30 minutes for the next step or stored in ethanol. AuNRs were immobilized on the coverslip by spin-coating from the water suspension. After that, the remaining CTAB was removed by rinsing with MilliQ water and treating with UV/Ozone for 30 minutes. The AuNRs are well isolated on the slide with a density of ~10 nanorods per 100 μm^2. Approximately 90% of the identified bright spots were measured to be single nanorods while the others stemmed from aggregates of nanorods. For SM measurements, we were only interested in molecules in the vicinity of single AuNRs, whose electromagnetic near-field is well-defined.

Gold nanorod coating. It was found experimentally that bare AuNRs were not stable during electrochemical measurements, as is evidenced by the spectral change of the AuNRs (Fig. S3.2(a)). A few seconds after the electrochemical potential was changed the photoluminescence (PL) spectrum of the AuNR shifted and the PL brightness decreased. These changes were irreversible. This issue might be the consequence of dissolution by phenazine ethosulfate when the potential is changed. Similar irreversible particle reshaping phenomena in electrochemistry experiments were reported by previous researchers [30, 31]. In order to protect the AuNRs, saturated aliphatic chains were compactly functionalized on them so that they are isolated from the ambient solution (see the inset of Fig. S3.2(b)). Experimentally, the coverslips with AuNRs were treated with a 10 mM 1-undecanethiol ($CH_3(CH_2)_{10}SH$, Sigma-Aldrich) solution in 2-propanol (Sigma-Aldrich) overnight at room temperature. The slides were then rinsed extensively with 2-propanol and dried with nitrogen. Once the AuNRs were coated in this manner, we did not observe any etching or reshaping throughout our experiments (see Fig. S3.2(b)).

Silanization of the coverslips. The coverslips with coated AuNRs were then immersed for 30 minutes with gentle stirring in a methanol solution containing 1% (3-Aminopropyl)triethoxysilane (APTES, Sigma-Aldrich) and 5% glacial acetic acid. Thereafter, the silanized slides were washed thoroughly with methanol and ethanol and dried with a nitrogen flow [32]. If not immediately used for the next step, they were stored inside a desiccator to maintain the activity of the amine groups.

Gold film sputtering. A small piece of clean glass slide (a few mm) was put at the center of every coverslip before any film was sputtered. A 2-nm-thick adhesion layer of molybdenum-germanium (MoGe) film was deposited onto the coverslips by magnetron sputtering (Z-400 system, Leybold). A 30-nm-thick gold film was immediately sputtered onto the slides in the same system. The thicknesses were estimated from the deposition rates (5.5 nm/min for MoGe and 15.2 nm/min for Au in a $<6 \times 10^{-6}$ mbar Argon environment) and times. Afterwards, the slides were taken out of the sputtering system and the small glass pieces were blown away. There were no MoGe or Au films in the area blocked by the tiny glass. Amine groups in this area were still exposed and active for immobilizing MB molecules.

Immobilization of MB molecules. Next the coverslip was placed into a circular sample holder. 1 mL solution of 300 nM MB with a N-Hydroxysuccinimide ester (NHS-ester) substituent (ATTO-TEC GmbH) in 0.1 M phosphate buffer (pH = 7.6) was applied to the coverslip. NHS-ester reacts readily with the amine groups on the coverslip to form stable amide bonds, and MB molecules thus are immobilized (depicted in Fig. S3.3). In order to accurately control the surface density of MB molecules the immobilization process was monitored *in situ*. Experimentally, the coverslip was mounted on the confocal setup and the surface close to the gold film was imaged every few minutes with the 635-nm laser. The intensity of the laser was kept low ($\sim$5 W/cm^2) to minimize photobleaching. The effective confocal volume of the optical setup was measured in a separate experiment to be 0.3 fL. With this information the count rate from an individual MB molecule was obtained by measuring the brightness of a MB NHS-ester solution of known concentration. The number of molecules per unit area was then estimated by dividing the brightness of the immobilized MB molecules by the count rate per molecule, assuming that the brightness of MB molecules does not change upon binding to the glass surface. The target molecular density is such that there is on average 1 molecule in the near-field of a AuNR. The area of the near-field in the plane of the substrate was estimated to be 40 nm$\times$20 nm$\times$2 = 1600 nm^2 considering the dimension of the AuNR. One molecule in this area corresponds to 177 molecules in the diffraction limited confocal area ($\sim$300 nm in radius). In practice, some AuNRs might have more than 1 molecule nearby but we only considered single molecules indicated by clear two-level blinking. Once the desired number of molecules is obtained, the reaction was terminated by removing the solution of MB NHS-ester. The slide was then washed several times with HCl-KCl buffer (pH = 2.0) and immediately used for electrochemistry-coupled single-molecule measurements.

3.4.3. Modeling the ensemble response to the potential

In this section we model the fluorescence response of an ensemble of $\sim$260 molecules in the focal area to the potential. The mean intensity I_m emitted by each molecule over several

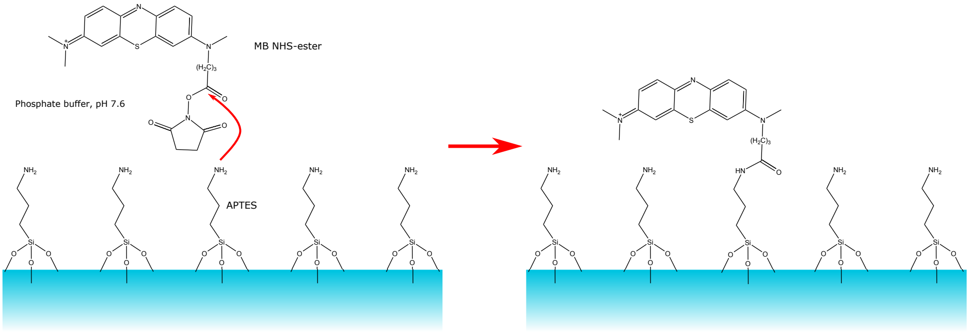

Figure S3.3: MB with a NHS-ester substituent is reacted with APTES silanized on the slide resulting in a covalent amide bond formation.

switching cycles can be calculated as

$$I_m = \langle I(t) \rangle_t = B + I_{\text{on}}^{SM} \frac{\bar{t}_{\text{on}}}{\bar{t}_{\text{on}} + \bar{t}_{\text{off}}} \,, \tag{3.3}$$

where $\langle I(t) \rangle_t$ indicates time average, B is the background intensity (200 counts s^{-1}), $I_{\text{on}}^{\text{SM}}$ is the on-intensity for one molecule and $\bar{t}_{\text{on}}$ and $\bar{t}_{\text{off}}$ are the mean on- and off-times, respectively. Since the blinking comes from the redox reaction of MB, the ratio of on- and off-times can be expressed using the Nerst equation

$$\frac{\bar{t}_{\text{off}}}{\bar{t}_{\text{on}}} = \exp\left(\frac{E_0 - V}{\alpha}\right) \,, \tag{3.4}$$

where V is the applied potential, E_0 the mid-point potential and $\alpha = \frac{k_{\text{B}}T}{ne} \approx 13$ mV.

If we assume a probability density function (PDF) $g(\zeta)$ for mid-point potentials and that all the molecules contribute with the same intensity, we can estimate the ensemble intensity distribution summing all the contributions from each single-molecule I_m weighted by this distribution:

$$\langle I_m \rangle_e (V) = B + I_{\text{on}} \int \frac{g(\zeta)}{1 + \exp(\frac{\zeta - V}{\alpha})} \mathrm{d}\zeta \,, \tag{3.5}$$

where $\langle I_m \rangle_e$ indicates ensemble averaging, B is the background signal and $I_{\text{on}} = N_{\text{molec}} I_{\text{on}}^{\text{SM}}$. The simplest model would be to have a single mid-point potential value, $\bar{E}_0$, in which case the PDF is a delta function $\delta(\zeta - \bar{E}_0)$. We fitted this simple model to our experimental data (Fig. 3.2(b) in the main text) and obtained $\bar{E}_0 = 51 \pm 4$ mV.

3.4.4. Blinking time scales

In order to extract the characteristic times associated with the fluorescence emission of SMs we calculated the autocorrelation function and found two components with clearly separated time scales as shown in Fig. S3.4. The short component ($\tau_s = 135.9 \pm 21.5$ μs) may be

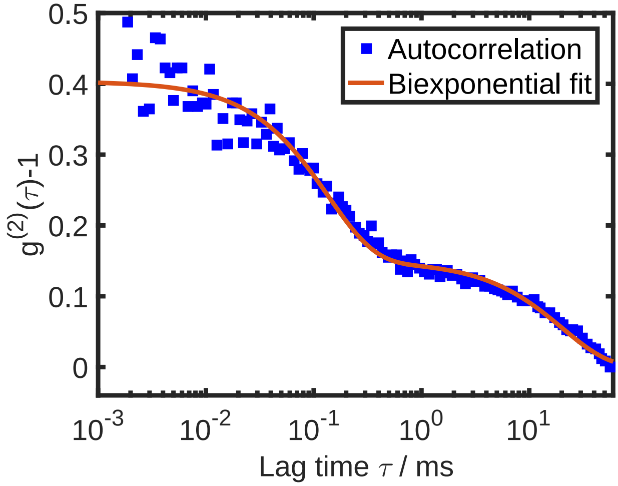

Figure S3.4: Autocorrelation traces (blue dots) measured on a AuNR-enhanced MB molecule at 120 mV with biexponential fit (red curve). The distinct short and long correlation times correspond to blinking from the triplet state and redox-induced blinking, respectively.

attributed to blinking from the triplet state as it is close to the reported triplet lifetime of MB [33]. The long component ($\tau_L = 20.3 \pm 4.6$ ms) is attributed to redox-induced blinking since the order of magnitude of this component is in the range expected for the redox reaction of MB [34, 35]. The well separated time scales allowed us to work with 1ms-binned time traces to study only the redox-induced intensity fluctuations.

3.4.5. Histogram of single-molecule mid-point potentials

In Fig. S3.5 we show the histogram of mid-point potentials for single molecules. By modeling the distribution with a Gaussian shape we get a central value of $\langle E_0^{\mathrm{SM}} \rangle = 78.3 \pm 0.1$ mV and a dispersion of $\sigma^{\mathrm{SM}} = (21.1 \pm 0.1)$ mV.

3.4.6. Dependence of the electrochemical reaction on the laser intensity

Intensity dependence of a small ensemble

To gain more insight into the dependence of MB's redox properties on laser intensity, we carried out the same ensemble measurement as shown in Fig. 3.2(b) in the main text with different excitation intensities. Ensemble-averaged mid-point potentials ($\bar{E}_0$) were obtained for each case and plotted against laser intensity in Fig. S3.6. Likewise, the figure shows that generally higher $\bar{E}_0$ values are observed if higher laser intensities were used. When the intensity is decreased, the intensity dependence of $\bar{E}_0$ reaches a plateau, where the redox state of molecules is independent of the excitation laser intensity. For a more quantitative analysis we fitted the data with a saturation curve, $\bar{E}_0(I) = E_0^{\mathrm{dark}} + C\frac{I/I_s}{1+I/I_s}$, where C is a proportionality constant, Is the saturation value and E_0^{dark} the mid-point potential in the

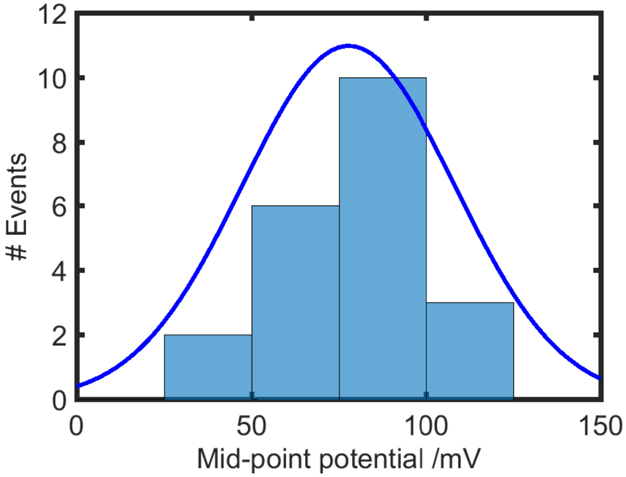

Figure S3.5: Histogram of mid-point potentials for 22 single molecules with the estimated probability distribution function with a Gaussian shape (blue solid curve).

absence of light. It is unclear to us why the two points at high intensities strongly deviate from the fit, unless this is a consequence of fast photobleaching at high intensities.

Intensity dependence of single molecules

Fluorescence emission from AuNR-enhanced single MB molecules was recorded with different excitation intensities under a fixed potential of 80 mV. Three time traces from an example molecule shown in Fig. S3.7(a) clearly evidence the dependence of oxidation/reduction dynamics on the excitation intensity. Investigation of more SMs reveals that AuNR-enhanced molecules show higher mid-point potentials under excitation of higher intensity. The intensity dependence of the measured mid-point potential is possibly a consequence of photo-induced reduction taking place in the triplet state of MB, since MB can be photo-excited to the long-lived triplet state ($\tau_{\mathrm{T}} = 450\ \mu$s) with high probability (triplet quantum yield $\phi_{\mathrm{T}} = 0.52$) [33]. This hypothesis is supported by Fig. S3.7(b), which shows that the reduction rate ($\bar{t}_{\mathrm{on}}^{-1}$) of SMs is increased by increasing the excitation intensity. The oxidation rate ($\bar{t}_{\mathrm{off}}^{-1}$), on the other hand, is independent of laser intensity as *leuco*-MB does not absorb visible light. Consequently, measured mid-point potentials of SMs are positively correlated with the laser intensity. Therefore, the on- and off-time analysis of SM fluorescence of MB overestimates the local redox potential.

3.4.7. Fluorescence enhancement analysis

The AuNR antenna in the vicinity of a MB molecule leads to fluorescence enhancement by two main mechanisms, excitation enhancement and emission enhancement. The former one arises from the high concentration of electric field at the tips of the nanorod. When a molecule is placed inside this hot spot, the local intensity can be as high as 300 times the input laser intensity, leading to an increased excitation rate. The latter enhancement mech-

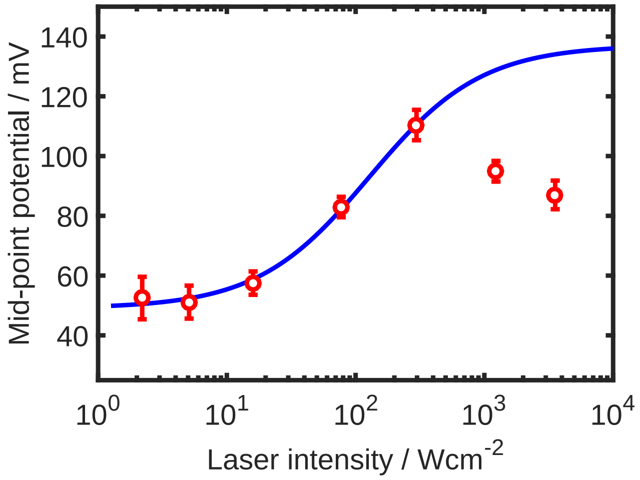

Figure S3.6: The average mid-point potential ($\bar{E}_0$) for a small ensemble depends on the laser intensity that is used for measuring. The blue is a fit according to a saturation behavior as described in the text.

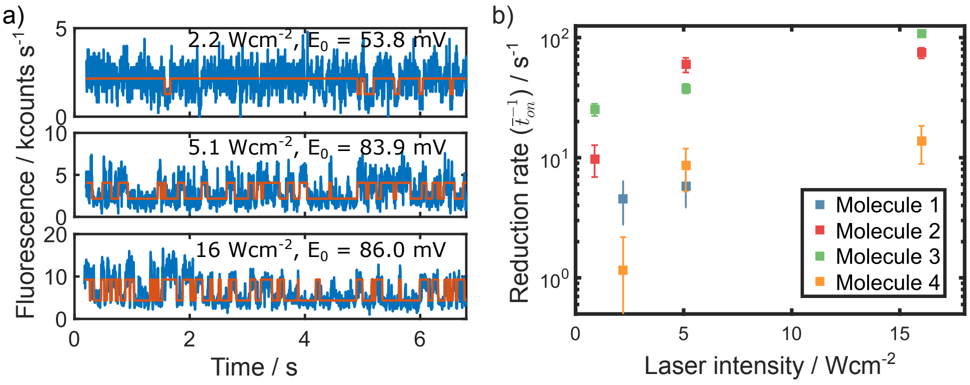

Figure S3.7: a) Fluorescence time traces recorded on the same molecule under 80 mV excited with different laser intensities. The molecule behaves differently at different excitation intensities. The red curves indicate the identified on/off state transitions. b) Reduction rates ($\bar{t}_{\mathrm{on}}^{-1}$) of four different single molecules (distinguished by different colors) under 80 mV at different laser intensities. We see a general correlation between higher reduction rate and higher intensity. Molecule 4 shown in yellow is less light-sensitive and corresponds to the molecule presented in a).

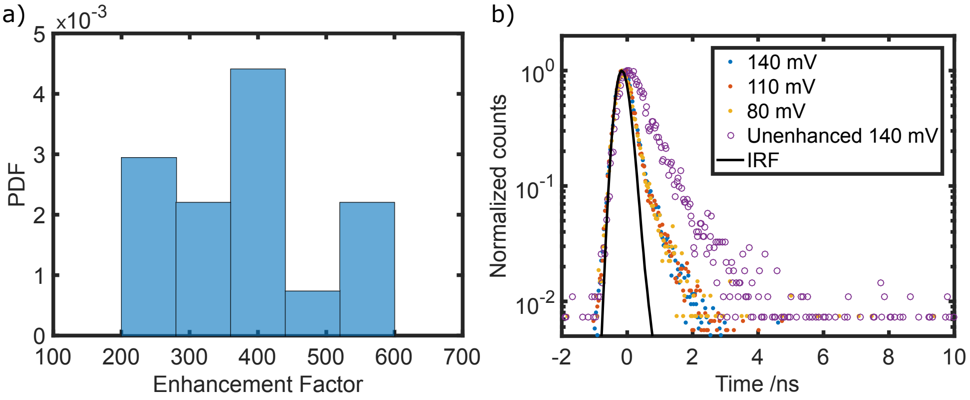

Figure S3.8: a) Total enhancement factor histogram for the 22 single molecules presented in Fig. S3.5. b) Lifetime curves for a small ensemble of unenhanced MB molecules, with a lifetime of 670 ps (open circles) and SM lifetimes for different EC potentials noted in the legend (dots). The black curve shows the IRF for our system. The enhanced lifetime remained at 360 ps regardless the applied EC potential.

anism is related to the change in the radiative and nonradiative decay rates of the molecule and depends on the distance, position, and orientation of the molecular dipole moment with respect to the local field around the AuNR and on the spectral overlap between the emitter and the nanorod [24]. We chose our AuNR sample to maximaze the overlap with the emission of MB. Regarding the dipolar orientation, due to the flexibility of the bonds that attach the MB molecules to the glass substrate, the molecules may rotationally diffuse at the end of their tether. The expected time scale for that diffusion is in the nanosecond range which is faster than any other process of interest here, so we may be observing an average of all the posible orientations. However, such process would not affect the reported values for the electrochemical quantities. Similarly, if the molecules are stuck to the surface, their orientation would be constant or vary slowly and thus would not alter the measured dynamics.

Fig. S3.8(a) shows a histogram of the total enhancement factor obtained from the SM time traces measured for this work. The enhancement factors vary from 200 to 600, a reasonable set of values for the nanorods we are using. We attribute the dispersion in values to the stochastic positioning of the molecules in the vicinity of the nanorod as well as the molecular orientation. Fig. S3.8(b) shows the comparison of the lifetime for unenhanced MB molecules and the enhanced SM data for different applied EC potentials, where a reduction in lifetime of ≈ 1.9 was measured. Notably, the lifetime is not influenced by the applied EC potential. We also show the instrument response function as a solid line.

3.4.8. Scatter plots

From our experimental data we can also extract information about correlations between the relevant parameters of the system. Firstly we look for correlations between the SM midpoint potential and the fluorescence enhancement factor. The scatter plot in Fig. S3.9 shows a positive correlation between these quantities, which is consistent with our interpretation

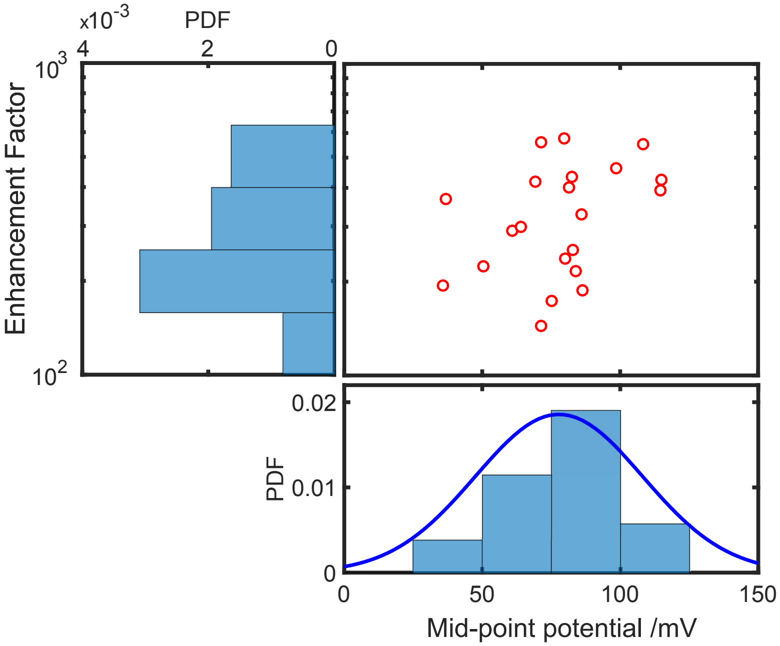

Figure S3.9: Enhancement factor as a function of measured mid-point potential at single-molecule level. Each dot in the scatter plot corresponds to one molecule. The histograms for each quantity are also shown.

of the high average mid-point potential for single molecules due to the near-field laser field. Using the data in Fig. S3.6 and the observed value $\left\langle E_0^{\mathrm{SM}} \right\rangle = 78.3$ mV we may estimate the average intensity felt by the molecules in the near field around 100 W cm^{-2}, which is a reasonable expectation value.

Secondly, we look for correlations between the mid-point potential and the enhanced fluorescence lifetime. The natural lifetime of a small ensemble MB molecules was measured to be 670 ps and due to the presence of the nanorod this lifetime is reduced. Figure S3.10 shows the scatter plot of the measured lifetime for each single molecule presented in the paper as a function of the mid-point potential. Also a histogram of lifetimes is shown. In this case no clear correlation is found between these two parameters suggesting that the electrochemical properties are not affected by a change in the population of the excited state of MB.

Finally, we correlated the single-molecule lifetime and the enhancement factors measured, as shown in the scatter plot from Fig. S3.11. As it was previously shown some degree of correlation is found since higher total enhancement factors are achieved when the lifetime reduction is stronger [24].

References

[1] W. Zhang, M. Caldarola, B. Pradhan, and M. Orrit, *Gold nanorod enhanced fluorescence enables single-molecule electrochemistry of methylene blue,* Angewandte

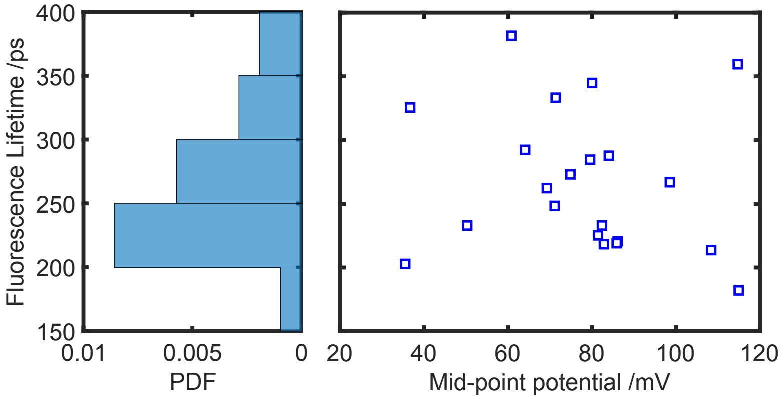

Figure S3.10: Single-molecule fluorescence lifetime as a function of measured mid-point potential. Each dot in the scatter plot corresponds to one molecule. No clear correlation is observed.

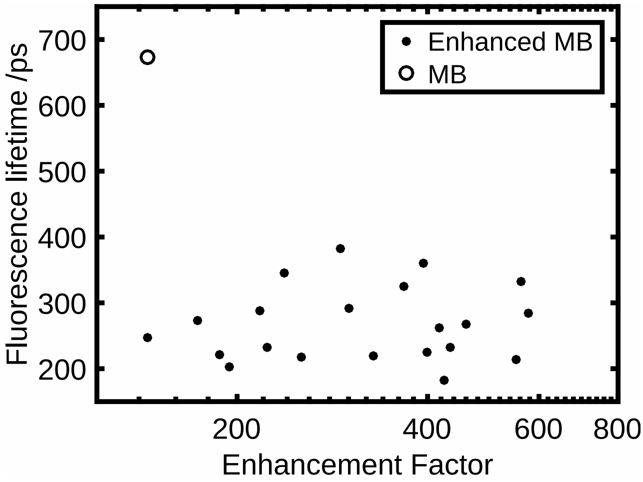

Figure S3.11: Single-molecule fluorescence lifetime vs enhancement factor. Each dot in the scatter plot corresponds to one molecule and some correlation is found between these quantities, as expected. The open circle corresponds to the unenhanced lifetime, shown for reference.

Chemie International Edition **56**, 3566 (2017).

[2] X. Mao and T. A. Hatton, *Recent advances in electrocatalytic reduction of carbon dioxide using metal-free catalysts,* Industrial & Engineering Chemistry Research **54**, 4033 (2015).

[3] M. T. Koper, *Structure sensitivity and nanoscale effects in electrocatalysis,* Nanoscale **3**, 2054 (2011).

[4] Y.-Y. Yu, S.-S. Chang, C.-L. Lee, and C. C. Wang, *Gold nanorods: electrochemical synthesis and optical properties,* The Journal of Physical Chemistry B **101**, 6661 (1997).

[5] G.-R. Li, H. Xu, X.-F. Lu, J.-X. Feng, Y.-X. Tong, and C.-Y. Su, *Electrochemical synthesis of nanostructured materials for electrochemical energy conversion and storage,* Nanoscale **5**, 4056 (2013).

[6] C. P. Byers, B. S. Hoener, W.-S. Chang, S. Link, and C. F. Landes, *Single-particle plasmon voltammetry (spPV) for detecting anion adsorption,* Nano Letters , 2314 (2016).

[7] R. H. Goldsmith, L. C. Tabares, D. Kostrz, C. Dennison, T. J. Aartsma, G. W. Canters, and W. Moerner, *Redox cycling and kinetic analysis of single molecules of solution-phase nitrite reductase,* Proceedings of the National Academy of Sciences **108**, 17269 (2011).

[8] J. M. Salverda, A. V. Patil, G. Mizzon, S. Kuznetsova, G. Zauner, N. Akkilic, G. W. Canters, J. J. Davis, H. A. Heering, and T. J. Aartsma, *Fluorescent cyclic voltammetry of immobilized azurin: direct observation of thermodynamic and kinetic heterogeneity,* Angewandte Chemie International Edition **49**, 5776 (2010).

[9] S. G. Lemay, S. Kang, K. Mathwig, and P. S. Singh, *Single-molecule electrochemistry: present status and outlook,* Accounts of Chemical Research **46**, 369 (2012).

[10] F.-R. F. Fan and A. J. Bard, *Electrochemical detection of single molecules,* Science **267**, 871 (1995).

[11] C. M. Hill, D. A. Clayton, and S. Pan, *Combined optical and electrochemical methods for studying electrochemistry at the single molecule and single particle level: recent progress and perspectives,* Physical Chemistry Chemical Physics **15**, 20797 (2013).

[12] E. Cortés, P. G. Etchegoin, E. C. Le Ru, A. Fainstein, M. E. Vela, and R. C. Salvarezza, *Monitoring the electrochemistry of single molecules by surface-enhanced raman spectroscopy,* Journal of the American Chemical Society **132**, 18034 (2010).

[13] E. Cortés, P. G. Etchegoin, E. C. Le Ru, A. Fainstein, M. E. Vela, and R. C. Salvarezza, *Strong correlation between molecular configurations and charge-transfer processes probed at the single-molecule level by surface-enhanced raman scattering,* Journal of the American Chemical Society **135**, 2809 (2013).

[14] S. Zaleski, M. F. Cardinal, J. M. Klingsporn, and R. P. Van Duyne, *Observing single, heterogeneous, one-electron transfer reactions,* The Journal of Physical Chemistry C **119**, 28226 (2015).

[15] C. Lei, D. Hu, and E. J. Ackerman, *Single-molecule fluorescence spectroelectrochemistry of cresyl violet,* Chemical Communications , 5490 (2008).

[16] M. I. F. Canto, S. Setrakian, R. E. Petras, E. Blades, A. Chak, and M. V. Sivak, *Methylene blue selectively stains intestinal metaplasia in barrett's esophagus,* Gastrointestinal Endoscopy **44**, 1 (1996).

[17] M. Wainwright and K. Crossley, *Methylene blue-a therapeutic dye for all seasons?* Journal of Chemotherapy **14**, 431 (2002).

[18] K. Kerman, D. Ozkan, P. Kara, B. Meric, J. J. Gooding, and M. Ozsoz, *Voltammetric determination of DNA hybridization using methylene blue and self-assembled alkanethiol monolayer on gold electrodes,* Analytica Chimica Acta **462**, 39 (2002).

[19] E. Farjami, L. Clima, K. V. Gothelf, and E. E. Ferapontova, *DNA interactions with a methylene blue redox indicator depend on the DNA length and are sequence specific,* Analyst **135**, 1443 (2010).

[20] L. Michaelis and S. Granick, *Metachromasy of basic dyestuffs,* Journal of the American Chemical Society **67**, 1212 (1945).

[21] N. R. de Tacconi, J. Carmona, and K. Rajeshwar, *Reversibility of photoelectrochromism at the TiO_2/methylene blue interface,* Journal of the Electrochemical Society **144**, 2486 (1997).

[22] J. Olmsted, *Calorimetric determinations of absolute fluorescence quantum yields,* The Journal of Physical Chemistry **83**, 2581 (1979).

[23] D. Punj, J. de Torres, H. Rigneault, and J. Wenger, *Gold nanoparticles for enhanced single molecule fluorescence analysis at micromolar concentration,* Optics Express **21**, 27338 (2013).

[24] S. Khatua, P. M. Paulo, H. Yuan, A. Gupta, P. Zijlstra, and M. Orrit, *Resonant plasmonic enhancement of single-molecule fluorescence by individual gold nanorods,* ACS Nano **8**, 4440 (2014).

[25] B. Pradhan, S. Khatua, A. Gupta, T. Aartsma, G. Canters, and M. Orrit, *Gold-nanorod-enhanced fluorescence correlation spectroscopy of fluorophores with high quantum yield in lipid bilayers,* The Journal of Physical Chemistry C **120**, 25996 (2016).

[26] B. Shuang, D. Cooper, J. N. Taylor, L. Kisley, J. Chen, W. Wang, C. B. Li, T. Komatsuzaki, and C. F. Landes, *Fast step transition and state identification (STaSI) for discrete single-molecule data analysis,* The Journal of Physical Chemistry Letters **5**, 3157 (2014).

[27] B. Pradhan, S. Khatua, A. Gupta, T. Aartsma, G. Canters, and M. Orrit, *Gold-nanorod-enhanced fluorescence correlation spectroscopy of fluorophores with high quantum yield in lipid bilayers,* The Journal of Physical Chemistry C **120**, 25996 (2016).

[28] M. Yorulmaz, S. Khatua, P. Zijlstra, A. Gaiduk, and M. Orrit, *Luminescence quantum yield of single gold nanorods,* Nano Letters **12**, 4385 (2012).

[29] A. Bard and L. Faulkner, *Electrochemical Methods: Fundamentals and Applications* (Wiley, 2000).

[30] B. S. Hoener, C. P. Byers, T. S. Heiderscheit, A. S. De Silva Indrasekara, A. Hoggard, W.-S. Chang, S. Link, and C. F. Landes, *Spectroelectrochemistry of halide anion adsorption and dissolution of single gold nanorods,* The Journal of Physical Chemistry C **120**, 20604 (2016).

[31] C. P. Byers, B. S. Hoener, W. S. Chang, M. Yorulmaz, S. Link, and C. F. Landes, *Single-particle spectroscopy reveals heterogeneity in electrochemical tuning of the localized surface plasmon,* Journal of Physical Chemistry B **118**, 14047 (2014).

[32] A. Gupta, T. J. Aartsma, and G. W. Canters, *One at a time: Intramolecular electron-transfer kinetics in small laccase observed during turnover,* Journal of the American Chemical Society **136**, 2707 (2014).

[33] S. L. Murov, I. Carmichael, and G. L. Hug, *Handbook of photochemistry* (CRC Press, 1993).

[34] S. Mowry and P. J. Ogren, *Kinetics of methylene blue reduction by ascorbic acid,* Journal of Chemical Education **76**, 970 (1999).

[35] J. R. Sutter and W. Spencer, *An equilibrium and kinetic-study of the methylene blue-ferrocyanide reaction in acid-medium,* Journal of Physical Chemistry **94**, 4116 (1990).

4

Enhancement of hot-band absorption anti-Stokes luminescence of single molecules by individual gold nanorods

Frequency upconversion luminescence is an optical process that converts long-wavelength excitation to short-wavelength emission. Upconversion materials are especially suited for bio-imaging applications because anti-Stokes shift luminescence leads to reduced background from auto-fluorescence of biological tissues. Here we demonstrate anti-Stokes luminescence from a commercial squaraine dye, Seta 670. The luminescence is induced by optical absorption from a vibrational hot-band. We use individual chemically-synthesized gold nanorods to enhance the anti-Stokes emission intensity of single Seta 670 molecules and obtain an enhancement factor of 350.

4.1. Introduction

Fluorescence-based light microscopy continues to develop as an indispensable tool in material science and biology because of, among others, its high contrast since photons are emitted at a different wavelength than the excitation photons. Specially, fluorescence microscopy has the sensitivity of detecting exceedingly low concentrations of molecules, down to the single-molecule level. Demonstration of optical detection of single-molecule fluorescence marked a major breakthrough in the field of optics [1]. It greatly extended the scope of fluorescent microscopy, providing unprecedented insights into complex systems where static and dynamic heterogeneity is present [2–4].

Over the decades, imaging probes of various kinds have been developed, including synthetic organic dyes, fluorescent biomolecules (notably green fluorescent proteins), and semiconductor nanocrystals. Recently, frequency upconversion materials have attracted much attention because of the anti-Stokes shift of the emission wavelength with respect to the excitation wavelength. This feature makes them especially interesting for bio-imaging applications because of the reduced background from auto-fluorescence of biological tissues. Moreover, upconversion emission usually involves near-infrared (NIR) excitation, which has a larger penetration depth into tissues. Three different materials and mechanisms can generate anti-Stokes emission [5] (i) multi-photon absorption, which usually requires femtosecond pulsed lasers for extremely high excitation energy. (ii) lanthanide- and triplet-triplet annihilation-based upconversion nanoparticles; (iii) hot-band absorption induced luminescence, where a molecule is excited to the lowest excited state from a higher vibrational energy level (termed "hot band") and emit photons whose wavelength is shorter than that of the excitation photons. The mechanism is illustrated in Fig. 4.1(a) with a Jablonski diagram. In hot-band absorption induced luminescence, the additional energy is provided by thermal energy, therefore hot-band absorption is usually accompanied by a concomitant decrease in the temperature of the system. Such a feature gives rise to applications in laser cooling [6, 7]. Hot-band absorption is a linear process, which does not require expensive ultrafast lasers. Hot-band absorption anti-Stokes luminescent materials are typical dye molecules. Their nanometer size features a major advantage as fluorescent probes over bulky optical probes such as quantum dots, metal nanoparticles and upconversion nanoparticles in that they have minimum effects on the motion, localization and interactions of tagged objects, which is highly desired for fluorescence correlation spectroscopy, single-molecule imaging, *etc*. However, the application of this anti-Stokes luminescence in microscopy is hampered by its low efficiency, *i.e.*, low luminescence brightness. Only a limited number of dyes have demonstrated hot-band absorption anti-Stokes emission [5, 8], mainly because there is no rational rule for designing such molecules with better brightness.

It has been long known that metallic nanostructures, such as nanospheres [9], bow-ties [10] or nanorods [11, 12], are able to enhance the fluorescence emission of a single adjacent molecule. The gain in the detected fluorescence arises from the combined excitation and emission rate enhancement. The former comes form the highly concentrated electric fields produced around these nanostructures due to the resonant excitation of surface plasmons [13], while the later arises from the modification of the radiative decay rate [9], similar to the effect of a metallic surface [14]. In the present work, we demonstrate the possibility of enhancing hot-band absorption induced luminescence by chemically synthesized gold

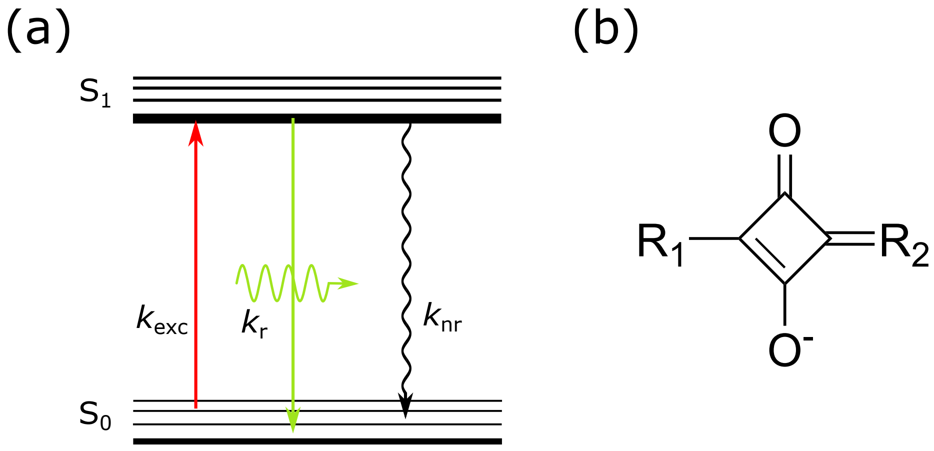

Figure 4.1: (a) Jablonski diagram illustrating the mechanism of hot-band absorption induced luminescence. k_{exc}: excitation rate; k_{r}: radiative rate; k_{nr}: nonradiative rate; (b) General chemical structure of squaraine dyes.

nanorods. The molecule in our study is a commercial squaraine dye, Seta 670. Squaraines are a class of fluorophores with a characteristic squarylium core flanked by nucleophilic motifs (Fig. 4.1(b)). They are extensively used for fluorescent labeling because of their strong red/NIR absorption and emission and excellent photostability [15–18]. Here we show that the hot-band absorption induced luminescence of such dyes can be enhanced by gold nanorods. We measured an enhancement factor of 350 for single Seta 670 molecules. Our findings open the potential of increasing the sensitivity of anti-Stokes luminescence-based imaging and extending single-molecule spectroscopy to a relatively unexplored type of luminescence.

4.2. Materials and methods

Materials. Spectroscopy grade methanol (99.9%) was purchased from Alfa Aesar. Seta 670 containing one reactive NHS-ester group (Seta-670-NHS) was purchased from SETA BioMedicals (Urbana, USA). Gold nanorods were from Nanopartz Inc. Their average dimensions were 38 nm × 118 nm as obtained from the transmission electron microscopy image provided by the manufacturer. Gold nanorods were immobilized onto a microscope coverslip with a spin-coating method described elsewhere [11, 19]. The coverslip was mounted in a home-made sample holder, where the dye solution can be added for further optical measurements. A second cover glass was placed immediately on top to prevent solvent evaporation.

Bulk absorption and fluorescence spectroscopy. UV-Vis absorbance measurements were performed using a Cary 50 spectrophotometer (Varian Analytical Instruments, USA). Bulk emission spectra in solution were recorded with a Cary Eclipse fluorescence spectrophotometer (Varian Analytical Instruments, USA). The temperature of the solutions in the cuvette was controlled by a single-cell Peltier accessory (Varian Analytical Instruments, USA).

Single-particle spectroscopy was performed on a confocal microscopy setup described in detail in the Supporting Information. Briefly, we used a mode-locked titanium-sapphire laser (775 nm wavelength and 220 fs pulse width) with circular polarization to excite fluorescence from the molecules in a custom-built confocal microscope equipped with time-correlated single-photon counting (TCSPC) electronics (TimeHarp 200, PicoQuant GmbH, Berlin). For continuous-wave (CW) laser excitation, we switched the titanium-sapphire laser to the CW mode and kept the same wavelength. The laser wavelength is in resonance with the longitudinal plasmon of the nanorods (Fig. 4.4), generating a strongly enhanced local field for fluorescence enhancement. The plasmon resonance of each gold nanorod is determined by measuring the one-photon-excited photoluminescence spectrum excited by a 532-nm continuous-wave (CW) laser. Apart from more commonly used scattering spectra, photoluminescence spectra have been proven and used as an alternative method of measuring the plasmon resonances [20, 21].

Imaging and time trace recording. Immobilized nanorods were brought into the focus of the microscope and a typical area of 30×30 μm^2 was imaged with the Ti:Sapphire laser (see Fig. S4.6(c)). Gold nanorods were identified by their strong two-photon-excited photoluminescence. Figure S4.6 shows a typical spectrum of the two-photon-excited photoluminescence from a nanorod and the dependence of the luminescence intensity on the laser power. We selected only single gold nanorods which are evidenced by the Lorentzian one-photon photoluminescence spectral shape (measured with the 532-nm CW laser) for further measurements and analyses. Then a solution of 1 μM Seta 670 in methanol was applied to the sample. The titanium-sapphire laser was focused on the single nanorods and photons were recorded in time-ragged-time-resolved mode and further analyzed with SymPhoTime software. The autocorrelation analyses were performed with the raw single-photon data instead of the binned time traces.

4.3. Results and discussion

4.3.1. Optical characterization at room temperature

We first characterized the optical properties of Seta 670 by the bulk absorption and emission spectra measurements at room temperature. Figure 4.3(a) shows the UV-Vis absorption spectra of a diluted methanol solution (1 μM) of Seta 670. Seta 670 shows a narrow principal absorption band at 684 nm and a vibronic shoulder at around 630 nm. Strikingly, we observe that the emission spectrum of Seta 670 is dependent on the concentration of the solution. If the concentration is 1 μM or lower, the emission peak is at 704 nm, whereas the emission peak shifted to 720 nm when we increased the concentration to 100 μM (Fig. 4.2(a)). Figure S4.4 in the Supporting Information shows emission spectra measured with more concentrations, where the gradual red-shift is visualized when increasing the concentration. Such a concentration dependence is most probably a result of reabsorption due to the large overlap of the absorption and emission spectra [6].

We observed blue-shifted anti-Stokes emission from Seta 670 when exciting the long-energy tail of the absorption spectrum. Figure 4.2(b) shows the emission spectra of a 100 μM methanol solution of Seta 670 excited at 775 nm and 785 nm. The excitation was achieved

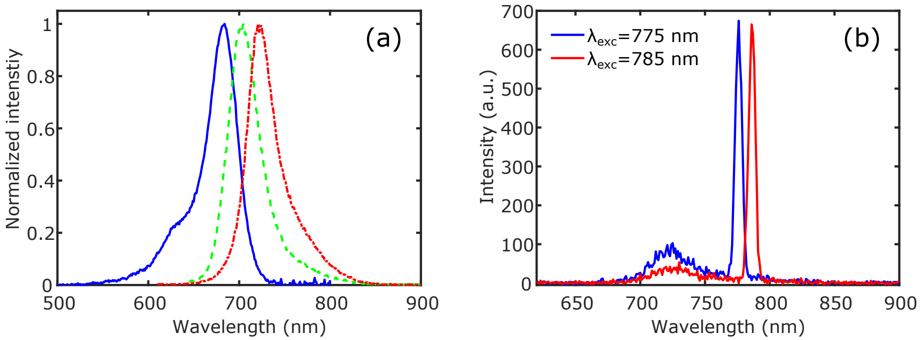

Figure 4.2: **Optical characterization of Seta 670 at room temperature**. (a) The blue solid line and dashed green line shows the absorption and Stokes fluorescence emission spectra of 1 μM Seta 670 in methanol, respectively. The red dot-dashed line shows the Stokes fluorescence emission spectrum of 100 μM Seta 670 in methanol. (b) Anti-Stokes luminescence spectra of Seta 670 (100 μM in methanol) excited at 775 nm and 785 nm. The high peaks at the excitation wavelengths were from the scattering of the solution.

by selecting the desired wavelength from the lamp of the spectrophotometer. An anti-Stokes emission peak at 720 nm was observed, irrespective of the excitation wavelength. The anti-Stokes emission wavelength is the same as the Stokes emission at the same concentration.

4.3.2. Temperature-dependent optical characterization

We then performed the temperature-dependent measurements to reveal the mechanism of anti-Stokes emission from Seta 670. Figure 4.3(a) shows the UV-Vis absorption spectra of 1 μM Seta 670 at different temperatures. The two absorption peaks do not shift upon temperature change. However, lower absorbance and broader spectra are seen as the temperature increases from 278.5 K to 333 K. There is a clear isosbestic point at $\sim$ 703 nm. Two other isosbestic points at $\sim$642 nm and $\sim$ 650 nm are less clear because they are too close to each other. See Fig. S4.3 for a zoom-in of the absorption spectra. The intensity decrease and spectral broadening were explained by Clark *et al.* with the Boltzmann distribution [6, 8]. Briefly, at low temperatures, most molecules tend to lie in the lowest possible state. As the temperature increases, the distribution over energy states becomes more uniform, so the absorption bands become broader in shape and lower in amplitude.

We then measured the fluorescence emission spectra of Seta 670 with an excitation wavelength of 650 nm. The dependence on temperature of the fluorescence spectra is shown on Fig. 4.3(a). This excitation wavelength was chosen because the absorbance at this wavelength does not dependent on the temperature. The princial emission band around 704 nm does not shift upon temperature change. The fluorescence intensity, however, decreases dramatically when the temperature was increased, which is attributed to the decrease of fluorescence quantum yield (QY) as the temperature was increased. We measured the quantum yield of the Stokes emission of Seta 670 at different temperatures (Fig. 4.3(b)). The quantum yield was determined using Seta 670 in pH 7.4 phosphate buffer as a reference sample with a known QY of 0.07 (at 298 K) provided by the manufacturer. The measured values

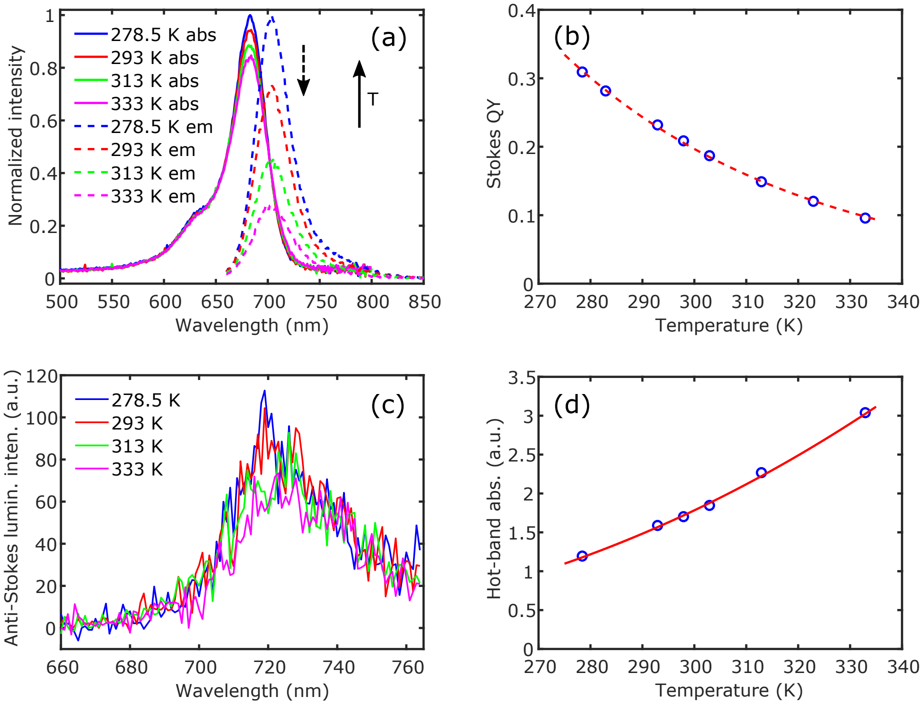

Figure 4.3: **Optical characterization of Seta 670**. (a) Absorption and Stokes fluorescence emission spectra of 1 μM Seta 670 in methanol at different temperatures. The absorption spectra have been normalized relative to the highest absorption spectrum and the emission spectra have been normalized relative to the highest emission spectrum. The excitation wavelength for the emission spectra was 650 nm. (b) Quantum yield of Stokes fluorescence of Seta 670 as a function of temperature. The dashed red line is an empirical exponential fit to the experimental data. (c) Anti-Stokes luminescence spectra of Seta 670 at different temperatures (λ_{exc} = 775 nm). (d) Hot-band absorption efficiency as a function of temperature (λ_{exc} = 775 nm). The red line shows an exponential fit to equation 4.1.

of quantum yield against temperature can be well fitted by an empirical single-exponential relation. The temperature dependent quantum yield is usually attributed to more efficient non-radiative processes related to thermal agitation at higher temperatures [22].

Figure 4.3(c) shows the emission spectra of a 100 μM methanol solution of Seta 670 at different temperatures (λ_{exc} = 775 nm). From Fig. 4.3(c) it is seen that the emission intensity of anti-Stokes increases slightly with decreasing temperature, which is not what we expect for hot-band absorption.This paradox can be solved by taking into account the temperature dependence of quantum yield shown in Fig.4.3(b). The lower anti-Stokes absorption at low temperatures is compensated by the higher quantum yield, resulting in a higher anti-Stokes emission. We divided the integrated anti-Stokes luminescence intensity by the quantum yield for the corresponding temperatures. The results are representative of the absorption efficiency at 775 nm (and the absolute values are not important). The absorption efficiency increases as the solution temperature increases (Fig. 4.3(d)). We fitted the results with an exponential function:

$$I(T) = A\exp(-\Delta E/k_{\mathrm{B}}T), \tag{4.1}$$

where $I(T)$ is the relative hot-band absorption efficiency as a function of solution temperature T, k_{B} the Boltzmann constant, and A a proportionality coefficient. The thermal activation energy ΔE was determined from the fitting to be 138 meV, in good agreement with the difference between the excitation energy and the upconversion emission energy (134 meV). The anti-Stokes luminescence intensity excited with 785 nm was weaker than with 775 nm (Fig. 4.2(b)) due to the larger energy barrier. The results clearly confirms that the anti-Stokes emission from Seta 670 really originates from the optical excitation of a thermally populated vibration level (hot band).

4.3.3. Femtosecond laser excitation

Because of their donor-acceptor-donor structures, squaraine dyes have been found to have strong two-photon absorption and emission. The two-photon action cross-sections are comparable with those of semiconducotor quantum dots, whereas the size is much smaller than the latter [16, 23]. Therefore squaraine dyes have been proposed as promising fluorescent molecular probes in biological two-photon microscopy. Here we compared the blue-shifted emission excited with a CW laser (λ_{exc} = 775 nm) and that with a femtosecond pulsed laser (λ_{exc} = 775 nm) and found no evidence of two-photon-excited emission. As Fig. 4.4(a) illustrates, the intensity of emission under femtosecond excitation shows no difference from that under continuous-wave excitation at the same excitation power. Moreover, in both cases, the intensity of emission is a linear function of the excitation power. The blue spectrum shown in Fig. 4.4(b) shows the emission spectrum of Seta 670 excited with the femtosecond laser, which is identical with that excited with CW excitation. The results suggest that under our experimental conditions, the emission from Seta 670 with femtosecond pulsed excitation also stems from linear hot-band absorption. The contribution from two-photon absorption, if present at all, is negligible.

4.3.4. Enhancing hot-band absorption using gold nanorods

In the following, we used gold nanorods to enhance the upconversion luminescence of single Seta 670 molecules. We have proven that the anti-Stokes emission under CW and pulsed excitations stem from the same origin, so we used the pulsed laser to do the enhancement experiments with time-correlated single-photon counting electronics. The nanorods used in our study were the same as described in Chapter 2. The longitudinal surface plasmon resonance of the nanorods was 770 nm. For single-particle studies with the confocal microscope, the nanorods were well isolated and immobilized on a glass coverslip. The spectra of the nanorods exhibit good overlap with the excitation wavelength (775 nm) and some overlap with the emission of the dye, ensuring a high expected enhancement factor [11, 24].

Single isolated gold nanorods immobilized on a glass coverslip were immersed in a 1 μM methanol solution of Seta 670 and brought to the focus of the microscope. Figure 4.5(a) shows a typical time trace taken on a single nanorod, where signal bursts are identified. We attribute these bursts to enhanced anti-Stokes luminescence emission of single Seta 670 molecules when freely diffusing molecules approach the near field of the gold nanorod. The

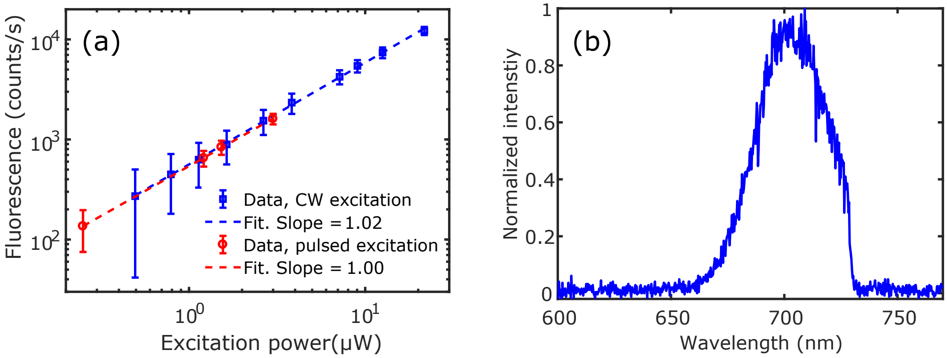

Figure 4.4: (a) Log-log plot showing the linear dependence of anti-Stokes emission of Seta 670 in methanol on the average excitation intensity under continuous-wave (blue) and pulsed (red) excitation. The wavelengths for continuous-wave and pulsed excitation were both 775 nm. The concentration of Seta 670 for the CW measurement was 1 μM. The concentration for the measurement with a pulsed laser was 5 μM and the fluorescence intensity has been scaled to 1 μM assuming a linear relation of fluorescence with concentration. (b) The emission spectrum of 5 μM Seta 670 in methanol excited by a 775-nm femtosecond laser. A 745-nm shortpass filter was used to cut the excitation wavelength.

corresponding autocorrelation is shown in Fig. 4.5(b). The autocorrelation is apparently non-exponential with no well-defined characteristic correlation time. Nevertheless, we fitted the autocorrelation to a single exponential and obtained a correlation time of 5.4 ms. As found out by previous works [10, 11, 24, 25], this correlation time is too long to be due to the free diffusion of molecules through the near field of a nanorod. It is most likely a result of the transient sticking (and subsequent photobleaching or desorption) of dye molecules to the glass substrate. The stretched decay behavior of the autocorrelation curve is attributable to the lack of a characteristic time scale for the non-specific sticking.

The background signal in the time trace, 3,800 counts/s, comes from all the unenhanced Seta 670 molecules in the focal volume and two-photon-excited luminescence of the nanorod. The contribution of dye molecules can be measured by recording a time trace on an area without a nanorod under the same experimental conditions. Such a time trace is also present in Fig. 4.5(a) with an average count rate of $\sim$ 1,000 counts/s. No significant fluorescence bursts higher than the photon noise can be seen. The corresponding autocorrelation curve shown in Fig. 4.5(b) does not show any correlation. This is expected because with a measured focal volume of 0.09 fL (Supporting Information) and a given dye concentration of 1 μM, we estimate on average 54 molecules in the focal volume. With such a high number of molecules, we do not expect any visible signal fluctuations above the experimental noise or any visible correlation contrast due to molecules diffusing in and out of the detection volume.

With the number molecules present in the detection volume, we can further estimate the average count rate of one molecule without enhancement to be 18.8 ± 0.2 counts/s. The count rate of the most intense signal burst (indicated by an arrow) shown in Fig. 4.5(a) is 10,400 counts/s against a background of 3,800 counts/s. This burst is due to the enhanced anti-Stokes luminescence emission, 6,600 counts/s, from a single Seta 670 molecule. Based on this, we can calculate an enhancement factor of 350.

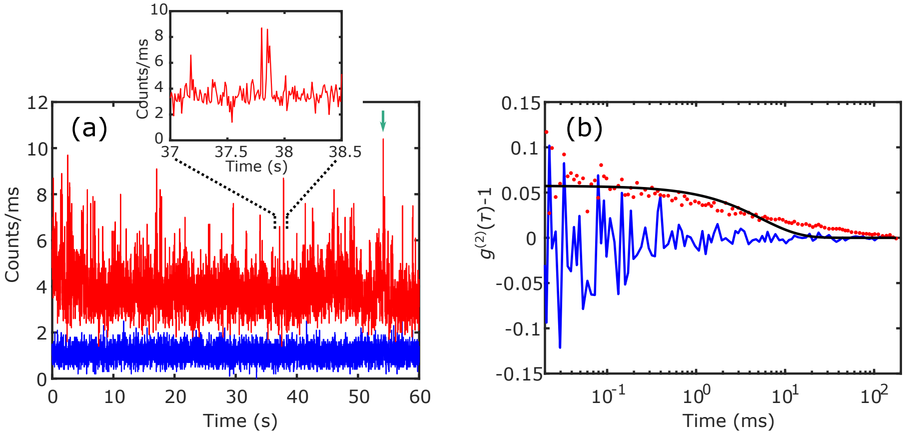

Figure 4.5: (a) Fluorescence time traces (10 ms per bin) taken on a nanorod (red dots) and on the background where no nanorod was present (blue line). The average excitation power of the pulsed laser was 1.5 μW at the sample. The inset figure is an expansion of part of the trace. (b) Autocorrelation curves of the measurements (colors correspond to (a)). The measurement on the background showed no correlation because of the high concentration of dye. An exponential fit (black solid line) to the red dots yields a correlation time of 5.4 ms, clearly longer than that takes for a molecule to diffuse through the near field of the nanorod.

4.4. Conclusion

In summary, we have characterized the hot-band absorption anti-Stokes luminescence of a squaraine dye. We have demonstrated the feasibility of enhancing anti-Stokes luminescence of single dye molecules using chemically synthesized gold nanorods. An enhancement factor of 350 was achieved by using nanorods with a plasmon resonance close to the excitation wavelength. Thanks to the sub-wavelength detection volume defined by the strong near field around the nanorods, fluorescence correlation spectroscopy could be performed even at a dye concentration of 1 μM, yielding a correlation time associated with the sticking or bleaching time of molecules on the glass substrate.

4.5. Supporting information

Schematic of the optical setup

Confocal microscopy measurements were performed on our home-built sample-scanning confocal fluorescence microscope (Fig. S4.1). A mode-locked titanium-sapphire laser (Coherent Mira 900) was made circularly polarized by a quarter-wave plate (not shown in the scheme) before entering the oil immersion objective (100×, NA = 1.4, Zeiss), and used for excitation. It was spatially filtered and expanded to overfill the aperture of the objective. The laser operated at 775 nm, 76 MHz repetition rate and 220 fs pulse width. The photoluminescence signal of Seta 670 molecules and/or gold nanorods collected by the same objective was filtered out from the back-scattered excitation light by a 745-nm short-pass filter (FF01-745/SP-25, Semrock) and a 785-nm notch filter (NF03-785E-25, Semrock). A multimode optical fiber with a core size of 62 μm was used as a confocal pinhole. A 532-

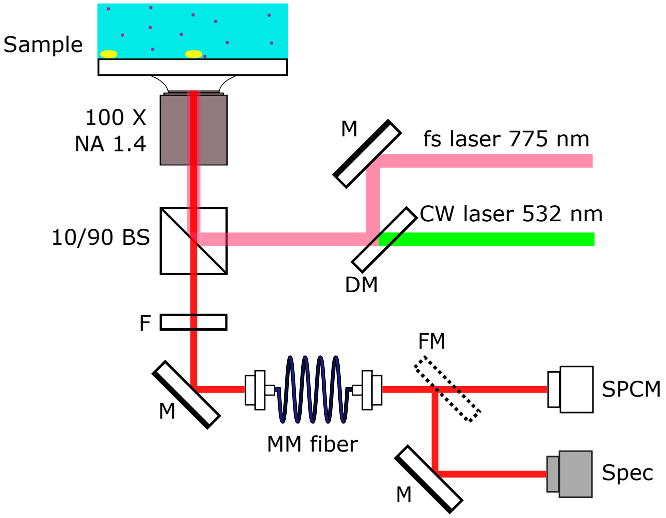

Figure S4.1: Schematic of the experimental setup for confocal microscopy and luminescence spectra measurements. BS - beam splitter, F - Set of filters: 745 nm short-pass filter + 785 notch filters for the titanium:sapphire laser or two 532 nm notch filters for the 532-nm laser, M - mirror, DM - dichroic mirror, FM - flip mirror, MM fiber - multimode fiber, SPCM - single-photon counting module, Spec - spectrometer. Waveplates and spatial filters are not shown in the scheme.

nm diode-laser-pumped solid-state continuous-wave laser (Shanghai Laser & Optics Century Co., Ltd), which matches the transverse plasmon resonance of nanorods, was used to measure the one-photon excited photoluminescence spectrum of each nanorod. For this, two 532-nm notch filters were used in place of the 745-nm shortpass and 785-nm notch filters. We used circular polarization to find nanorods regardless of their orientation. It was previously shown that nanorods' one-photon photoluminescence spectra closely resemble their scattering spectra [20], so photoluminescence is used to determine the resonance wavelengths. The near-infrared and green laser beams were overlapped with a shortpass dichroic mirror (FF720-SDi01-25×36, Semrock). Note that the two lasers were not used at the same time. We used a motorized flip mirror to direct luminescence either to a single-photon counting module (SPCM-AQR-16, PerkinElmer) or to a spectrometer equipped with a liquid-nitrogen-cooled CCD (Acton SP-500i, Princeton Instruments).

Size of the confocal volume

We measured the size of the confocal volume by measuring the point spread function (PSF) of the microscope [26]. We scanned sectional scattering images of an immobilized gold nanorod immersed in index-matching objective oil excited with the Ti:Sapphire laser. No detection filters were used. Figure S4.2 shows the xz section of the PSF (z is along the optical axis). All three sections (xy, xz and yz) of the PSF were fitted with two-dimensional Gaussian functions as described in Chapter 2. The size of the confocal volume is then calculated from the mean dimensions in each axis as

$$V_{\text{conf}} = \left(\frac{\pi}{2}\right)^{3/2} w_x w_y w_z = 0.089 \pm 0.005 \text{ fL}, \tag{4.2}$$

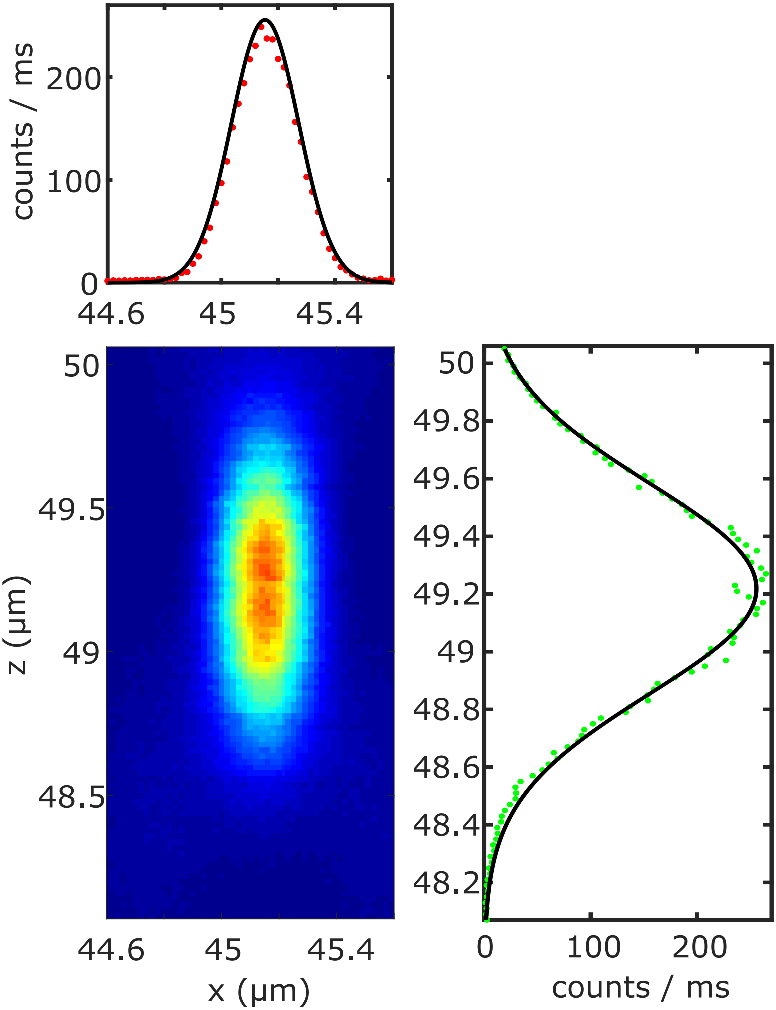

Figure S4.2: ***xz* section of the scattering PSF measured with a gold nanorod**. Line profiles through the center are shown. The red (along the x axis) and green (along the z axis) dots show the experimental data and the black lines represent two-dimensional Gaussian fits, which yield $w_x = 237.0 \pm 1.4$ nm and $w_z = 731.1 \pm 4.4$ nm.

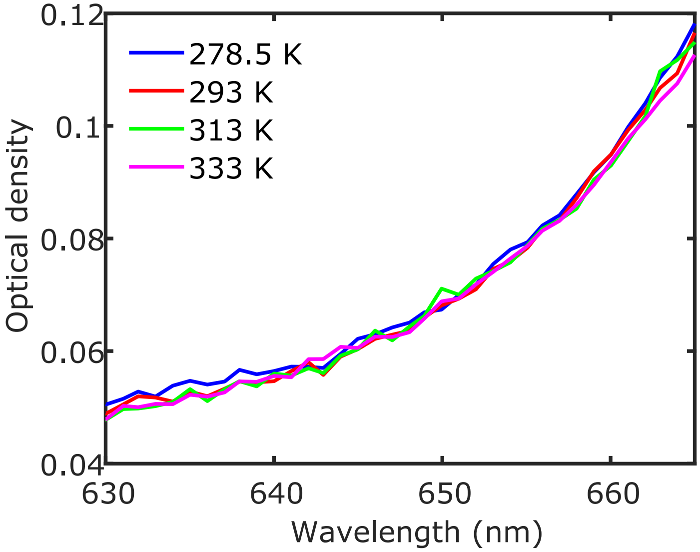

Figure S4.3: Detailed absorbance spectra of 1 μM Seta 670 as a function of temperature. It is a zoom-in plot of Fig. 4.3(a) in the main text. Two other isosbestic points at ~642 nm and ~ 650 nm are less clear because they are too close to each other.

where w_x, w_y and w_z are the $1/e^2$ radii along *x*, *y* and *z* axis, respectively.

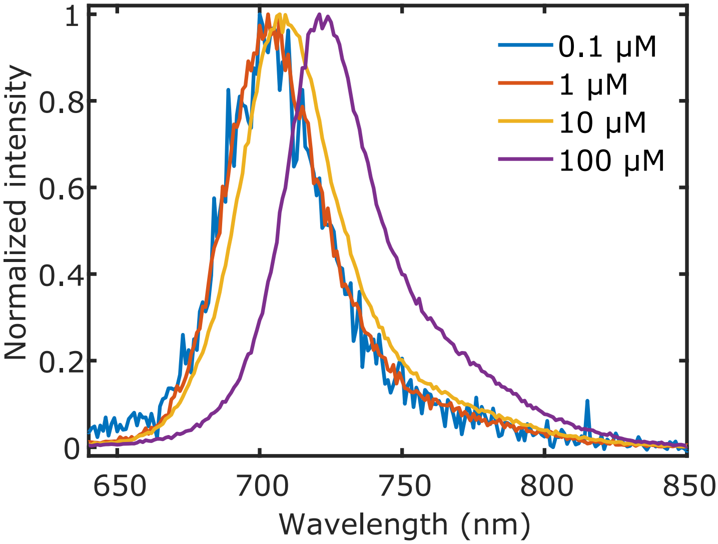

Figure S4.4: Concentration dependence of the Stokes fluorescence spectra of Seta 670. If the concentration is 1 μM or lower, the emission peak is at 704 nm. The emission peaks moves 710 nm if the concentration is increased to 10 muM. The 100 μM solution shows an emission peak at 720 nm. Such a concentration dependence is most probably a result of reabsorption due to the large overlap of the absorption and emission spectra [6].

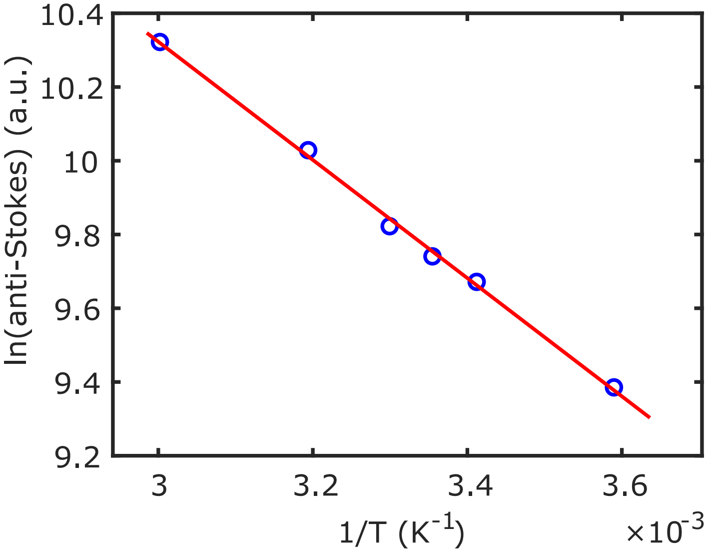

Figure S4.5: Linear plots of logarithm of integrated fluorescence intensity against inverse temperature of Seta 670 solution. The data are the same as shown in Fig. 4.3(d) in the main text but presented differently.

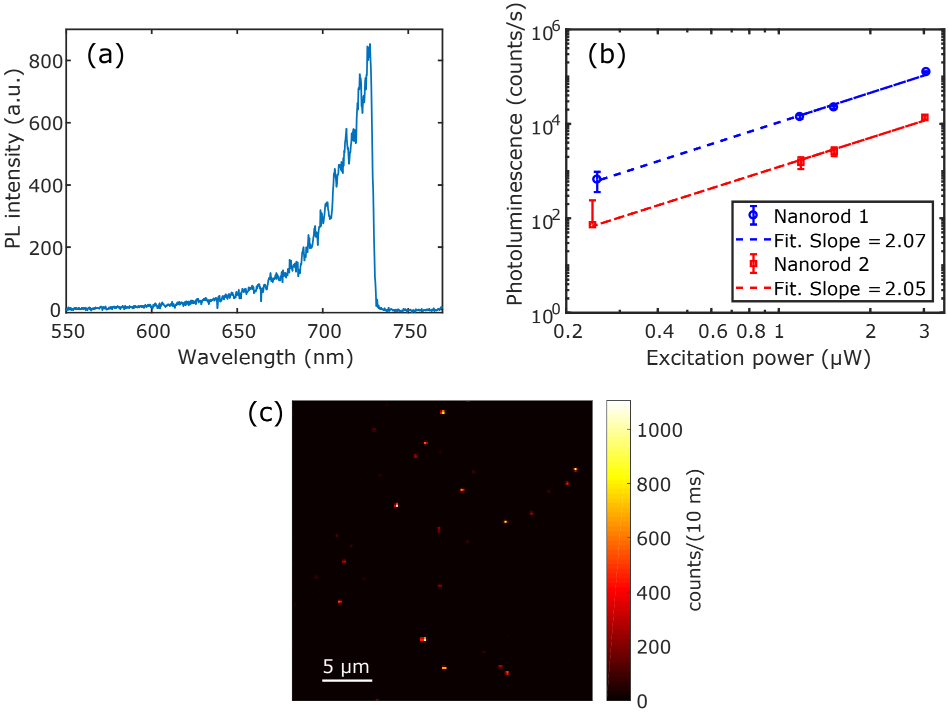

Figure S4.6: **Two-photon-excited luminescence of gold nanorods**. (a) Typical two-photon-excited luminescence spectrum of a gold nanorod immersed in water. The immobilized nanorod was excited with the femtosecond laser (circularly polarized) with an average power of 3 μW. (b) Log-log plot of the dependence of the photoluminescence intensity on the excitation power for two gold nanorods. The fitted slopes reveal a quadratic intensity-excitation relation, confirming the two-photon excitation origin of photoluminescence from the nanorods. The nanorods were immersed in methanol and excited with the femtosecond laser (circularly polarized). (c) An image of two-photon-excited luminescence of gold nanorods immobilized on a glass coverslip and immersed in methanol. The image size is 30 μm × 30 μm. Each pixel is 0.2 μm × 0.2 μm with an integration time of 10 ms/pixel. The excitation source was the femtosecond laser (circularly polarized) with an average power of 3 μW. For (a-c), a 745-nm shortpass filter and a 785-nm notch filter were used to block the excitation wavelength.

References

[1] M. Orrit and J. Bernard, *Single pentacene molecules detected by fluorescence excitation in a p-terphenyl crystal,* Physical Review Letters **65**, 2716 (1990).

[2] B. Schuler and W. A. Eaton, *Protein folding studied by single-molecule FRET,* Current Opinion in Structural Biology **18**, 16 (2008).

[3] S. Weiss, *Fluorescence spectroscopy of single biomolecules,* Science **283**, 1676 (1999).

[4] X. S. Xie and H. P. Lu, *Single-molecule enzymology,* Journal of Biological Chemistry **274**, 15967 (1999).

[5] X. Zhu, Q. Su, W. Feng, and F. Li, *Anti-Stokes shift luminescent materials for bio-applications,* Chemical Society Reviews **46**, 1025 (2017).

[6] J. L. Clark, P. F. Miller, and G. Rumbles, *Red edge photophysics of ethanolic rhodamine 101 and the observation of laser cooling in the condensed phase,* The Journal of Physical Chemistry A **102**, 4428 (1998).

[7] W. Qin, S. Huang, G. Du, J. Zhang, G. De, J. Zhang, Y. Wang, C. Cao, and S. Lu, *Anti-Stokes fluorescent cooling by energy transfer,* Journal of Luminescence **119**, 356 (2006).

[8] Y. Liu, Q. Su, X. Zou, M. Chen, W. Feng, Y. Shi, and F. Li, *Near-infrared in vivo bioimaging using a molecular upconversion probe,* Chemical Communications **52**, 7466 (2016).

[9] P. Anger, P. Bharadwaj, and L. Novotny, *Enhancement and quenching of single-molecule fluorescence,* Physical Review Letters **96**, 113002 (2006).

[10] A. Kinkhabwala, Z. Yu, S. Fan, Y. Avlasevich, K. Müllen, and W. Moerner, *Large single-molecule fluorescence enhancements produced by a bowtie nanoantenna,* Nature Photonics **3**, 654 (2009).

[11] H. Yuan, S. Khatua, P. Zijlstra, M. Yorulmaz, and M. Orrit, *Thousand-fold enhancement of single-molecule fluorescence near a single gold nanorod,* Angewandte Chemie International Edition **52**, 1217 (2013).

[12] Y. Fu, J. Zhang, and J. R. Lakowicz, *Plasmon-enhanced fluorescence from single fluorophores end-linked to gold nanorods,* Journal of the American Chemical Society **132**, 5540 (2010).

[13] S. A. Maier, *Plasmonics: fundamentals and applications* (Springer Science & Business Media, 2007).

[14] F. Tam, G. P. Goodrich, B. R. Johnson, and N. J. Halas, *Plasmonic enhancement of molecular fluorescence,* Nano Letters **7**, 496 (2007).

[15] S. Sreejith, P. Carol, P. Chithra, and A. Ajayaghosh, *Squaraine dyes: a mine of molecular materials,* Journal of Materials Chemistry **18**, 264 (2008).

[16] K. Podgorski, E. Terpetschnig, O. P. Klochko, O. M. Obukhova, and K. Haas, *Ultra-bright and stable red and near-infrared squaraine fluorophores for in vivo two-photon imaging,* PloS one **7**, e51980 (2012).

[17] E. G. Matveeva, E. A. Terpetschnig, M. Stevens, L. Patsenker, O. S. Kolosova, Z. Gryczynski, and I. Gryczynski, *Near-infrared squaraine dyes for fluorescence enhanced surface assay,* Dyes and Pigments **80**, 41 (2009).

[18] E. Arunkumar, N. Fu, and B. D. Smith, *Squaraine-derived rotaxanes: Highly stable, fluorescent near-IR dyes,* Chemistry-A European Journal **12**, 4684 (2006).

[19] W. Zhang, M. Caldarola, B. Pradhan, and M. Orrit, *Gold nanorod enhanced fluorescence enables single-molecule electrochemistry of methylene blue,* Angewandte Chemie International Edition **56**, 3566 (2017).

[20] M. Yorulmaz, S. Khatua, P. Zijlstra, A. Gaiduk, and M. Orrit, *Luminescence quantum yield of single gold nanorods,* Nano Letters **12**, 4385 (2012).

[21] A. Carattino, S. Khatua, and M. Orrit, *In situ tuning of gold nanorod plasmon through oxidative cyanide etching,* Physical Chemistry Chemical Physics **18**, 15619 (2016).

[22] B. Valeur and M. N. Berberan-Santos, *Molecular fluorescence: principles and applications* (John Wiley & Sons, 2012).

[23] S.-J. Chung, S. Zheng, T. Odani, L. Beverina, J. Fu, L. A. Padilha, A. Biesso, J. M. Hales, X. Zhan, K. Schmidt, A. Ye, E. Zojer, S. Barlow, D. J. Hagan, E. W. Van Stryland, Y. Yi, Z. Shuai, G. A. Pagani, J.-L. Brédas, J. W. Perry, and S. R. Marder, *Extended squaraine dyes with large two-photon absorption cross-sections,* Journal of the American Chemical Society **128**, 14444 (2006).

[24] S. Khatua, P. M. Paulo, H. Yuan, A. Gupta, P. Zijlstra, and M. Orrit, *Resonant plasmonic enhancement of single-molecule fluorescence by individual gold nanorods,* ACS Nano **8**, 4440 (2014).

[25] S. Khatua, H. Yuan, and M. Orrit, *Enhanced-fluorescence correlation spectroscopy at micro-molar dye concentration around a single gold nanorod,* Physical Chemistry Chemical Physics **17**, 21127 (2015).

[26] S. Rüttinger, V. Buschmann, B. Krämer, R. Erdmann, R. Macdonald, and F. Koberling, *Comparison and accuracy of methods to determine the confocal volume for quantitative fluorescence correlation spectroscopy,* Journal of Microscopy **232**, 343 (2008).

5

Plasmonic enhancement of two-photon-excited luminescence of single quantum dots by individual gold nanorods

Plasmonic enhancement of two-photon-excited fluorescence is not only of fundamental interest but also appealing for many bioimaging and photonic applications. The high peak intensity required for two-photon excitation may cause shape changes in plasmonic nanostructures, as well as transient plasmon broadening. Yet, in this work, we report on strong enhancement of the two-photon excited photoluminescence of single colloidal quantum dots close to isolated chemically synthesized gold nanorods. Upon resonant excitation of the localized surface plasmon resonance, a gold nanorod can enhance the photoluminescence of a single quantum dot more than $10,000$*-fold. This strong enhancement arises from the combined effect of local field amplification and the competition between radiative and nonradiative decay rate enhancements, as is confirmed by time-resolved fluorescence measurements and numerical simulations.*

5.1. Introduction

Due to their unique properties associated with surface plasmons, nanostructures based on metal nanoparticles have been extensively studied for their potential in various applications, such as surface-enhanced Raman spectroscopy [1, 2], metal-enhanced fluorescence [3–5] and second harmonic generation [6, 7]. Plasmonic nanostructures were found to significantly enhance the fluorescence emission of adjacent chromophores as a result of the interplay of several factors, including excitation enhancement because of the high local field, spontaneous radiative emission enhancement from resonant Purcell effect and fluorescence quenching due to nonradiative energy transfer to the metal [8, 9].

Apart from the extensive research on the enhancement of conventional one-photon-excited fluorescence [3, 10–13], the last two decades have seen a growing interest in metal-enhanced fluorescence under two-photon excitation, which is known for the advantages of intrinsic optical sectioning, deeper penetration into biological tissues and, under certain conditions, lower photo-damage. Upon two-photon excitation, a much larger fluorescence enhancement is expected because of the quadratic dependence of two-photon absorption on the excitation intensity. Starting from the 1990s, metal-enhanced two-photon-excited fluorescence has been experimentally demonstrated with lithographically made flat or patterned metal films [9, 14, 15]. There have been also reports on the enhancement of upconversion luminescence using plasmonic nanoparticles [16, 17].

Wet-chemically synthesized metal nanoparticles have been exploited as important alternative structures for plasmonic enhancement [8, 10, 18, 19]. Among many types of metallic nanoparticles, gold nanorods are the most extensively explored. Their intense electromagnetic fields associated with the narrow, strong and tunable plasmon resonance contribute to large enhancement of the fluorescence signal of nearby fluorescent emitters such as molecules and quantum dots. Compared to metal surfaces and nanoparticle clusters [20, 21], individual gold nanorods open the study of plasmon-choromophore interactions in a more reproducible and controllable way owing to their well-defined single-crystalline structure. Compared to nanogap antennas, such as bow-ties, dimers or particles on mirror, nanorods present a more open near field, which can accommodate molecules of various sizes. Moreover, gold nanorods are chemically inert and biocompatible, therefore they are particularly interesting for biotechnological applications.

A few recent reports have successfully demonstrated enhanced two-photon absorption and emission using various systems of nanocomposites composed of colloidal nanorods surrounded by fluorophores [9, 22–25]. However, the enhancement factors reported in ensembles are reduced by averaging over many fluorophores, most of which are not in the best position.

Combined single-molecule and single-particle measurements are needed to bridge the gap between theory and experiments. Moreover, single-molecule and single-particle measurements have the potential of revealing the intrinsic nature of the plasmon-emitter interactions that is usually hidden in ensemble experiments by nanoparticle inhomogeneities, such as size fluctuations and local environment variations.

While seemingly a straightforward idea, two-photon-excited fluorescence enhancement with a single-emitter-single-nanostructure system was investigated theoretically [26] and only achieved experimentally in a very recent work by Gong *et al.*, where the two-photon excited luminescence intensity from single epitaxially grown InGaN quantum dots (QDs) was enhanced by a factor of 5000 using the strong field enhancement by a silver-coated pyramid structure at a temperature of 7 K [27]. Indeed, two possible major obstacles stand in the way to experimentally testing the two-photon fluorescence enhancement. First, the high peak intensities required for efficient two-photon excitation might damage the plasmonic structure, if not after a single pulse, certainly upon repeated excitation by millions of pulses over long acquisition times. Photothermal reshaping of gold nanorods under femtosecond pulses [28–30] limits the laser intensity one can use for two-photon excitation. Second, the excitation by intense femtosecond pulses tremendously heats up the electron gas by up to thousands of K, thereby broadening the plasmon resonance [31] and potentially hindering plasmonic enhancement. Added to the difficulty of a precise positioning of a single emitter with respect to the near field of plasmonic structures, these two problems may hamper plasmonic enhancement of two-photon excitation.

Our earlier studies have shown that, by exploiting the random diffusion of single molecules around single gold nanorods, the fluorescence of a low-quantum-yield dye could transiently be enhanced by three orders of magnitude [8, 18]. Motivated by the theoretical limit to two-photon-excited fluorescence enhancement, we exploited diffusion and transient sticking of single colloidal QDs to study the strong enhancement of their two-photon-excited luminescence by single gold nanorods at room temperature. We find enhancement of two-photon-excited luminescence by more than four orders of magnitude for *single* QDs in the vicinity of a *single* immobilized gold nanorod at room temperature. The enhancement factor shows a clear dependence on the nanorod's surface plasmon resonance wavelength and is maximum when the resonance wavelength overlaps with the excitation laser wavelength. The achieved enhancement is in good agreement with the predictions of numerical calculations. The dependence on surface plasmon resonance (SPR) wavelength and the fair agreement with simulations show that the transient broadening of the plasmonic resonance by femtosecond excitation is not a limiting factor for two-photon-excited fluorescence enhancement by individual gold nanorods.

5.2. Materials and methods

Gold nanorods. Aqueous suspensions of cetyltrimethylammonium bromide (CTAB) stabilized gold nanorods were purchased from Nanopartz Inc. (A12-40-780-CTAB). The average size was 38 nm × 118 nm by diameter and length. Individual isolated gold nanorods were immobilized onto a glass coverslip by spin coating suspensions with reduced CTAB concentration [18]. After spin coating we removed the stabilization ligands from the surface of the gold nanorods by ozone treatment for 30 minutes. This results in bare gold nanorods (*i.e.* without any ligands on their surface), allowing easy access for the quantum dots.

Two-photon microscopy. We performed two-photon excited luminescescence measurements on a home-built sample-scanning fluorescence microscope system similar to Chapter 4. The glass coverslip with deposited gold nanorods was immersed in a dilute aqueous solution of QDs. A mode-locked titanium-sapphire laser (Coherent Mira 900) was used as the two-photon excitation source, operating at 775 nm, 76 MHz pulse repetition rate and ~ 220 fs pulse width. The excitation power was measured at the output of the objective. Circular polarization was used, as it excites all the GNRs irrespective of their random orientation in the focal plane. Time-resolved photoluminescence photons from QDs and gold nanorods were passed through a 650-nm bandpass filter (HQ650/50, Chroma) and recorded with an avalanche photodiode (APD) and processed with a time-correlated single photon counting (TCSPC) card (TimeHarp 200, PicoQuant GmbH). The bandpass filter was used to pass through the luminescence from QDs while reducing the background from two-photon photoluminescence of nanorods. A 532-nm continuous wave laser and a spectrometer equipped with a liquid-nitrogen-cooled CCD (Acton SP-500i, Princeton Instruments) were used to measure the one-photon-excited luminescence spectrum of each nanorod, which was shown previously [32] to closely resemble its scattering spectrum. Spectra of nanorods were measured in water without QDs prior to the enhancement measurements. The spectra were corrected for the spectral response of the optical setup and instruments. Only single nanorods evidenced by their narrow Lorentzian spectral lineshapes were considered in this study. See Chapter 4 for a more detailed description of the optical setup and spectral correction.

5.3. Results and discussion

The colloidal QDs in our study (Qdot 655 ITK amino (PEG) from Invitrogen) are CdSe/ZnS core-shell structures, which are further coated with an amphiphilic polymer shell to enable conjugation of amine-derivatized polyethylene glycol. Their overall shape is rod-like and the length and width are $\sim$ 12 nm and $\sim$ 7 nm, respectively [33]. See Supporting Information for more details about the QDs structure. The narrow emission band centered at 655 nm is well away from the longitudinal plasmon resonance of the gold nanorods as can be appreciated in Fig. 5.1. This feature results in a good contrast of signal from single quantum dots against a background from the intrinsic luminescence of the gold nanorods if an appropriate bandpass filter is used. Two-photon photoluminescence was excited by a mode-locked titanium-sapphire laser operating at 76 MHz pulse repetition rate and $\sim$ 220 fs pulse width. The wavelength was set to 775 nm to efficiently excite the longitudinal plasmon resonance of the gold nanorods.

To determine whether the photoluminescence of QDs generated by the femtosecond laser is a result of instantaneous two-photon absorption, we measured the photoluminescence emission intensity from a diluted aqueous suspension of Qdot 655 with respect to the average intensity at the center of the focused excitation beam. Figure 5.1(b) plots this relation in log-log scale, yielding a slope of 2.11 ± 0.03, which confirms the two-photon excitation origin of the observed luminescence from the QDs.

Prior to the luminescence enhancement experiments, we measured the one-photon-excited photoluminescence spectra of gold nanorods immobilized on a coverslip and immersed in water. We selected single gold nanorods through their narrow and Lorentzian spectral shape for our later measurements. Afterwards, the nanorods were immersed in a 30 nM Qdot 655 solution with 3 mM NaCl (inset of Fig. 5.1(a)). Photoluminescence photons were recorded on individual gold nanorods under the excitation of the femtosecond laser with an average excitation intensity of 1.55 kW/cm^2 (1 μW at the objective focus) at the center of the focused excitation volume. We note that this intensity is well below that required for photothermal reshaping of single gold nanorod with a low number ($\sim$ 1 to 10^4) of ultrafast pulses [28–30]. Indeed, we did not observe any luminescence intensity change from the gold nanorods upon femtosecond irradiation, even after our extended measurements of several minutes. More-

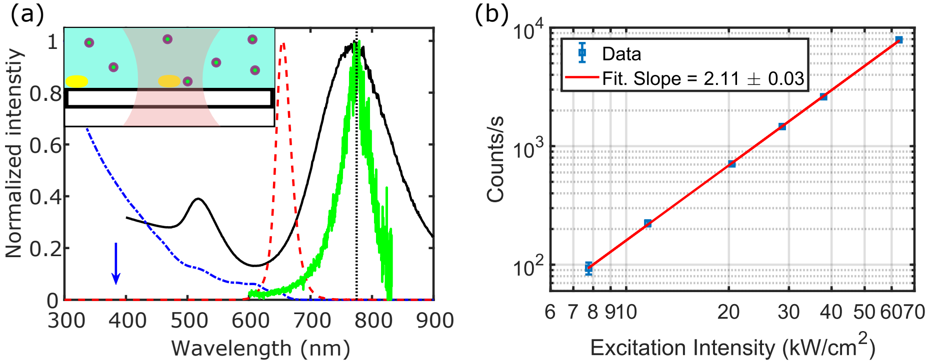

Figure 5.1: **Quantum dots and gold nanorods optical characterization**. (a) Spectra of gold nanorods and quantum dots. The black and green solid lines show the bulk extinction spectrum of gold nanorods dispersed in water and the one-photon-excited photoluminescence spectrum of an immobilized single gold nanorod, respectively. One-photon absorption and emission spectra of the quantum dots diluted in water are shown as the blue dot-dashed line and red dashed lines, respectively. The vertical dotted line shows the wavelength of the Ti:Sapphire laser. The blue vertical arrow indicates the wavelength corresponding to the total energy of two excitation photons. The inset shows a simplified schematics of the enhancement experiment (the yellow cylinders represent gold nanorods; core/shell circles, quantum dots). (b) Log-log plot showing the quadratic dependence of photoluminescence emission of the quantum dots on the excitation intensity. The photoluminescence emission is from a 30 nM quantum dot solution with 1 mM NaCl.

over, the measured one-photon-excited photoluminescence spectra of gold nanorods before and after femtosecond irradiation showed no noticeable changes. Therefore, the nanorods were not reshaped during our measurements. It is worth mentioning that most previous studies on ultrafast reshaping of gold nanoparticles were done with single or a few pulses. Under continuous irradiation of pulses, however, accumulative heating leads to a much lower reshaping threshold in terms of average power. Indeed, we started to observe reshaping for some nanorods with an excitation power $\geq 3\,\mu$W (intensity of 4.7 kW/cm^2 with circular polarization).

Figure 5.2 shows two typical intensity traces (binned to 100 ms) from two gold nanorods whose spectra are shown in the right panels. The spectra have been corrected for the spectral response of the optical setup (see Fig. S2.2 in Chapter 2). Intensity bursts are observed for both nanorods, which we attribute to gold nanorod-enhanced photoluminescence emission of single QDs. Some weak background signal comes mostly from the two-photon-excited luminescence of the gold nanorods [34] (see Fig. S4.6 in Chapter 4). Note that the bursts shown in Fig. 5.2 last generally a few tens of milliseconds to a few seconds.

We used two-photon-excited fluorescence correlation spectroscopy with a two-fold purpose. First, to obtain the diffusion time of our QDs in the confocal volume and second, to measure the single-QD brightness, needed to quantify the enhancement factor.

The diffusion time of a single QD in the near field of a rod is shorter than one microsecond, estimated from the diffusion time in the confocal volume, measured by autocorrelating the two-photon-excited luminescence of freely difussing QDs (Fig. S5.1). Thus we attribute the bursts to transient sticking of QDs onto the substrate and/or the gold nanorods (note that the emitting part of a QD is separated from the gold surface by the polymer coating, therefore

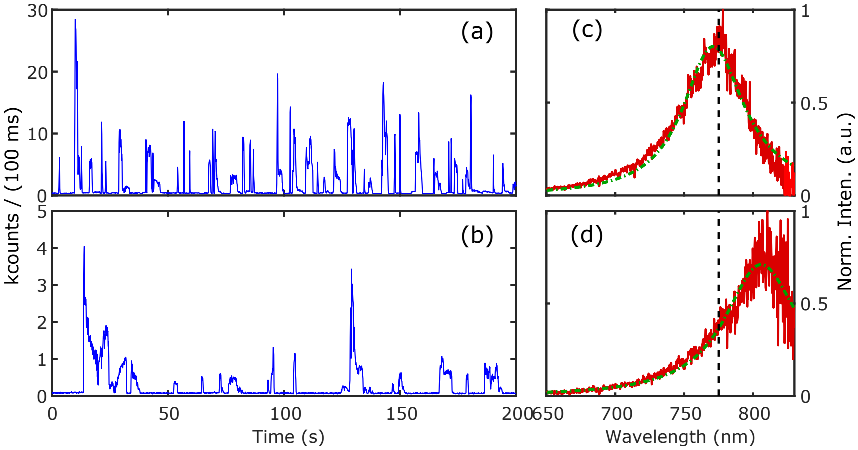

Figure 5.2: **Enhanced two-photon excited luminescence from single QDs.** (a,b) Two-photon-excited luminescence intensity timetraces (100 ms/bin) taken on two single nanorods immersed in 30 nM QD aqueous solution with 3 mM NaCl and (c,d) the corresponding one-photon-excited luminescence spectra of the nanorods measured in water. The excitation intensity at the center of two-photon excitation volume was 1.55 kW/cm^2 (circularly polarized). The one-photon-excited spectra show narrow Lorentzian lineshape (green dashed lines), confirming that they are from single nanorods. The low near-infrared response of the optics including the spectrometer CCD is responsible for the high noise. The wavelength of the laser (775 nm) is also shown as the dashed vertical lines in (c) and (d).

sticking to a gold nanorod does not necessarily completely quench its photoluminescence). This nonspecific sticking effect was found in a few studies to be strongly dependent on the properties of the diffuser and the surrounding medium as well as the surface conditions of the metal and substrate [18, 35, 36]. In our case, the addition of a proper amount of NaCl to the QD solution was essential for transient sticking and, hence, for observing luminescence bursts. If no NaCl was added we saw only luminescence from gold nanorods . On the other hand, when the NaCl concentration was too high, the bursts were too long to be separated from each other (data shown in Supporting Information Fig. S5.5).

From the correlation measurements explained in detail in the Supporting Information, we obtained an average unenhanced single-QD brightness of 1900 ± 70 counts/s at 15.5 kW/cm^2 illumination intensity. We note here that this is an ensemble-averaged result that may show significant fluctuations when compared to single-QD data due to variations from dot to dot, for example in size. We also note that the intensity used for this unenhanced measurement is × 10 higher than the intensity used for the enhancement experiment on a nanorod.

We attribute the large difference in burst intensities recorded on the same gold nanorod to the random locations and orientations of the QDs with respect to the gold nanorod. Additionally, the size distribution of the QDs in our sample contributes further to the intensity inhomogeneity of the enhancement bursts. We observed that the more intense the bursts are, the shorter they last, as it can be seen in Fig. 5.2. Indeed we confirmed this behavior by plotting the burst duration as a function of the burst detected intensity for an enhanced time trace (see Fig. S5.2). In addition, we note that we did not observe characteristic luminescence blinking of QDs [37, 38]. However, blinking may occur either on a time scale shorter than our resolution or at times longer than the burst duration. We note that earlier observations indicate that QD blinking is greatly suppressed when coupled to plasmonic structures [39, 40].

Blank experiments were performed to verify that the bursts are from gold nanorod-enhanced single QDs. We recorded timetraces on a area without a nanorod under the same experimental conditions. We also measured single nanorods with the same excitation but immersed in 3 mM NaCl without QDs. In both cases, we never observed any burst, as shown in the example traces in the Suppporting Information (Fig. S5.3). Moreover, we recorded timetraces on *the same* single gold nanorod in solutions with different concentrations of QD (6 nM and 30 nM) and we found higher occurrence of bursts in the solution with higher QD concentration (Fig. S5.4). It clearly demonstrates the linear dependence of burst frequency on QD concentration.

The previous experiments convinced us that the bursts stem from enhanced two-photon-excited luminescence of single QDs. The size of the QDs is as large as the near-field, so it is unlikely that more than one QD reside in the near field. We have to consider the possibility of aggregates of QDs, as we did find evidence of them (Fig. S5.1) with an occurrence of 20 per 300 s in the confocal volume. However, considering a near-field volume that is ~ 2000 times smaller than the confocal volume ($V_{\text{conf}} = 3 \times 10^{-2}$ fL, $V_{\text{NF}} = 1.4 \times 10^{-5}$ fL), the probability of seeing one QD aggregate in the near-field in a measuring time of 300 s is only 1%.

In order to calculate the luminescence enhancement factor, we need to compare the two-photon-excited enhanced intensity with the unenhanced brightness of a single quantum dot (i.e. count rate per dot). The former can be extracted from the time traces in Fig. 5.2 and the latter was obtained using two-photon fluorescence correlation spectroscopy (FCS) [41]. The same QD solution used for the enhancement experiment was excited with an average excitation intensity of 15.5 kW/cm^2 (below saturation). By scaling with the quadratic power dependence of two-photon-excited luminescence, we found the count rate per dot to be 19.0 ± 0.1 counts/s at an excitation intensity of 1.55 kW/cm^2. See the Supporting Information (Fig. S5.1) for details. The maximum intensity of the burst shown in Fig. 5.2(a) is 2.84×10^2 kcounts/s for circularly polarized excitation. It is from a single QD enhanced by the nanorod against a background signal of 2850 counts/s from the nanorod and other QDs in the focal volume. Based on a brightness of 19.0 counts/s per QD measured with FCS at the same excitation intensity, we calculate an enhancement factor of 1.5×10^4 for circularly polarized light. We used circularly polarized light to excite all the nanorods in the glass surface, regardless of their orientation. If we would use linearly polarized light parallel to the long axis of the nanorod, we expect to observe a larger enhancement of 6×10^4.

We would like to emphasize that the reported enhancement factor comes from looking at the highest burst in a time trace, as is commonly done in the literature. However, there are other alternative methods to obtain the enhancement factor from the same type of experimental data, leading to similar results [42].

Comparison of Fig. 5.2(a) and (b) clearly reveals that the enhancement strongly depends on the longitudinal plasmon resonance wavelength of the gold nanorod. The plasmon resonance of the nanorod shown in the upper panels matches the laser wavelength very well, giving rise to almost one order of magnitude more intense bursts than the other nanorod, whose resonance wavelength is $\sim$ 30 nm away from the laser wavelength. We repeated the measurements on 23 different individual nanorods and plotted their maximum luminescence enhancement factors in Fig. 5.3(a). The strongest enhancement was achieved by a nanorod with a surface plasmon resonance wavelength of 771 nm. The time trace and spectrum of this nanorod are those shown in Fig. 5.2(a). We note that our observation of two-photon excited enhanced emission gives evidence that the transient plasmon broadening is not serious limitation to the two-photon enhancement.

To understand the measured luminescence enhancement theoretically, we employed a finite-element method (Comsol Multiphysics) and a boundary element method to model the quantum dot-nanorod system. The photoluminescence emission of an emitter in the vicinity of a gold nanorod is altered through the modification of both the excitation and emission rates, as illustrated by Khatua *et al.* considering a two-level model [8]. For excitation intensities below saturation, we can treat absorption and emission independently. This assumption is justified because the saturation intensity is $\sim$ 2000 times higher than the incident laser intensity in our enhancement experiments (Fig. S5.7). Such a high saturation intensity is well above the local field intensity that can be attained by the nanorods used in our study, about 300 times larger than the incident intensity. Therefore, the overall enhancement factor is approximated by the product of excitation enhancement and emission enhancement [8]. See the Supporting Information for the details of the simulations.

In Fig. 5.3(a), along with measured photoluminescence enhancement factors, we plot the calculated overall enhancement factors for point emitters that are 5 nm away from the tip of the nanorod as a function of the plasmon resonance wavelength of the nanorod, while the near-field intensity map of the nanorod with the highest enhancement is shown in Fig. 5.3(b). From this map, it is straightforward to obtain the excitation enhancement as $E_{ex} = (I/I_0)^2$, which is shown in panel (d), left axis as a function of the distance to the tip.

In Fig. 5.3(c) we plot the calculated radiative rate enhancement ($k_\mathrm{r}/k_\mathrm{r}^0$, blue triangles) and relative additional nonradiative rate ($K_\mathrm{nr}/k_\mathrm{r}^0$, red circles) of a QD against the distance to the tip of a single nanorod. The size of the nanorod in the calculation was 38 nm $\times$114 nm with a plasmon resonance of 775 nm in water. The high additional nonradiative rate due to the strong absorption of the gold nanorod (quenching) leads to an emission “enhancement” factor that is lower than unity.

The emission enhancement is proportional to the inverse of the emitter’s intrinsic quantum yield (see Supporting Information), which is not a priori known in our experiments. First, the quantum yield of individual QDs varies due to the size distribution [33]. Second, it is known that the quantum yield of a single QD fluctuates with time in a manner that is strongly correlated with the luminescence lifetime [43–46]. Moreover, the presence of on-off blinking and intermediate states [44] adds further complications to the "on-state" quantum yield of a QD.

In addition to these unknown parameters of the system, we modeled the measured lifetime decay with three exponential components (see supporting information Fig. S5.6 for details) for unenhanced QDs in solution. The obtained lifetimes are $\tau_1 = 1.5$ ns, $\tau_2 = 16.5$ ns and $\tau_3 = 46.2$ ns. In the absence of detailed information on the QD emission we used two simple models to calculate the emission enhancement. Model 1 assumes that the three components have the same radiative rate k^0_rad. We then use the measured lifetimes to obtain

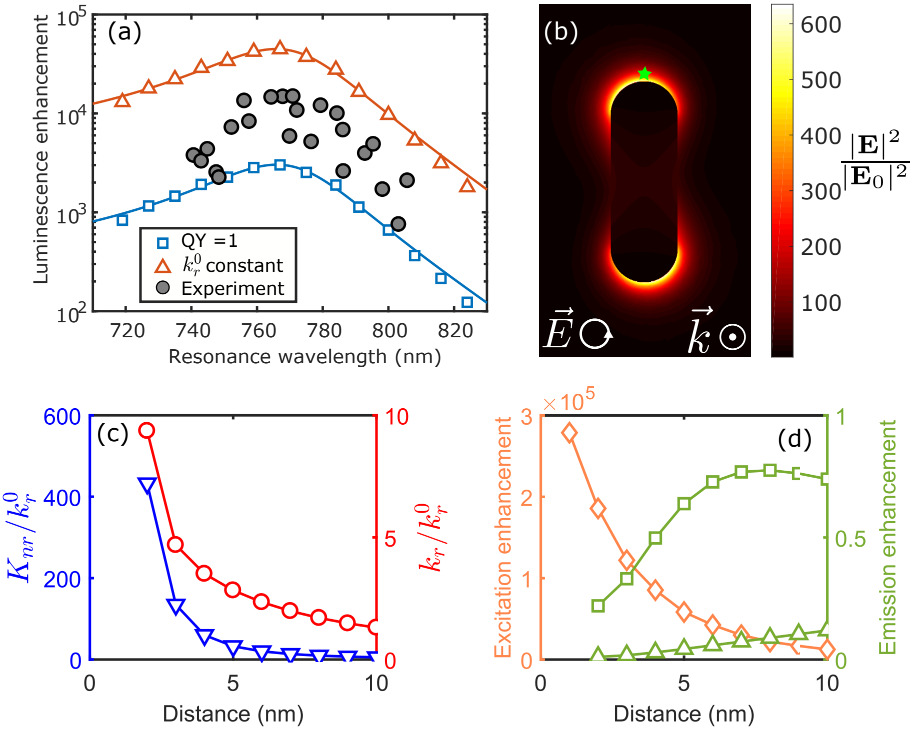

Figure 5.3: **Enhancement dependence with plasmon resonance.**(a) Measured maximum two-photon excited luminescence enhancement factors for 23 gold nanorods plotted against their plasmon resonance wavelengths are shown as gray circles. The numerically calculated overall enhancement factors for two different models of QD luminescence (see main text) in red triangles and blue squares. Solid lines are guides to the eye. For the calculations, the emitter is assumed to be located 5 nm away from the tip of the nanorod (green star in (b)). (b) Calculated near-field intensity map of a 38 nm ×114 nm nanorod in water, with SPR at 775 nm. (c) Calculated radiative rate enhancement ($k_\mathrm{r}/k_\mathrm{r}^0$, red circles, right axis) and relative additional nonradiative rate ($K_\mathrm{nr}/k_\mathrm{r}^0$, blue triangles, left axis) of a QD as a function of the distance to the tip of the nanorod. (d) Calculated excitation enhancement (orange diamonds) and emission enhancement (green squares and triangles) as functions of the distance to the tip of the nanorod. The squares and triangles correspond to the two models mentioned above for (a). The excitation wavelength was 775 nm (circularly polarized) for both experiments and simulations.

the quantum yield for each component. We additionally assumed a unity quantum yield for the longest component. Model 2 assumes unity quantum yield for all three components. In both cases we calculated the emission enhancement for each component individually and then averaged the results with the weights obtained from the lifetime fit shown in the supplementary material. The results for the two models are plotted in Fig. 5.3(a) as a function of the SPR (model 1 as red triangles and model 2 as blue squares) and Fig. 5.3(d) as a function of the gold nanorod-QD distance (model 1 as triangles and model 2 as squares). From Fig. 5.3(a) we see that these two extreme models reproduce the resonance wavelength dependence quite well. The experimental points lay between the two curves, showing that these simple models do not give a complete quantitative description of the system. Figure 5.3(d) shows the calculated two-photon excitation enhancement and emission enhancement as functions of the distance to the tip of the nanorod. Overall, our experimental results agree well with theoretical calculations both for the enhancement factors and the dependence on the resonance wavelength. Therefore, comparison to theory indicates that transient plasmon broadening, if at all present, does not significantly reduce the two-photon-excited fluorescence enhancement.

It is also of interest to investigate the impact of gold nanorods on the photoluminescence lifetime of QDs. The intrinsic two-photon-excited photoluminescence lifetime of the QDs could not be accurately measured with our current system due to the high repetition rate of the titanium-sapphire laser. We noticed that it was reported that the photoluminescence lifetimes of CdSe quantum dots under one- and two-photon excitations are nearly identical [47]. Therefore, we measured the complete photoluminescece decay of the same QD solution with one-photon excitation by using a pulsed picosecond diode laser (Power Technology, Little Rock) with a repetition rate of 1 MHz and a wavelength of 635 nm, and we obtained a non-exponential decay with an average lifetime of 6.3 ns (See Supporting Information for more explanation and Fig. S5.6 for the curve). In the presence of nanorods, we obtained the lifetimes of the enhanced two-photon-excited luminescence from the recorded time-tagged single-photon data. The instrument response function (IRF) was measured by recording luminescence photons from a nanorod in the same spectral range as the QDs [34]. For each time bin of 100 ms, we recorded a luminescence decay histogram and, after deconvoluting the instrument response function, fitted it with a single-exponential function, and plotted the temporal evolution of the lifetimes (i.e. a lifetime trace) in Fig. 5.4(b). The corresponding photoluminescence intensity trace from the same nanorod is plotted as well in Fig. 5.4(a) for comparison. We observed a shortened lifetime smaller than 2 ns due to the presence of the nanorod.

We also calculated numerically the photoluminescene lifetime for a QD near the gold nanorod for the three components using the simple model mentioned before. Figure 5.4(c)-(d) show the expected lifetime for each component and the weighted average result for the two models presented before. In both cases, the weighted average lifetime for a QD in the vicinity of the gold nanorods is below 5 ns, in agreement with the observed shortened lifetime. This strong shortening of lifetime is a combination of an enhanced radiative decay rate (k_r) and the additional non-radiative decay pathways due to the dissipation of gold (k_nr). The relation between luminescence intensity and lifetime is complicated due to the interplay between electromagnetic intensity enhancement and changes of radiative and nonradiative decay rates.

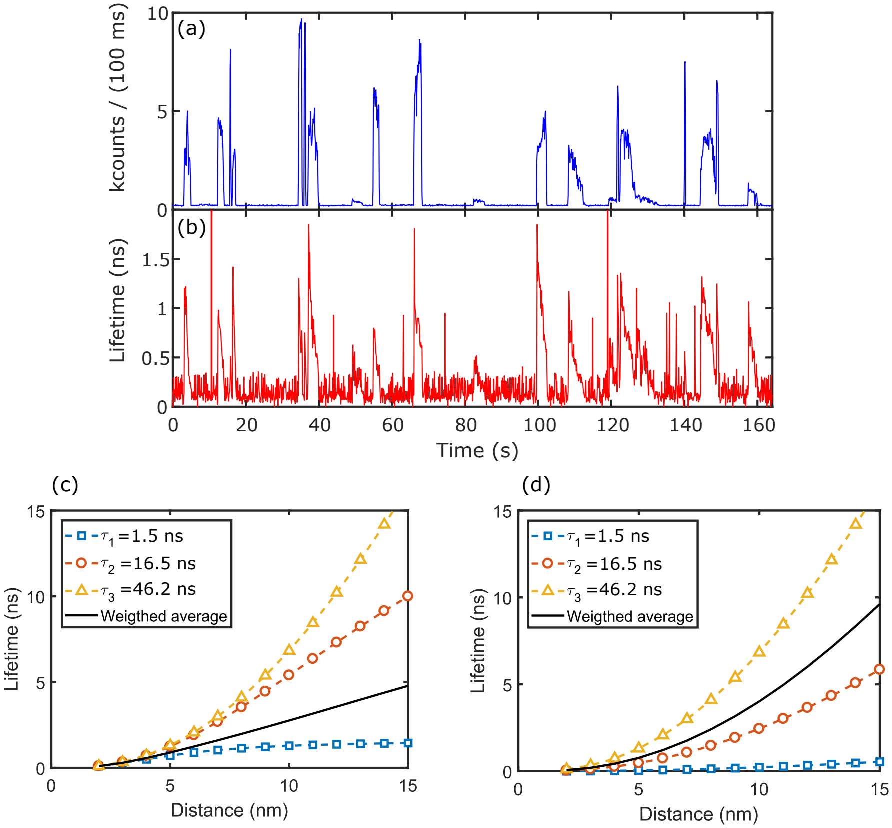

Figure 5.4: **QDs enhanced photoluminescence lifetime.** (a) Photoluminescence intensity trace and the corresponding lifetime trace (b) measured on a single gold nanorod. (c), (d) Calculated lifetime of a QD as a function of the distance to the tip of the nanorod, with different lifetimes indicated in the legend. For the calculation, the size of the single nanorod is 38 nm ×114 nm with a plasmon resonance of 775 nm in water, corresponding to the maximum enhancement. For (c) we assumed a constant radiative rate for all the species with a unity quantum yield for the longest component (τ_3). For (d) we assumed unit quantum yield for all the species.

Interestingly, we systematically found many photoluminescence bursts which show nearly constant or even increasing intensities but shorter lifetimes. We speculate that this interesting behavior may be a result of some photochemistry that is happening to the QDs in the vicinity of the nanorods. Oxidation of the QDs is unlikely the cause, as we observed the same phenomenon after removing oxygen by saturating the sample solution with Argon gas (data not shown). With the current set of data and experimental design, we are not able to identify the underlying mechanism. Obviously, the emission intensity and decay rates are strongly dependent on the QD location with respect to the nanorod, which is not a priori known in our case. Further investigations, preferably single-emitter and single-particle studies with well-defined structures and positions, are required to clarify this point.

5.4. Conclusions

In summary, this work demonstrates the enhancement of two-photon-excited luminescence from single emitters by wet-chemically synthesized single gold nanorods. Quantum dots with high two-photon brightness are used to detect enough luminescence signal while maintaining the shape of gold nanorods by using very low excitation intensity. An enhancement factor of $15,000$ ($60,000$ with linearly polarized light parallel to the long direction of the nanorod) is achieved by matching the plasmon resonance of gold nanorod with the excitation wavelength. This large enhancement results from the plasmon resonance-enhanced strong near-field at the tips of the gold nanorods and the quadratic dependence of two-photon absorption and the excitation intensity. We also observed a significant change in the quantum dot's luminescence lifetime due to interaction with the nanorods.

The good agreement between our experimental and simulation results suggest that luminescence enhancement is not notably affected by the plasmon broadening due to the presence of high electronic temperatures. We believe this study sheds some light on metal-enhanced fluorescence and paves the way for future studies of single-molecule-single-particle plasmonic enhancement of two-photon-excited luminescence. The luminescence enhancement by gold nanorods will be valuable for two-photon fluorescence applications [9, 23], especially when a low excitation power is required by experimental conditions.

5.5. Supporting information

5.5.1. Two-photon fluorescence correlation spectroscopy

To measure the average brightness of individual QDs without enhancement, we excite a solution of 30 nM QDs with 3 mM NaCl with fs laser (average 15.5 kW/cm^2, circularly polarized). About 20 high bursts in 300 seconds can be observed (Fig. S5.1(a)), which cannot be explained by the intensity fluctuations due to single quantum dots diffusing in and out of the focal volume. They are probably a consequence of a small amount of large clusters of QDs present in the solution. The longer time component (~ 30 ms) in the autocorrelation curve for the entire timetrace (back triangles in Fig. S5.1(b)) is probably from the clusters, which diffuse slower than single QDs. We tried several separating and filtering methods to get rid of the clusters, but it appeared that these clusters always reform in the aqueous solution. By autocorrelating photons within a period of time without high bursts (marked

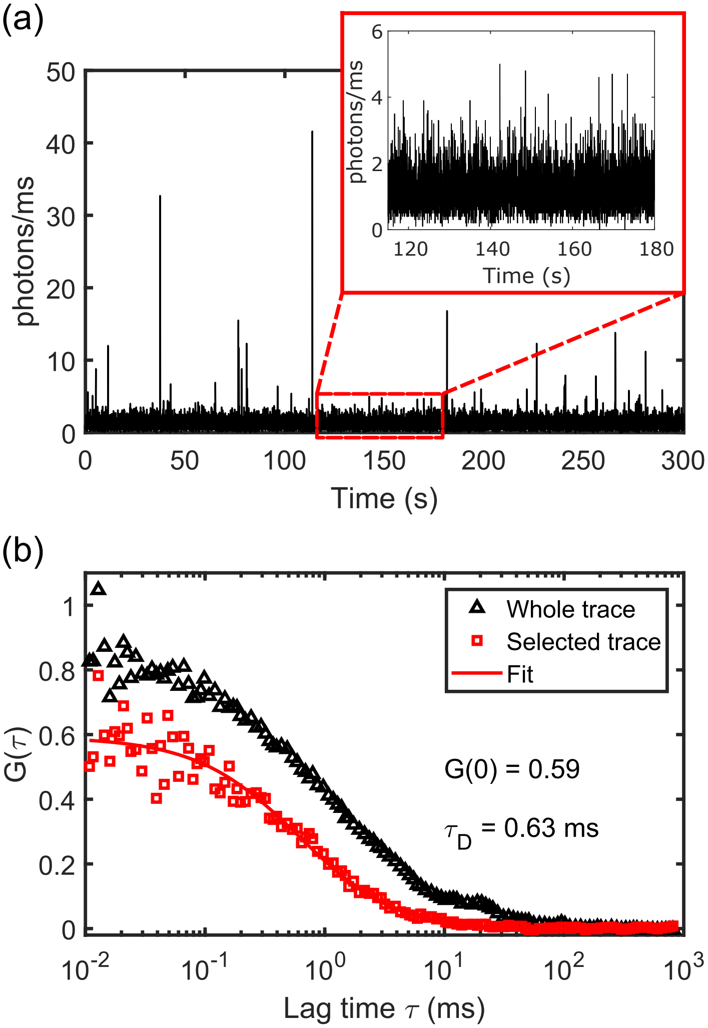

Figure S5.1: (a) Emission intensity time trace (binned to 10 ms) recorded from a solution of 30 nM QDs ($\lambda_{\mathrm{em}} = 655$ nm) with 3 mM NaCl without gold nanorods. The high bursts evidence the presence of aggregates of QDs in the solution. The average excitation intensity was 15.5 kW/cm^2. The inset shows a zoom in of the zone marked with the rectangle. This evidences the presence of single-QD bursts. (b) The black triangles plot the autocorrelation curve of the whole timetrace shown in (a). The stretched longer component at $\sim$ 30 ms comes from the strong bursts in (a). The red squares show the autocorrelation for the photons within the marked window in (a). No strong bursts were present in this period of timetrace. The autocorrelation curve can be fitted with a translational diffusion model, yielding an amplitude of 0.59 ± 0.02 and a diffusion time τ_D of (0.63 ± 0.07) ms.

by a red box in Fig. S5.1(a)), we got the autocorrelation curve for single quantum dots, which is shown as red triangles in Fig. S5.1(b). The autocorrelation curve was fitted with the following diffusion model [48, 49]

$$G(\tau) = G(0)\frac{1}{1+\tau/\tau_D}\frac{1}{\left[1+(w_0/z_0)^2\tau/\tau_D\right]^2},$$

where w_0 and z_0 are the $1/e^2$ width along the radial and axial direction of the excitation volume, respectively and τ_D is the diffusion time. For the fitting we used the values $w_0 = (202 \pm 2)$ nm and $z_0 = 560 \pm 5$ nm ($V_{\text{conf}} = 3 \times 10^{-2}$ fL). The fitting result is shown as a solid red line in Fig. S5.1(b). The number of QDs contributing to the average photoluminescence signal (1130.7 ± 28.2 counts/s) is related to the fitted amplitude of the autocorrelation function ($G(0)$) through $N = \gamma/G(0)$, where γ is geometrical factor that accounts for the shape of the excitation profile. For an overfilled objective lens, the excitation profile is a 3D-Gaussian and $\gamma = 2^{-3/2}$, therefore we obtained $N = 0.60 \pm 0.02$, which means a two-photon-excited confocal volume of (0.03 ± 0.01) fL. Then the brightness of each QD was calculated to be 1895 ± 72 counts/s at 15.5 kW/cm^2.

By considering the quadratic emission-intensity relation of two-photon photoluminescence, we found that the average brightness of each QD at the intensity used for the enhancement experiments (1.55 kW/cm^2 at the center of the excitation volume) should be 19.0 ± 0.7 counts/s. The excitation intensity was well below saturation. We found no evidence of blinking on microsecond to millisecond time scales, which is in agreement with previous observations [50, 51]. The study by Yao *et al.* suggests that QDs are still blinking in solution but longer dwell times are needed to detect the blinking [41].

5.5.2. Burst analysis: correlation between duration and intensity

We analyzed the two-photon excited enhanced time trace shown in Fig S5.2(a) to extract the burst duration and the intensity of each enhancement event and plotted the burst duration as a function of the intensity observed during the burst. Figure S5.2(b) shows the correlation plot between these two quantities in linear scale and (c) in log-log scale. We see that the high-intensity bursts have a short duration and that bursts with low intensity usually last longer.

5.5.3. Blank experiments

We performed some blank experiments to corroborate that the luminescence signal observed was indeed coming from the QDs and not from some other chemical species in the solution. First, we measure under the same experimental conditions used for the enhanced experiment in a position far away from any nanorod. The obtained time trace in this case is shown in Fig. S5.3(a). No bursts are observed. Note that the quantum dots are diffusing during the experiment and that at this extremely low power the two-photon excitation does not provide much signal.

Second, we measured in the same experimental conditions used for the enhancement but in a solution without any QDs on top of a nanorod. The measured time trace for this case is shown in Fig. S5.3(b) with an inset showing the scheme of the experiment. Again, there are

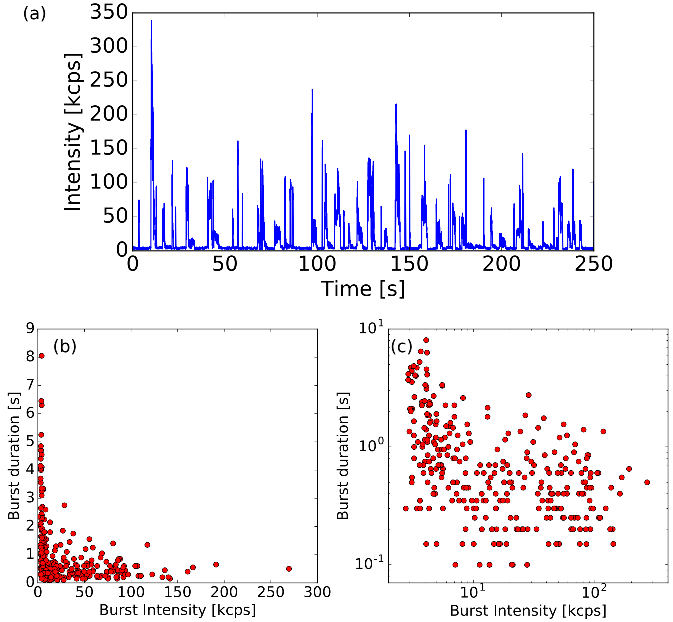

Figure S5.2: (a) Two-photon-excited photoluminescence enhanced time trace of Qdot 655. (b) Linear scale plot of the burst duration as a function of the burst intensity. (c) Same plot as (b) in log-log scale.

not bursts, as expected, but there is a significant contribution that we assign to two-photon excited photoluminescence of the gold nanorods. This is a quite efficient process since the laser is hitting the surface plasmon resonance of the particle and thus the absorption cross section is remarkably high.

5.5.4. Quantum dot concentration dependence

We also studied the concentration dependence of the enhanced signal from single QDs. We observed an approximate 5 times increase in the number of events registered in 275 s when we increase the concentration by a factor of 5 (see Fig. S5.4).

5.5.5. Enhancement time traces at different NaCl concentration

We took traces at different concentration of NaCl to empirically obtain the optimum concentration for our study. We seek a situation where we have clearly distinguished enhancement events, sparse enough in time to address them individually. Figure S5.5 shows two time traces, the top one at 1 mM and the bottom one at 5 mM concentration of NaCl. We see that when the concentration is too high, the enhancement events overlap in time, complicating the analysis.

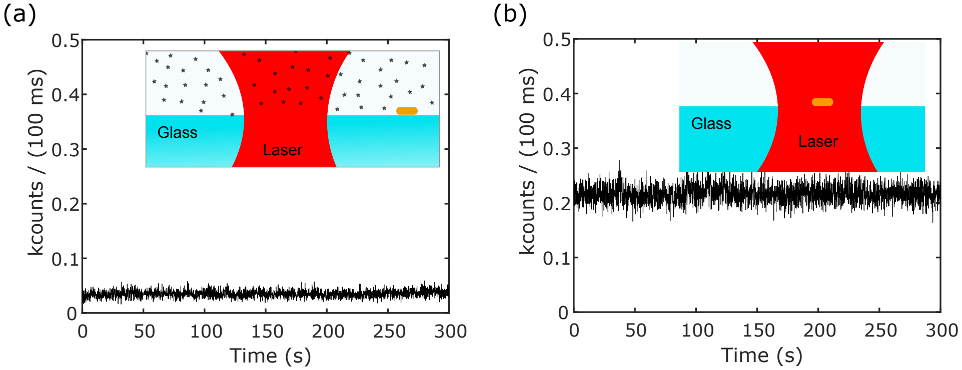

Figure S5.3: (a) A timetrace recorded on a solution of 30 nM QD and 3 mM NaCl in water, with no gold nanorod present. (b) A timetrace taken on a single gold nanorod in 3 mM NaCl, with no QD present. In both experiments, the excitation conditions were the same as in the enhancement experiment (Fig. 5.2 in the main text).

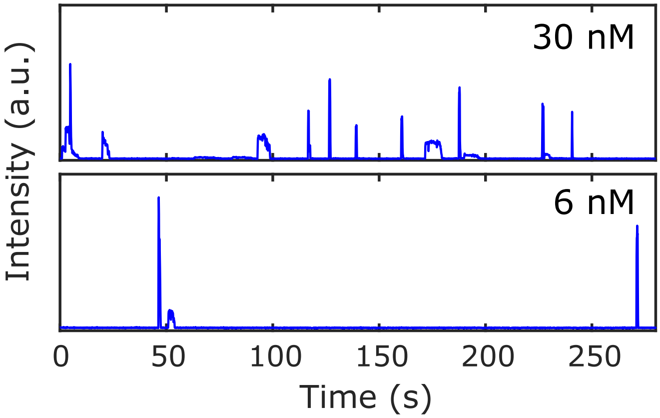

Figure S5.4: Timetraces recorded on the same gold nanorod at two different QD concentrations (6 nM and 30 nM). The timetrace for 30 nM is shifted for clarity. The excitation is 1.55 kW/cm^2 at 775 nm.

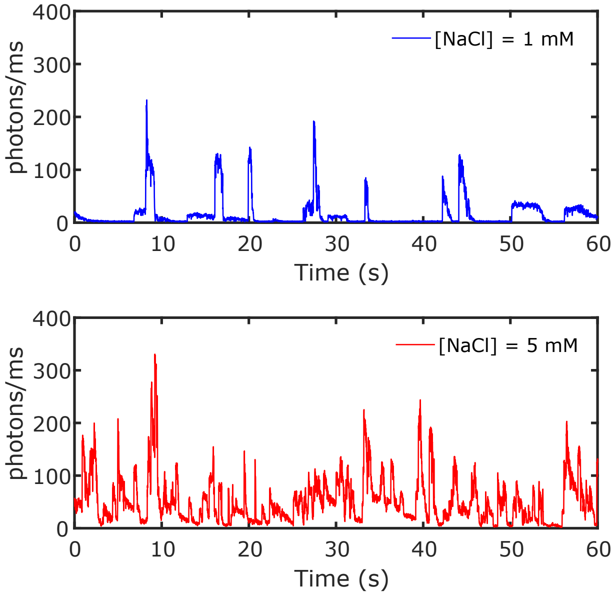

Figure S5.5: Enhanced time traces of QDs by gold nanorods at different concentrations of NaCl. Top 1 mM, bottom 5 mM.

5.5.6. One-photon luminescence decay of quantum dots

To measure the complete luminescence decay, an aqueous solution of 150 nM Qdot 655 and 3 mM NaCl was excited by a picosecond diode laser (Power Technology, Little Rock, AR, USA) with a wavelength of 635 nm and a repetition rate of 1 MHz. The emission was detected by an avalanche photodiode (SPCM AQRH-15, Perkin Elmer Inc., USA) and counted by a TCSPC card (PicoHarp 300, PicoQuant GmbH, Berlin, Germany). Figure S5.6 shows at the top the PL decay of the sample over a time window of 1 μs, along with the impulse response function of our system. We observe a non-exponential decay, commonly reported in the literature for quantum dots and usually attributed to the size distribution [39, 46], blinking and environmental fluctuations [44, 45, 52].

In order to model this behavior we used a stretched exponential [45]

$$f(\tau) = A\exp\Big[\big(-\tau/\tau_0\big)^{\beta}\Big],$$

and, alternatively, three exponentials

$$g(\tau) = w_1 e^{-\tau/\tau_1} + w_2 e^{-\tau/\tau_2} + (1 - w_1 - w_2) e^{-\tau/\tau_3}$$

to fit the decay. We also show both fits in Fig. S5.6. For the stretched exponential we obtained a $\tau_0 = 1.51$ ns and an exponent $\beta = 0.39$, while for the three exponentials we obtained obtaining $\tau_1 = 1.5$ ns ($w_1 = 66.92\%$), $\tau_2 = 16.5$ ns ($w_2 = 25.06\%$), $\tau_3 = 46.2$ ns

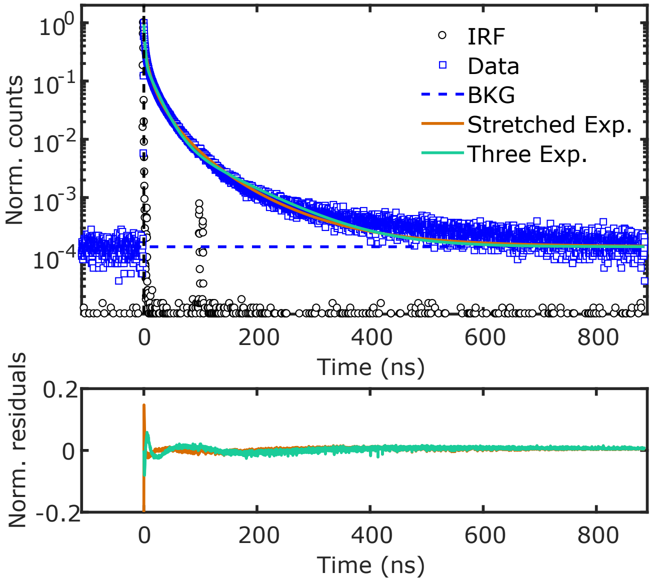

Figure S5.6: One-photon-excited luminescence decay curve of Qdot 655 diluted in water (150 nM). Top: decay data from QDs (blue squares) and IRF (black circles). The vertical dashed line shows $t = 0$ s while the horizontal dashed line represents the background signal. The fits for stretched exponential and three exponentials are also shown. Bottom: residuals from the fits with the same color code used on top.

($w_3 = 8.02\%$). Note that our curves are normalized to get a unity value at zero time and the percentage amplitudes in brackets correspond to the percentage weight of each exponential.

For the stretched exponential model, we calculated the average lifetime by [45]

$$\langle \tau \rangle = \frac{\tau_0}{\beta}\Gamma\left(\frac{1}{\beta}\right) = 5.09 \text{ ns}$$

where Γ represents the gamma function.

For the three-exponential model, we calculated different probabilities of the three QD forms according to the two models presented in the main text.

In model 1, the probabilities of the three forms are just proportional to the initial fluorescence intensity w_i, because their radiative rate is identical and thus initial intensities are proportional to the number of QDs. Thus we obtained an amplitude-weighted average lifetime of 8.88 ns by

$$\langle \tau_{\text{amp}} \rangle = \sum_i w_i \tau_i.$$

In model 2, because the quantum yield is the same for all three populations of QDs, these populations are proportional to the total number of photons emitted, corresponding to new weights $W_i = w_i\tau_i / \sum_j w_j \tau_j$. We obtained $W_1 = 11.54\%, W_2 = 46.68\%, W_3 = 41.78\%$. Thus we obtained an intensity-weighted average lifetime of 27.22 ns by

$$\langle \tau_{\text{int}} \rangle = \sum_i W_i \tau_i.$$

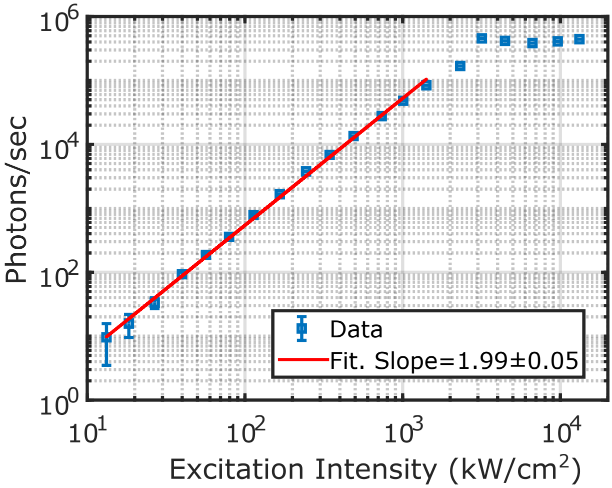

Figure S5.7: Two-photon-excited photoluminescence signal from an aqueous solution of Qdot 655 doped with 3 mM NaCl as a function of the excitation intensity at the center of the focused excitation volume. The curve deviates from the intensity-square relation at high intensities, indicating an excitation saturation threshold of $\sim$ 3000 kW/cm^2.

QDs quantum yield

We measured the ensemble quantum yield (QY) of the quantum dots using a fluorometer and obtained 0.80 $\pm$ 0.05. The quantum yield η_i of each component i is

$$\eta_i = \frac{k_{ri}}{k_{ri} + k_{nri}} = \tau_i k_{ri}$$

where k_r and k_{nr} represents the radiative and non-radiative rates and τ_i is the lifetime for each component. For model 1, with $\eta_3 = 1$ we can calculate the average quantum yield as

$$\langle \eta \rangle = \sum_i w_i \eta_i,$$

and obtained a value of $\langle \eta \rangle = 0.19$. For model 2, the average quantum yield is obviously unity. Thus, the two extreme models give upper and lower bounds to the expected experimental values.

5.5.7. Excitation saturation

We performed a power dependence study of the collected luminescence of a solution of QD in the same conditions as the enhancement experiment. This time we increased the excitation intensity until we found the saturation value (Fig. S5.7). We find that the saturation occurs at $\sim$ 3000 kW/cm^2, which is $\sim$ 2000 times higher than the intensity used for the enhancement experiments.

5.5.8. Enhancement factor simulations

The excitation enhancement was calculated with a finite-element method using Comsol Multiphysics. The near-field intensity maps of single gold nanorods with resonance wavelengths ranging from 711 to 824 nm in water were calculated. The resonance wavelengths were tuned by changing the length while keeping a constant diameter of 38 nm. The dielectric permitivity for gold was taken from Johnson and Christy [53], and the refractive index of the ambient medium was taken as 1.33. The theoretical excitation enhancement E_{exc} for two-photon absorption is the squared ratio of local field intensities with and without the nanorod, $E_{\mathrm{exc}} = I^2/I_0^2$, at the emitter's position.

We used a boundary element method (SCUFF-EM) to evaluate the modifications of decay rates and emission enhancement using a classical electrodynamics approach [54, 55]. For simplicity, a QD was modeled as a radiating point dipole ($\mathbf{p}_0$) oscillating at a frequency of ω, which corresponds to the emission wavelength of the QD.

The time-average power radiated by a QD in a medium is

$$P_{\mathrm{r0}}(\omega) = \frac{|\mathbf{p}_0|^2}{4\pi\varepsilon_0}\frac{n\omega^4}{3c^3},$$

where n is the relative index of the medium, c is the speed of light and ε_0 is the vacuum permittivity. In the vicinity of a nanoantenna, however, both the radiative and nonradiative decay rates are modulated by coupling to the plasmonic modes. The radiative rate enhancement factor (E_{rad}) due to resonant Purcell enhancement can be calculated as the ratio of the total radiated power by the emitter-antenna system (P_{rad}) and the power radiated by an isolated emitter (P_{r0}):

$$E_{\mathrm{rad}} = k_{\mathrm{r}}/k_{\mathrm{r}}^0 = P_{\mathrm{rad}}/P_{\mathrm{r0}},$$

where k_{r} and k_{r}^0 are the radiative decay rates with and without the antenna, respectively. Likewise, the additional nonradiative rate (K_{nr}) due to the dissipative losses inside the metal is derived from the power absorbed by the nanorod (P_{abs}):

$$K_{\mathrm{nr}}/k_{\mathrm{r}}^0 = P_{\mathrm{abs}}/P_{\mathrm{r0}}.$$

In the simulation, P_{abs} was calculated by integrating the time-averaged Poynting flux over the nanorod surface, which was modeled as a spherically capped cylinder. The sum of P_{rad} and P_{abs} was calculated as [56]

$$P_{\mathrm{rad}}(\omega) + P_{\mathrm{abs}}(\omega) = \frac{\omega^3}{2c^2\varepsilon_0}|\mathbf{p}_0|^2\left[\mathbf{n}\cdot\mathrm{Im}[\mathbf{G}(\mathbf{r},\mathbf{r};\omega)]\cdot\mathbf{n}\right],$$

where $\mathbf{G}(\mathbf{r},\mathbf{r};\omega)$ is the Green tensor at the emitter's position $\mathbf{r}$, $\mathbf{n}$ the unit vector in the direction of the dipole moment. The emission enhancement factor can be written as

$$E_{\mathrm{em}} = \frac{\eta}{\eta_0} = \frac{E_{\mathrm{rad}}}{\eta_0\big(E_{\mathrm{rad}} + K_{\mathrm{nr}}/k_{\mathrm{r}}^0 + 1/\eta_0 - 1\big)} \approx \frac{E_{\mathrm{rad}}}{\eta_0\big(E_{\mathrm{rad}} + K_{\mathrm{nr}}/k_{\mathrm{r}}^0\big)},$$

where η and η_0 are the quantum yield of the emitter with and without the antenna, respectively. E_{em} is proportional to the inverse of the emitter's intrinsic quantum yield for a given

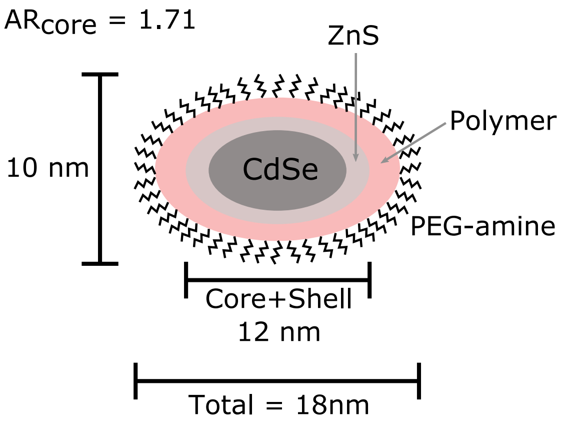

Figure S5.8: Scheme of the QDs used for the study.

emitter-antenna configuration, but independent of its intrinsic lifetime. Due to emission enhancement, the luminescence lifetime of the emitter is shortened:

$$\tau/\tau_0 = \eta_0^{-1}\big(E_{\mathrm{rad}} + K_{\mathrm{nr}}/k_{\mathrm{r}}^0 + 1/\eta_0 - 1\big)^{-1} \approx \eta_0^{-1}\big(E_{\mathrm{rad}} + K_{\mathrm{nr}}/k_{\mathrm{r}}^0\big)^{-1}.$$

In the calculation of E_{rad} and K_{nr}, it was assumed that the point dipole is placed along the long axis of the nanorod with a certain distance from the tip, and all the results were averaged over the actual luminescence spectrum of the QD. Unlike a fluorescent molecule, an elongated QD has three dipolar axis, where two are degenerated. Therefore, we simulated both orientations, parallel (‖) and perpendicular (⊥) and averaged the results using $1/3(\| + 2\perp)$.

We modeled the three components with lifetimes τ_i $(i = 1, 2, 3)$ independently using the above approach and then averaged the results using the weights w_i obtained from the fit of the natural lifetime decay (Fig. S5.6). We used two extreme models to assign the quantum yield of each component. In model 1 we assume that the radiative rate of all the components is the same and we assigned a unity quantum yield to the longest component. In model 2 we assigned unity quantum yield to the three components.

5.5.9. Quantum dot structure

For our study we used commercial quantum dots from Invitrogen (Qdot 655 ITK amino-PEG). They have a core-shell structure of CdSe/ZnS with a rod-like shape. The length and width are 12 nm and 7 nm, respectively, giving an aspect ratio of 1.71. It is further coated with an amphiphilic polymer shell to enable conjugation of amine-derivatized polyethylene glycol (PEG). Figure S5.8 shows a scheme of the QDs. The last layer of PEG-amine is about 2-nm thick.

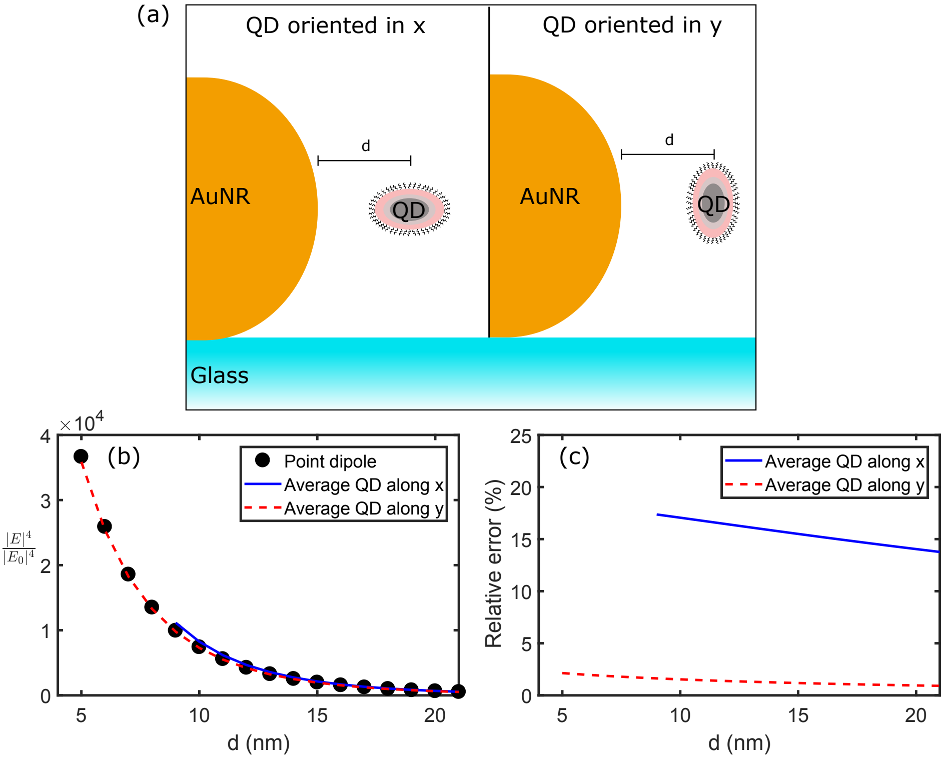

Figure S5.9: (a) Scheme of the average procedure. (b) Excitation enhancement for a point dipole and the averaged values for the two situations described on top. (c) Relative error

5.5.10. Effect of finite size of the quantum dot

In order to take into account the finite size of the QD we averaged the near-field map over the dimensions of the QD core. Figure S5.9(a) shows a scheme for the two situations taken into account: the quantum dot oriented along the longitudinal axis of the nanorod (x) and along the transverse axis (y). Figure S5.9(b) shows the resulting curves with the presented notation. The point dipole approximation gives rise to an error smaller than 20% in all cases.

References

[1] K. Kneipp, H. Kneipp, I. Itzkan, R. R. Dasari, and M. S. Feld, *Ultrasensitive chemical analysis by raman spectroscopy,* Chemical Reviews **99**, 2957 (1999).

[2] J. F. Li, Y. F. Huang, Y. Ding, Z. L. Yang, S. B. Li, X. S. Zhou, F. R. Fan, W. Zhang, Z. Y. Zhou, D. Y. Wu, B. Ren, Z. L. Wang, and Z. Q. Tian, *Shell-isolated nanoparticle-enhanced raman spectroscopy,* Nature **464**, 392 (2010).

[3] R. Bardhan, N. K. Grady, J. R. Cole, A. Joshi, and N. J. Halas, *Fluorescence enhancement by au nanostructures: nanoshells and nanorods,* Acs Nano **3**, 744 (2009).

[4] O. L. Muskens, V. Giannini, J. A. Sanchez-Gil, and J. Gomez Rivas, *Strong enhancement of the radiative decay rate of emitters by single plasmonic nanoantennas,* Nano Letters **7**, 2871 (2007).

[5] F. Tam, G. P. Goodrich, B. R. Johnson, and N. J. Halas, *Plasmonic enhancement of molecular fluorescence,* Nano Letters **7**, 496 (2007).

[6] G. Boyd, T. Rasing, J. Leite, and Y. Shen, *Local-field enhancement on rough surfaces of metals, semimetals, and semiconductors with the use of optical second-harmonic generation,* Physical Review B **30**, 519 (1984).

[7] A. Bouhelier, M. Beversluis, A. Hartschuh, and L. Novotny, *Near-field second-harmonic generation induced by local field enhancement,* Physical Review Letters **90**, 013903 (2003).

[8] S. Khatua, P. M. R. Paulo, H. Yuan, A. Gupta, P. Zijlstra, and M. Orrit, *Resonant plasmonic enhancement of single-molecule fluorescence by individual gold nanorods,* ACS Nano **8**, 4440 (2014).

[9] X. Li, F.-J. Kao, C.-C. Chuang, and S. He, *Enhancing fluorescence of quantum dots by silica-coated gold nanorods under one- and two-photon excitation,* Optics Express **18**, 11335 (2010).

[10] Y. Fu, J. Zhang, and J. R. Lakowicz, *Plasmon-enhanced fluorescence from single fluorophores end-linked to gold nanorods,* Journal of the American Chemical Society **132**, 5540 (2010).

[11] Z. Yang, W. Ni, X. Kou, S. Zhang, Z. Sun, L.-D. Sun, J. Wang, and C.-H. Yan, *Incorporation of gold nanorods and their enhancement of fluorescence in mesostructured silica thin films,* The Journal of Physical Chemistry C **112**, 18895 (2008).

[12] J. N. Farahani, D. W. Pohl, H.-J. Eisler, and B. Hecht, *Single quantum dot coupled to a scanning optical antenna: a tunable superemitter,* Physical Review Letters **95**, 017402 (2005).

[13] A. Kinkhabwala, Z. Yu, S. Fan, Y. Avlasevich, K. Müllen, and W. Moerner, *Large single-molecule fluorescence enhancements produced by a bowtie nanoantenna,* Nature Photonics **3**, 654 (2009).

[14] H. Kano and S. Kawata, *Two-photon-excited fluorescence enhanced by a surface plasmon,* Optics Letters **21**, 1848 (1996).

[15] J.-M. Jung, H.-W. Yoo, F. Stellacci, and H.-T. Jung, *Two-photon excited fluorescence enhancement for ultrasensitive DNA detection on large-area gold nanopatterns,* Advanced Materials **22**, 2542 (2010).

[16] N. J. Greybush, M. Saboktakin, X. Ye, C. Della Giovampaola, S. J. Oh, N. E. Berry, N. Engheta, C. B. Murray, and C. R. Kagan, *Plasmon-enhanced upconversion luminescence in single nanophosphor–nanorod heterodimers formed through template-assisted self-assembly,* ACS Nano **8**, 9482 (2014).

[17] Y. Xue, C. Ding, Y. Rong, Q. Ma, C. Pan, E. Wu, B. Wu, and H. Zeng, *Tuning plasmonic enhancement of single nanocrystal upconversion luminescence by varying gold nanorod diameter,* Small **13** (2017).

[18] H. Yuan, S. Khatua, P. Zijlstra, M. Yorulmaz, and M. Orrit, *Thousand-fold enhancement of single-molecule fluorescence near a single gold nanorod,* Angewandte Chemie International Edition **52**, 1217 (2013).

[19] A. Samanta, Y. Zhou, S. Zou, H. Yan, and Y. Liu, *Fluorescence quenching of quantum dots by gold nanoparticles: a potential long range spectroscopic ruler,* Nano Letters **14**, 5052 (2014).

[20] W. Wenseleers, F. Stellacci, T. Meyer-Friedrichsen, T. Mangel, C. A. Bauer, S. J. Pond, S. R. Marder, and J. W. Perry, *Five orders-of-magnitude enhancement of two-photon absorption for dyes on silver nanoparticle fractal clusters,* The Journal of Physical Chemistry B **106**, 6853 (2002).

[21] I. Cohanoschi, S. Yao, K. D. Belfield, and F. E. Hernández, *Effect of the concentration of organic dyes on their surface plasmon enhanced two-photon absorption cross section using activated au nanoparticles,* Journal of Applied Physics **101**, 086112 (2007).

[22] S. T. Sivapalan, J. H. Vella, T. K. Yang, M. J. Dalton, R. N. Swiger, J. E. Haley, T. M. Cooper, A. M. Urbas, L.-S. Tan, and C. J. Murphy, *Plasmonic enhancement of the two photon absorption cross section of an organic chromophore using polyelectrolyte-coated gold nanorods,* Langmuir **28**, 9147 (2012).

[23] T. Zhao, K. Yu, L. Li, T. Zhang, Z. Guan, N. Gao, P. Yuan, S. Li, S. Q. Yao, Q.-H. Xu, and G. Q. Xu, *Gold nanorod enhanced two-photon excitation fluorescence of photosensitizers for two-photon imaging and photodynamic therapy,* ACS Applied Materials & Interfaces **6**, 2700 (2014).

[24] A. M. Craciun, M. Focsan, L. Gaina, and S. Astilean, *Enhanced one- and two-photon excited fluorescence of cationic (phenothiazinyl)vinyl-pyridinium chromophore attached to polyelectrolyte-coated gold nanorods,* Dyes and Pigments **136**, 24 (2017).

[25] S. T. Sivapalan, J. H. Vella, T. K. Yang, M. J. Dalton, J. E. Haley, T. M. Cooper, A. M. Urbas, L.-S. Tan, and C. J. Murphy, *Off-resonant two-photon absorption cross-section enhancement of an organic chromophore on gold nanorods,* The Journal of Physical Chemistry Letters **4**, 749 (2013).

[26] T. Zhang, G. Lu, J. Liu, H. Shen, P. Perriat, M. Martini, O. Tillement, and Q. Gong, *Strong two-photon fluorescence enhanced jointly by dipolar and quadrupolar modes of a single plasmonic nanostructure,* Applied Physics Letters **101**, 051109 (2012).

[27] S.-H. Gong, S. Kim, J.-H. Kim, J.-H. Cho, and Y.-H. Cho, *Site-selective, two-photon plasmonic nanofocusing on a single quantum dot for near-room-temperature operation,* ACS Photonics **5**, 711 (2018).

[28] A. B. Taylor, A. M. Siddiquee, and J. W. M. Chon, *Below melting point photothermal reshaping of single gold nanorods driven by surface diffusion,* ACS Nano **8**, 12071 (2014).

[29] P. Zijlstra, J. W. Chon, and M. Gu, *White light scattering spectroscopy and electron microscopy of laser induced melting in single gold nanorods,* Physical Chemistry Chemical Physics **11**, 5915 (2009).

[30] W. Albrecht, T.-S. Deng, B. Goris, M. A. van Huis, S. Bals, and A. van Blaaderen, *Single particle deformation and analysis of silica-coated gold nanorods before and after femtosecond laser pulse excitation,* Nano Letters **16**, 1818 (2016).

[31] S. Link and M. A. El-Sayed, *Spectral properties and relaxation dynamics of surface plasmon electronic oscillations in gold and silver nanodots and nanorods,* The Journal of Physical Chemistry B **103**, 8410 (1999).

[32] M. Yorulmaz, S. Khatua, P. Zijlstra, A. Gaiduk, and M. Orrit, *Luminescence quantum yield of single gold nanorods,* Nano Letters **12**, 4385 (2012).

[33] K. Zhang, H. Chang, A. Fu, A. P. Alivisatos, and H. Yang, *Continuous distribution of emission states from single cdse/zns quantum dots,* Nano Letters **6**, 843 (2006).

[34] C. B. Talbot, R. Patalay, I. Munro, S. Warren, F. Ratto, P. Matteini, R. Pini, H. G. Breunig, K. Konig, A. C. Chu, G. W. Stamp, M. A. Neil, P. M. French, and C. Dunsby, *Application of ultrafast gold luminescence to measuring the instrument response function for multispectral multiphoton fluorescence lifetime imaging,* Optics Express **19**, 13848 (2011).

[35] A. A. Kinkhabwala, Z. Yu, S. Fan, and W. E. Moerner, *Fluorescence correlation spectroscopy at high concentrations using gold bowtie nanoantennas,* Chemical Physics **406**, 3 (2012).

[36] S. Khatua, H. Yuan, and M. Orrit, *Enhanced-fluorescence correlation spectroscopy at micro-molar dye concentration around a single gold nanorod,* Physical Chemistry Chemical Physics **17**, 21127 (2015).

[37] C. Galland, Y. Ghosh, A. Steinbrück, M. Sykora, J. A. Hollingsworth, V. I. Klimov, and H. Htoon, *Two types of luminescence blinking revealed by spectroelectrochemistry of single quantum dots,* Nature **479**, 203 (2011).

[38] C. Galland, Y. Ghosh, A. Steinbrück, J. A. Hollingsworth, H. Htoon, and V. I. Klimov, *Lifetime blinking in nonblinking nanocrystal quantum dots,* Nature Communications **3**, 908 (2012).

[39] X. Ma, H. Tan, T. Kipp, and A. Mews, *Fluorescence enhancement, blinking suppression, and gray states of individual semiconductor nanocrystals close to gold nanoparticles,* Nano Letters **10**, 4166 (2010).

[40] S. J. LeBlanc, M. R. McClanahan, M. Jones, and P. J. Moyer, *Enhancement of multiphoton emission from single cdse quantum dots coupled to gold films,* Nano Letters **13**, 1662 (2013).

[41] J. Yao, D. R. Larson, H. D. Vishwasrao, W. R. Zipfel, and W. W. Webb, *Blinking and nonradiant dark fraction of water-soluble quantum dots in aqueous solution,* Proceedings of the National Academy of Sciences of the United States of America **102**, 14284 (2005).

[42] M. Caldarola, B. Pradhan, and M. Orrit, *Quantifying fluorescence enhancement for slowly diffusing single molecules in plasmonic near fields,* The Journal of Chemical Physics **148**, 123334 (2018).

[43] A. Biebricher, M. Sauer, and P. Tinnefeld, *Radiative and nonradiative rate fluctuations of single colloidal semiconductor nanocrystals,* The Journal of Physical Chemistry B **110**, 5174 (2006).

[44] N. Amecke and F. Cichos, *Intermediate intensity levels during the emission intermittency of single CdSe/ZnS quantum dots,* Journal of Luminescence **131**, 375 (2011).

[45] G. Schlegel, J. Bohnenberger, I. Potapova, and A. Mews, *Fluorescence decay time of single semiconductor nanocrystals,* Physical Review Letters **88**, 137401 (2002).

[46] B. R. Fisher, H.-J. Eisler, N. E. Stott, and M. G. Bawendi, *Emission intensity dependence and single-exponential behavior in single colloidal quantum dot fluorescence lifetimes,* The Journal of Physical Chemistry B **108**, 143 (2004).

[47] G. S. He, K.-T. Yong, Q. Zheng, Y. Sahoo, A. Baev, A. I. Ryasnyanskiy, and P. N. Prasad, *Multi-photon excitation properties of cdse quantum dots solutions and optical limiting behavior in infrared range,* Optics Express **15**, 12818 (2007).

[48] M. Marrocco, *Two-photon excitation fluorescence correlation spectroscopy of diffusion for gaussian- lorentzian volumes,* The Journal of Physical Chemistry A **112**, 3831 (2008).

[49] A. Nagy, J. Wu, and K. M. Berland, *Observation volumes and γ-factors in two-photon fluorescence fluctuation spectroscopy,* Biophysical Journal **89**, 2077 (2005).

[50] D. R. Larson, W. R. Zipfel, R. M. Williams, S. W. Clark, M. P. Bruchez, F. W. Wise, and W. W. Webb, *Water-soluble quantum dots for multiphoton fluorescence imaging in vivo,* Science **300**, 1434 (2003).

[51] E. Zamir, P. H. Lommerse, A. Kinkhabwala, H. E. Grecco, and P. I. Bastiaens, *Fluorescence fluctuations of quantum-dot sensors capture intracellular protein interaction dynamics,* Nature Methods **7**, 295 (2010).

[52] P. Sher, J. Smith, P. Dalgarno, R. Warburton, X. Chen, P. Dobson, S. Daniels, N. Pickett, and P. O'Brien, *Power law carrier dynamics in semiconductor nanocrystals at nanosecond timescales,* Applied Physics Letters **92**, 101111 (2008).

[53] P. B. Johnson and R.-W. Christy, *Optical constants of the noble metals,* Physical Review B **6**, 4370 (1972).

[54] M. T. Homer Reid and S. G. Johnson, *Efficient Computation of Power, Force, and Torque in BEM Scattering Calculations,* ArXiv e-prints (2013), arXiv:1307.2966 [physics.comp-ph] .

[55] `http://homerreid.com/scuff-EM`.

[56] L. Novotny and B. Hecht, *Principles of nano-optics* (Cambridge University Press, 2012).

6

Plasmonic enhancement of molecular two-photon-excited fluorescence by individual gold nanorods

In this chapter, we demonstrate two-photon-excited fluorescence enhancement for an ensemble of Rhodamine 6G molecules. Our results show that due to the presence of a single gold nanorod, fluorescence of the molecules in the near field is enhanced, on average, by a factor of about 4,500 at best. The enhancement shows a strong dependence on the plasmon resonance of the nanorods, and is independent of the excitation laser intensity if the excitation is under the reshaping threshold of the nanorods.

6.1. Introduction

In Chapter 5, we have demonstrated large enhancement of two-photon-excited luminescence for single semiconductor quantum dots. This was possible largely thanks to the high two-photon absorption cross-sections of quantum dots. Organic dye molecules, however, have typically 3 orders of magnitude lower two-photon absorption cross-sections than quantum dots [1–3]. The sizes of molecules are much smaller ($\sim 1-3$ nm). This features a major advantage as fluorescent probes over bulky quantum dots, whose size can easily reach 20 nm with the chemical coatings for better biocompatibility. Smaller size leads lower effects on the motion, localization and interactions of tagged objects, which is highly desired for fluorescence correlation spectroscopy, single-molecule imaging, *etc*. For these reasons, it is highly desirable to enhance the two-photon-excited fluorescence of dye molecules.

The two-photon-excited fluorescence enhancement of fluorescent dyes has already been measured a number of times in ensemble, where under different conditions different enhancement factors were found [4–6]. In this chapter, we systematically studied the two-photon fluorescence enhancement of Rhodamine 6G by single gold nanorods. Our results show that molecules near a gold nanorod can be enhanced by a factor of 4,500, averaged over all the molecules in the near-field.

6.2. Experimental section

Materials. Spectroscopy grade methanol (99.9%) was purchased from Alfa Aesar. Rhodamine 6G was purchased from Eastman. Gold nanorods were from Nanopartz Inc. The longitudinal surface plasmon resonance (LSPR) of the nanorods was 770 nm as obtained from the UV-Vis spectrum (Fig. S6.1). Their average dimensions were 38 nm × 118 nm as obtained from the transmission electron microscopy image provided by the manufacturer. Gold nanorods were immobilized onto a microscope coverslip with a spin-coating method described elsewhere [7, 8]. The coverslip was mounted in a home-made sample holder, where the sample solutions can be added for further optical measurements. A second cover glass was placed immediately on top to prevent the evaporation of methanol.

Two-photon microscopy. Single-particle spectroscopy was performed on a same optical setup as described in Chapter 4. Briefly, we used a mode-locked titanium-sapphire laser (775 nm wavelength and 220 fs pulse width, Mira 900, Coherent) with circular polarization to excite fluorescence from the molecules in a home-built confocal microscope equipped with time-correlated single-photon counting (TCSPC) electronics (TimeHarp 200, PicoQuant GmbH, Berlin). A 612-nm shortpass filter was used in the detection path to reject most of the two-photon-excited luminescence signal from the gold nanorods. The plasmon resonance of each gold nanorod is determined by measuring the one-photon-excited photoluminescence spectrum in clean methanol excited by a 532-nm continuous-wave laser prior to the two-photon measurements. Apart from more commonly used scattering spectra, photoluminescence spectra have been proven and used as an alternative method of measuring the plasmon resonances [9, 10].

In order to characterize two-photon fluorescence enhancement, emission signals from three different experimental conditions have to be compared (see Fig. 6.1). (a) The femtosecond laser was focused on a single gold nanorod in clean methanol. Strong two-photon-

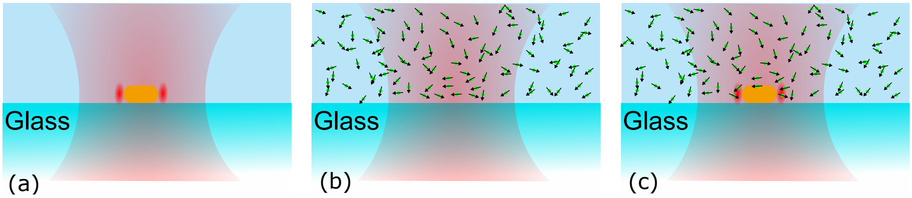

Figure 6.1: **Three measurements required to characterize the ensemble enhancement of Rhodamine 6G fluorescence**. (a) A single immobilized nanorod immersed in methanol. (b) Rhodamine 6G solution without a nanorod. (c) The same nanorod as in (a) immersed in the Rhodamine 6G solution.

excited luminescence signal from the nanorod was observed as a result of the strong two-photon absorption due to the resonant excitation of the surface plasmon [11–13], despite that only a small fraction of the emission was detected due to the 612-nm shortpass filter. See Chapter 4 for the optical characterizations of two-photon luminescence from gold nanorods. (b) Methanol was replaced by a solution of 5.34 mM Rhodamine 6G dissolved in methanol and the laser was focused on the solution/glass interface. (c) The laser was then parked on the same nanorod as in (a) but immersed in Rhodamine 6G solution. The laser power was the same for the three conditions. Time traces were recorded in time-tagged-time-resolved mode and further analyzed with SymPhoTime software (PicoQuant GmbH, Berlin).

6.3. Results and discussion

Figure 6.2(a) shows the time traces from the three measurements shown in Fig. 6.1 with an average laser power of 1.5 μW. Figure 6.2(b) shows the one-photon-excited luminescence spectrum of the nanorod shown in (a). A Lorentzian fit to the spectrum yields a plasmon resonance at 761.6 ± 0.3 nm and a full width at half maximum (FWHM) of 51.3 ± 0.7 nm. The narrow Lorentzian lineshape confirms that it is from a single gold nanorod. The spectrum has been normalized by the spectral response of the optical setup (see Chapter 2). The time traces show no higher fluctuations than the photon noise. Firstly, the laser power was kept below that required for photothermal reshaping of a gold nanorod [14–16] (see Chapter 5 for the discussion on nanorod reshaping), so the luminescence emission is stable. Secondly, fluorescence fluctuation due to molecules diffusing in and out of the confocal volume or the optical near field in the vicinity of the gold nanorod is not visible because of the high concentration of molecules. We measured the size of the focal volume by a separate experiment to be 0.09 ± 0.01 fL (See Fig. S4.2 in Chapter 4). We estimate $\sim$ 144,000 molecules in the upper half of the focal volume for a dye concentration of 5.34 mM. The size of the near field is $\sim$ 1000 times smaller than the half focal volume (denoted "far field" hereafter). The near field accommodates $\sim$ 144 molecules. We therefore do not expect any significant fluctuation of fluorescence in the time traces.

Excluding the dark count rate (64 ± 2 counts/s), the count rates from nanorod luminescence and unenhanced molecules in the far field were 778 ± 11 counts/s and 1820 ± 19 counts/s, respectively; the count rate from the nanorod in the Rhodamine 6G solution was 7140 ± 37 counts/s, which was higher than the sum of nanorod luminescence and

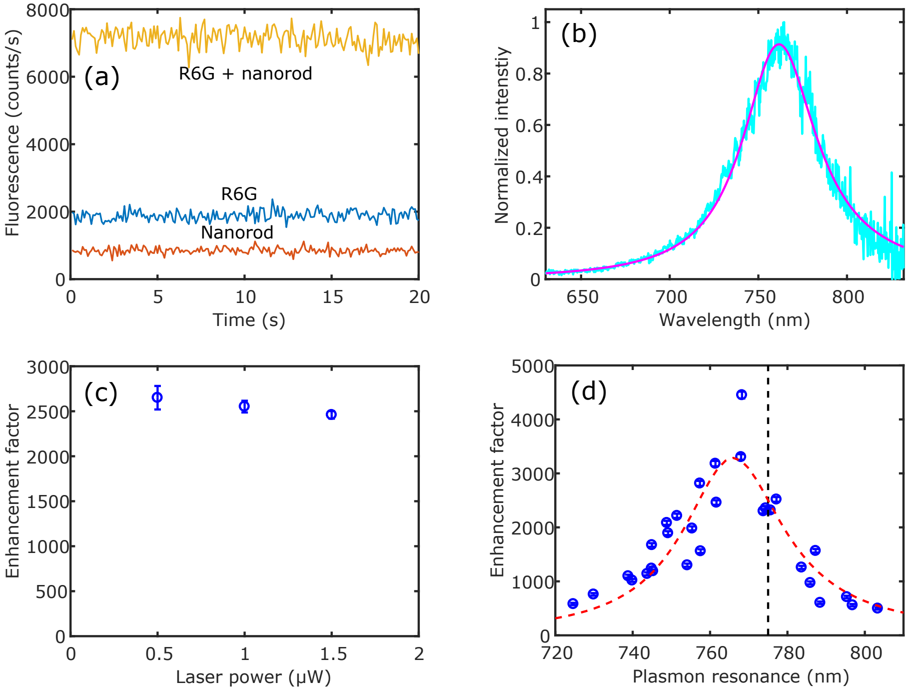

Figure 6.2: **Experimental results**. (a) Fluorescent time traces recorded on a nanorod in methanol (orange), Rhodamine 6G solution without a nanord (blue) and a nanorod in Rhodamine 6G solution (yellow). (b) The one-photon-excited luminescence spectrum of the nanorod shown in (a). The magenta solid curve represents a Lorentzian fit to the spectrum, which yields a plasmon resonance wavelength of 761.6 ± 0.3 nm and a full width at half maximum (FWHM) of 51.3 ± 0.7 nm. (c) Fluorescence enhancement factor as a function of the excitation laser power. (d) The blue circles represent the measured fluorescence enhancement factor as a function of the plasmon resonance of the single gold nanorods. The error bars are smaller than the circles representing the data points. The black dashed line shows the wavelength of the excitation laser (775 nm). The red dashed curve is a Lorentzian fit to the data, which yields a FWHM of 31.8 ± 5.6 nm.

molecule fluorescence when measured separately. (The mean values and uncertainties of photon counts were estimated by fitting the interphoton times to mono-exponentials without binning the photons.) The extra signal (4478 ± 43 counts/s) was from the molecules in the near field whose two-photon fluorescence was strongly enhanced by the gold nanorod. In other words, although the molecules in the plasmonic hotspot are 1000 times fewer in number than in the far field, they contribute to 2.46 ± 0.05 times higher count rate than all the molecules in the far field. This corresponds to an average enhancement factor of 2460 ± 50. We note this enhancement factor is a rough estimate since the volume of the near field is not well-defined.

It was previously reported that the high temperature of the electron gas (thousands of K) upon femtosecond excitation leads to the transient broadening of the plasmon resonance [17]. This broadening appears during the exciting pulse and might potentially hinder the efficiency of plasmonic effects, such as fluorescence enhancement. If this is the case, fluorescence enhancement should decrease with increasing excitation intensity. To address this point, we measured the fluorescence enhancement of Rhodamine 6G with varying average laser powers and the results are shown in Fig. 6.2(c). Measurements on four more different nanorods are presented in Fig. S6.4. We see that the enhancement factor does not show significant decrease with increasing power, suggesting that two-photon fluorescence enhancement is not notably affected by the plasmon broadening.

Fluorescence enhancement depends on the plasmon resonance wavelength of individual nanorods. With the plasmon resonance closer to the excitation wavelength, a nanorod creates a stronger near field intensity, hence higher fluorescence enhancement. We repeated the enhancement experiment for 29 more single nanorods and plotted the measured fluorescence enhancement factors in Fig. 6.2(d), which shows a clear plasmon resonance dependence. A maximum enhancement factor of 4,500 was achieved by a nanorod with a plasmon resonance wavelength of 768 nm, which is very close to the laser wavelength (775 nm). We fitted the enhancement factors to a Lorenzian function and obtained a full width at half maximum (FWHM) of 31.8 ± 5.6 nm, which is narrower than the typical linewidth of the plasmon resonance of a single gold nanorod ($\sim$ 50 nm, see Fig. 6.2(b)). The sharper dependence is consistent with the nonlinear nature of the two-photon-excited fluorescence enhancement.

6.4. Conclusion

By measuring on the same nanorod in different situations, we clearly and convincingly demonstrated two-photon-excited fluorescence enhancement for Rhodamine 6G by single gold nanorods. The enhancement strongly depends on the position of the plasmon resonances of the nanorods, and is independent of the excitation laser intensity if the excitation is under the reshaping threshold. We deduced a molecular enhancement factor of 4,500 averaged over the molecules in the near field of a nanorod in the best case.

6.5. Supporting information

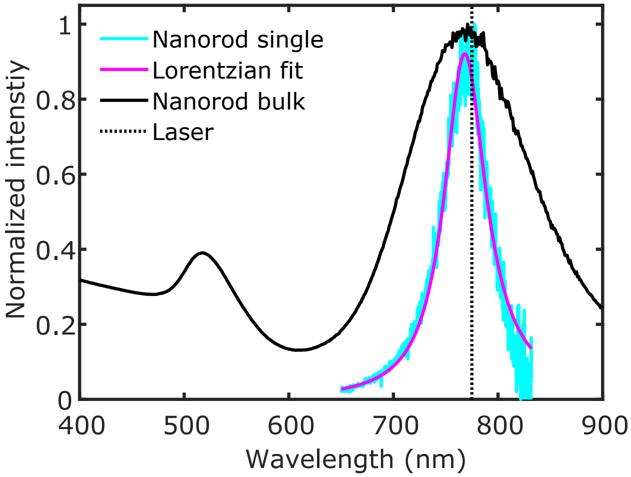

Figure S6.1: **Spectra of gold nanorods**. The black line shows the bulk extinction spectrum of gold nanorods used in this work dispersed in water. The extinction maximum was observed at 771 nm. The broad extinction band stems from the size distribution of nanorods in the suspension. The cyan curve shows the one-photon-excited photoluminescence spectrum of a single gold nanorod. The spectrum is corrected for the wavelength-dependence collecting efficiency of the setup and fitted with a Lorentzian line shape (magenta), yielding a resonance wavelength of 768.2 ± 0.3 nm. The wavelength of the excitation laser (775 nm) is represented by the dashed vertical lines in the plots.

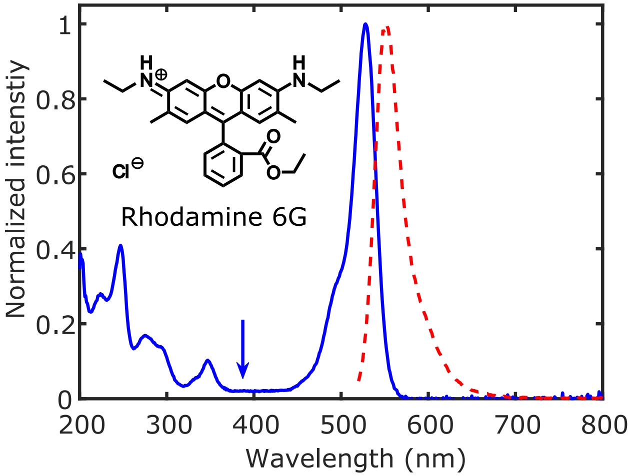

Figure S6.2: **Spectra of Rhodamine 6G**. Absorption and emission spectra of a solution of Rhodamine 6G in methanol are shown as the blue solid line and red dashed line, respectively ($\lambda_{\mathrm{max-abs}} \sim 528$ nm, $\lambda_{\mathrm{max-em}} \sim 552$ nm). The blue vertical arrow indicates the wavelength corresponding to the total energy of two excitation photons. Inset: chemical structure of Rhodamine 6G.

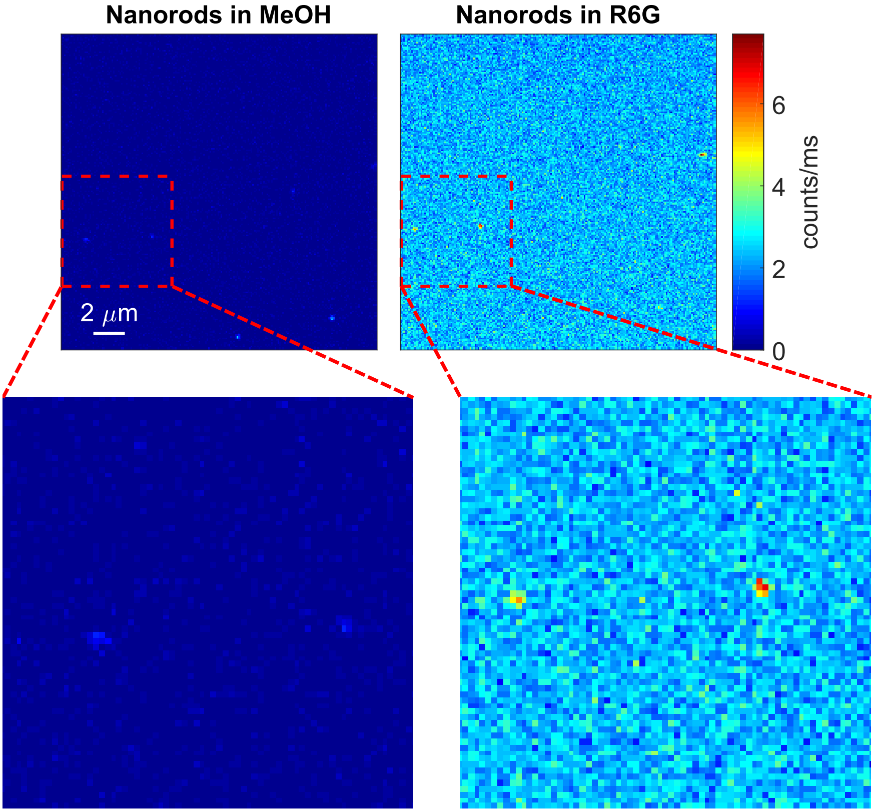

Figure S6.3: **Fluorescence images (20 μm × 20 μm) of gold nanorods in clean methanol (left) and Rhodamine 6G (right)**. The spots in the left image come from the two-photon-excited luminescence gold nanorods. After methanol was replaced by 5.34 mM Rhodamine 6G, the same nanorods shown in the left image were identified despite of the small drift. The images consist of 200 × 200 pixels with an integration time of 10 ms/pixel. An area of 7 μm × 7 μm containing two nanorods is expanded. The excitation was the femtosecond laser (circularly polarized) with an average power of 1.5 μW at the sample. A 612-nm short-pass filter was used for the images. Intensity enhancement is already visible by comparing of the brightness of the spots for the same nanorods in different images, but to measure the enhancement with more accuracy, we have to record time traces both on and outside nanorods.

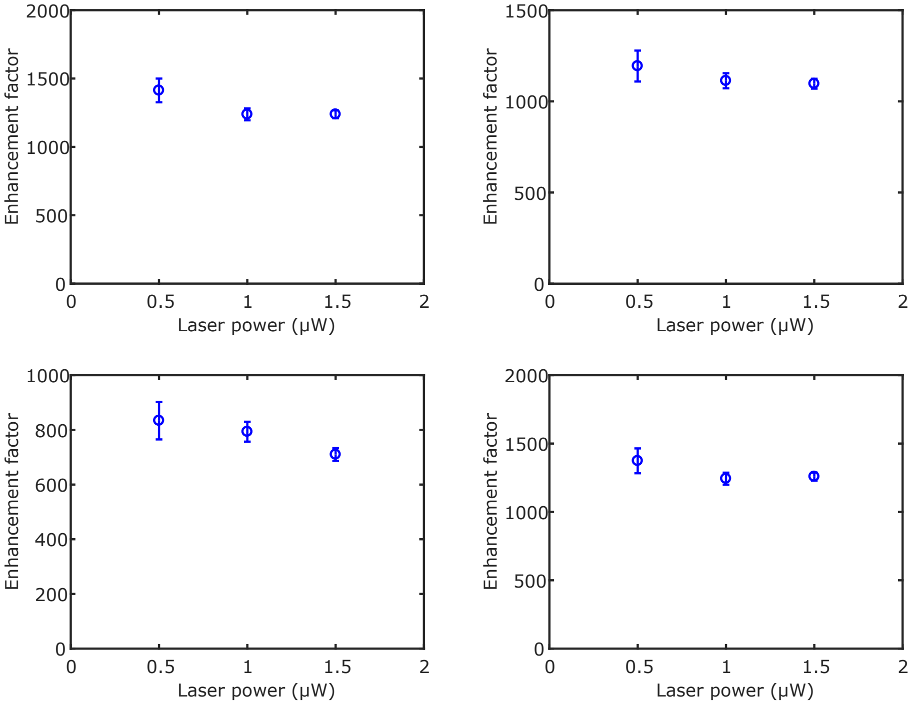

Figure S6.4: Power-dependent measurements of the enhancement factors for four more nanorods.

References

[1] M. A. Albota, C. Xu, and W. W. Webb, *Two-photon fluorescence excitation cross sections of biomolecular probes from 690 to 960 nm,* Applied Optics **37**, 7352 (1998).

[2] C. Xu and W. W. Webb, *Measurement of two-photon excitation cross sections of molecular fluorophores with data from 690 to 1050 nm,* JOSA B **13**, 481 (1996).

[3] D. R. Larson, W. R. Zipfel, R. M. Williams, S. W. Clark, M. P. Bruchez, F. W. Wise, and W. W. Webb, *Water-soluble quantum dots for multiphoton fluorescence imaging in vivo,* Science **300**, 1434 (2003).

[4] T. Zhao, K. Yu, L. Li, T. Zhang, Z. Guan, N. Gao, P. Yuan, S. Li, S. Q. Yao, Q.-H. Xu, and G. Q. Xu, *Gold nanorod enhanced two-photon excitation fluorescence of photosensitizers for two-photon imaging and photodynamic therapy,* ACS Applied Materials & Interfaces **6**, 2700 (2014).

[5] S. T. Sivapalan, J. H. Vella, T. K. Yang, M. J. Dalton, R. N. Swiger, J. E. Haley, T. M. Cooper, A. M. Urbas, L.-S. Tan, and C. J. Murphy, *Plasmonic enhancement of the two photon absorption cross section of an organic chromophore using polyelectrolyte-coated gold nanorods,* Langmuir **28**, 9147 (2012).

[6] I. Cohanoschi, S. Yao, K. D. Belfield, and F. E. Hernández, *Effect of the concentration of organic dyes on their surface plasmon enhanced two-photon absorption cross section using activated au nanoparticles,* Journal of Applied Physics **101**, 086112 (2007).

[7] H. Yuan, S. Khatua, P. Zijlstra, M. Yorulmaz, and M. Orrit, *Thousand-fold enhancement of single-molecule fluorescence near a single gold nanorod,* Angewandte Chemie International Edition **52**, 1217 (2013).

[8] W. Zhang, M. Caldarola, B. Pradhan, and M. Orrit, *Gold nanorod enhanced fluorescence enables single-molecule electrochemistry of methylene blue,* Angewandte Chemie International Edition **56**, 3566 (2017).

[9] M. Yorulmaz, S. Khatua, P. Zijlstra, A. Gaiduk, and M. Orrit, *Luminescence quantum yield of single gold nanorods,* Nano Letters **12**, 4385 (2012).

[10] A. Carattino, S. Khatua, and M. Orrit, *In situ tuning of gold nanorod plasmon through oxidative cyanide etching,* Phyical Chemistry Chemical Physics **18**, 15619 (2016).

[11] C. Molinaro, Y. El Harfouch, E. Palleau, F. Eloi, S. Marguet, L. Douillard, F. Charra, and C. Fiorini-Debuisschert, *Two-photon luminescence of single colloidal gold nanorods: Revealing the origin of plasmon relaxation in small nanocrystals,* The Journal of Physical Chemistry C **120**, 23136 (2016).

[12] N. Gao, Y. Chen, L. Li, Z. Guan, T. Zhao, N. Zhou, P. Yuan, S. Q. Yao, and Q.-H. Xu, *Shape-dependent two-photon photoluminescence of single gold nanoparticles,* The Journal of Physical Chemistry C **118**, 13904 (2014).

[13] P. Zijlstra, J. W. Chon, and M. Gu, *Five-dimensional optical recording mediated by surface plasmons in gold nanorods,* Nature **459**, 410 (2009).

[14] W. Albrecht, T.-S. Deng, B. Goris, M. A. van Huis, S. Bals, and A. van Blaaderen, *Single particle deformation and analysis of silica-coated gold nanorods before and after femtosecond laser pulse excitation,* Nano Letters **16**, 1818 (2016).

[15] P. Zijlstra, J. W. Chon, and M. Gu, *White light scattering spectroscopy and electron microscopy of laser induced melting in single gold nanorods,* Physical Chemistry Chemical Physics **11**, 5915 (2009).

[16] A. B. Taylor, A. M. Siddiquee, and J. W. M. Chon, *Below melting point photothermal reshaping of single gold nanorods driven by surface diffusion,* ACS Nano **8**, 12071 (2014).

[17] S. Link and M. A. El-Sayed, *Spectral properties and relaxation dynamics of surface plasmon electronic oscillations in gold and silver nanodots and nanorods,* The Journal of Physical Chemistry B **103**, 8410 (1999).

7

Conclusions and outlook

This thesis is a collection of experimental attempts to enhance photoluminescence of fluorescent molecules and quantum dots with single gold nanorods (GNRs) and relevant applications. Special attention is focused on the interactions between *single* emitters and GNRs. Investigation of single emitters provides direct information from each individual emitter, and thus reveals the characters and detailed processes of the microscopic components that are covered under the macroscopic behavior of the entirety in a conventional ensemble measurement. The first three chapters report enhancement of one-photon-excited fluorescence of single molecules. In the last two chapters, we investigate enhancement of two-photon-excited fluorescence/luminescence, which is much less studied in the literature. Every chapter includes its own conclusion. Here we summarize the important results of each chapter and discuss about open questions and prospects for future research.

Single-molecule fluorescence enhancement with DNA transient binding

Fluorescent dyes emitting at wavelengths in the near-infrared region are of particular interest for *in vivo* applications due to the absence of autofluorescence and deeper penetration depth. Unfortunately, however, most biocompatible near-infrared fluorescent dyes are weak emitters with fairly low quantum yield. It is thus quite challenging to image near-infrared dyes at the single-molecule level with conventional single-molecule fluorescence microscopy. In Chapter 2, we used gold nanorods with localized surface plasmon resonance (LSPR) in the near-infrared region to enhance the fluorescence of single molecules of a near-infrared dye. Nanorods with the LSPR in the near-infrared region often give rise to higher enhancement factors compared to nanorods resonating in the visible region because of stronger plasmon resonances and lower loss in the metal. In this chapter, we made use of the reversible hybridization of molecule-carrying short DNA oligomers to their complementary docking strands (transient binding) to visualize single-molecule enhancement events near individual GNRs. Complementary DNA strands offer the ability to bind the desired target molecule at the nanorod hot spot. When the fluorescence intensity of the dye molecules near a nanorod is monitored over time such events can be seen as signal bursts in the intensity trajectory.

Additionally, we found that hot electrons generated on the surface of plasmonic structures under focused continuous-wave (CW) laser irradiation are able to break the Au-S bond connecting the DNA oligomers and gold. This hot-electron effect was previously only observed with pulsed lasers.

DNA oligomer-based transient binding is a robust chemical approach that allows one to control the distance and binding time efficiently. Combined with plasmonic enhancement, a rich variety of single-molecule studies can be envisioned. We demonstrated observing fluorescence from refreshing molecules emitting at a fixed point near a nanorod. In such a situation, one can study fluorescence enhancement without the randomness caused by the inhomogeneity of the local electric field. For example, one can study the enhancement for molecules with different quantum efficiencies but placed at the same position with respect to the plasmonic nanoantenna.

Plasmonic hot electrons deteriorate the photostability of our enhancement experiments. However, interesting applications utilizing hot electrons have been demonstrated for controlled cargo release [1], to control the surface chemistry of nanoantennas with subdiffraction precision [2], and photocatalysis, to name a few. These possibilities were demonstrated mostly with the use of a femtosecond pulsed laser. If CW lasers can also generate hot electrons, as we demonstrated here, the application of hot electrons can be largely extended.

Single-molecule electrochemistry enabled by fluorescence enhancement

Chapter 3 shows that it is possible to observe the redox cycles of a single molecule in real time using fluorescence as the readout. We use single GNRs to enhance the fluorescence signal from single redox-sensitive Methylene Blue molecules so that the electrochemical properties of single molecules can be studied. By fixing a single molecule on the substrate near a GNR, we were able to record and quantify the redox-induced fluorescence blinking of the same molecule at different electrochemical potentials and thus determine the mid-point potential of the molecule. The observation time of a molecule is limited only by photobleaching.

Single molecules are local reporters inside a complex system. Our single-molecule electrochemical technique could be extended to chemical and biological systems to measure the local redox potential. At present, measurement should be performed in a system with a low pH value of 2 in order to match the mid-point potentials of the electron mediator and Methylene Blue. Future work would be to optimize the experimental design so that it works at physiological conditions before it can be applied in biological systems.

Single-molecule enhancement of hot-band absorption induced luminescence

In Chapter 4, we show that GNRs are able to enhance luminescence from hot-band absorption. Hot-band absorption induced luminescence shows an anti-Stokes shift with respect to the excitation wavelength. The anti-Stokes emission appears to be two-photon-excited fluorescence at the first glance considering the large two-photon absorption cross-section of the studied squaraine fluorophore [3, 4], but it is an one-photon process with a linear relation between emission intensity and excitation power. The anti-Stokes emission can be excited by both CW and femtosecond lasers, and the emission intensity is the same under the same excitation power. Moreover, we observed the exponential temperature-dependence of hot-band absorption.

Hot-band absorption is usually a process with low efficiency as the optical excitation has to start from a high vibration level at the ground state, which is not energetically favorable. In this chapter, we demonstrate the feasibility of enhancing anti-Stokes luminescence with plasmonic nanorods. A femtosecond laser was used in our study, but it should also work with a CW laser, and the same enhancement is expected. This is potentially valuable for fluorescence imaging as the low background benefiting from anti-Stokes emission can be obtained without implementation of costly two-photon microscopy instruments.

Two-photon-excited luminescence enhancement of single quantum dots

Two-photon-excited luminescence is particularly advantageous for imaging biological specimens since it offers reduced scattering, deep sample penetration, and intrinsic confocality. Two-photon excitation should lead to a higher excitation enhancement factor than one-photon excitation due to the quadratic dependence of the fluorescence intensity on the excitation intensity. However, it is more difficult to demonstrate (single-molecule) two-photon-excited fluorescence/luminescence enhancement as shape instability of GNRs upon ultrafast laser irradiation limits the excitation power, and thus the emission signal of fluorophores. This was a problem because if a nanorod is reshaped, the enhancement properties are weakened due to the strong dependence of the position of the LSPR on the shape of the nanorod. In Chapter 5, we successfully demonstrated 10^4 fold enhancement of two-photon-excited luminescence of *single* quantum dots. This was possible thanks to the larger two-photon absorption cross-sections of quantum dots, which are typically 10^3 times higher than organic molecules. The fair agreement between the experimentally obtained enhancement factor and numerical simulations using electromagnetic theory confirms that the transient broadening of the plasmonic resonance by femtosecond excitation is not a limiting factor for two-photon-excited luminescence enhancement by individual GNRs and an electromagnetic consideration is sufficient to describe the luminescence enhancement.

The study in this chapter paves the way for future studies of single-molecule-single-particle plasmonic enhancement of two-photon-excited luminescence. In perspective, GNRs can be used to enhance the two-photon-excited luminescence of I-III-VI_2 ternary quantum dots, whose quantum yields are often lower than 10%. I-III-VI_2 ternary quantum dots have attracted increasing attention as promising alternatives for toxic cadmium based II-IV quantum dots for their low toxicity and unique optical properties [5, 6]. Increasing the luminescence of cadmium-free quantum dots will extend their applications in many fields.

Two-photon-excited fluorescence enhancement of fluorescent molecules

Apart from enhancing quantum dots, it is also valuable to enhance the two-photon-excited fluorescence of organic dye molecules because of their small size as labeling probes. In Chapter 6, we circumvented the problem of nanorod reshaping by increasing the concentration of molecules, thus studied the enhancement effect of an ensemble of molecules near individual GNRs. Single-nanorod measurements allowed us to study systematically the dependence of fluorescence enhancement on the LSPRs of nanorods and the excitation power. The results further support that, at powers low enough to avoid reshaping, two-photon fluorescence enhancement is not notably affected by the plasmon broadening by femtosecond pulses.

Future work will be to push the current experiments to single molecules. To this end, due to the weak two-photon emission, a single molecule has to be tethered near a GNR to allow enough time to collect emission photons from the single molecule. A promising option is the DNA transient binding technique described in Chapter 2. The background from the luminescence of the GNR can be filtered out spectrally (by a band-pass filter) and temporally (luminescence of GNRs is much shorter-lived than fluorescent molecules). Improving the photothermal stability of GNRs by, for instance, silica coating [7, 8], could increase the reshaping power threshold and thus the photon counts of single molecules, allowing easier observation of two-photon-excited fluorescence enhancement.

This thesis shows the potential of GNRs for fluorescence enhancement. The next goal of the project is to extend plasmonic enhancement to even weaker emitters, such as lanthanide ions [9]. Two-photon excitation will be used to get access to fluorophores absorbing in the near UV, between 300 and 400 nm. We will use plasmon resonances at red wavelengths for the excitation enhancement, while maintaining the emission enhancement for the red luminescence. Plasmonic enhancement will potentially generalize single-molecule spectroscopy to even weaker emitters.

References

[1] A. M. Goodman, N. J. Hogan, S. Gottheim, C. Li, S. E. Clare, and N. J. Halas, *Understanding resonant light-triggered DNA release from plasmonic nanoparticles,* ACS Nano **11**, 171 (2016).

[2] S. Simoncelli, Y. Li, E. Cortés, and S. A. Maier, *Nanoscale control of molecular self-assembly induced by plasmonic hot-electron dynamics,* ACS Nano (2018).

[3] K. Podgorski, E. Terpetschnig, O. P. Klochko, O. M. Obukhova, and K. Haas, *Ultra-bright and stable red and near-infrared squaraine fluorophores for in vivo two-photon imaging,* PloS One **7**, e51980 (2012).

[4] S.-J. Chung, S. Zheng, T. Odani, L. Beverina, J. Fu, L. A. Padilha, A. Biesso, J. M. Hales, X. Zhan, K. Schmidt, A. Ye, E. Zojer, S. Barlow, D. J. Hagan, E. W. Van Stryland, Y. Yi, Z. Shuai, G. A. Pagani, J.-L. Brédas, J. W. Perry, and S. R. Marder, *Extended squaraine dyes with large two-photon absorption cross-sections,* Journal of the American Chemical Society **128**, 14444 (2006).

[5] P.-H. Chuang, C. C. Lin, and R.-S. Liu, *Emission-tunable CuInS2/ZnS quantum dots: structure, optical properties, and application in white light-emitting diodes with high color rendering index,* ACS Applied Materials & Interfaces **6**, 15379 (2014).

[6] T. Pons, E. Pic, N. Lequeux, E. Cassette, L. Bezdetnaya, F. Guillemin, F. Marchal, and B. Dubertret, *Cadmium-free CuInS2/ZnS quantum dots for sentinel lymph node imaging with reduced toxicity,* ACS Nano **4**, 2531 (2010).

[7] W. Albrecht, T.-S. Deng, B. Goris, M. A. van Huis, S. Bals, and A. van Blaaderen, *Single particle deformation and analysis of silica-coated gold nanorods before and after femtosecond laser pulse excitation,* Nano Letters **16**, 1818 (2016).

[8] C.-S. Chang and L. J. Rothberg, *Plasmon-enhanced photoconductivity in amorphous silicon thin films by use of thermally stable silica-coated gold nanorods,* Chemistry of Materials **27**, 3211 (2015).

[9] S. Akerboom, M. S. Meijer, M. A. Siegler, W. T. Fu, and E. Bouwman, *Structure, photo- and triboluminescence of the lanthanoid dibenzoylmethanates: HNEt3[Ln(dbm)4],* Journal of Luminescence **145**, 278 (2014).

Samenvatting

Dit proefschrift beschrijft een verzameling experimentele pogingen om de fotoluminescentie van fluorescerende moleculen en quantumdots te versterken met gouden nanostaafjes (gold nanorods oftewel GNR's), alsmede relevante toepassingen hiervan. Er is speciale aandacht besteed aan de interacties tussen individuele emitters en GNR's. Bestudering van een afzonderlijke emitter geeft directe informatie over deze emitter en onthult op deze manier de karakteristieken en gedetailleerde processen van microscopische componenten die schuilgaan onder het macroscopische gedrag van het geheel in een conventionele ensemblemeting. De eerste drie hoofdstukken beschrijven de versterking van één-foton geëxciteerde fluorescentie van individuele moleculen. In de laatste twee hoofdstukken bespreken we de versterking van twee-foton geëxciteerde fluorescentie/luminescentie, waaraan in de literatuur veel minder aandacht wordt besteed. Hieronder vatten we de belangrijkste resultaten per hoofdstuk samen en bespreken we de mogelijkheden voor vervolgonderzoek.

Fluorescerende kleurstoffen die licht uitzenden in het nabije infrarood zijn vooral interessant bij in vivo toepassingen vanwege de afwezigheid van autofluorescentie en een groter doordringend vermogen. Helaas zijn de meeste van deze biocompatibele kleurstoffen zwakke emitters met een laag quantumrendement. Daardoor is het moeilijk om deze stoffen op enkelmoleculair niveau met conventionele enkelmoleculaire fluorescentiemicroscopie in beeld te brengen. In **hoofdstuk 2** beschrijven we hoe we GNR's hebben gebruikt om de fluorescentie van individuele moleculen van een nabij-infrarode kleurstof te versterken. De 'plaatselijke oppervlakte plasmonische resonantie' (localized surface plasmon resonance oftewel LSPR) van deze GNR's ligt in het nabij-infrarode gebied. GNR's met hun LSPR in het nabij-infrarood hebben vaak een hogere versterkingsfactor dan GNR's die resoneren in het spectrum van zichtbaar licht vanwege sterkere plasmonische resonanties en minder verlies in het metaal. In dit hoofdstuk visualiseren we de fluorescentieversterking van individuele moleculen in de buurt van GNR's met behulp van de omkeerbare hybridisatie tussen molecuuldragende DNA-oligomeren en hun complementaire DNA-strengen (transiënte binding). Complementaire DNA-strengen bieden de mogelijkheid om het gewenste doelmolecuul te binden bij de hotspot van de GNR. Wanneer de fluorescentie-intensiteit van één van de kleurstofmoleculen in de buurt van een GNR als functie van de tijd wordt gemeten, zijn deze gebeurtenissen zichtbaar als intensiteitspieken. Daarnaast hebben we ontdekt dat de hete elektronen, die door gefocuste, continue (CW) laserbestraling gegenereerd worden aan het oppervlak van plasmonische structuren, de Au-S binding tussen de DNA-oligomeren en goud kunnen verbreken. Dit hete-elektroneffect was tot nu toe alleen waargenomen met pulslasers.

DNA oligomeer-gebaseerde transiënte binding is een robuuste chemische benadering om de afstand en bindingstijd op efficiënte wijze onder controle te houden. Gecombineerd met plasmonische versterking kan een grote variëteit aan enkelmoleculair onderzoek worden overwogen. We beschrijven hoe we fluorescentie van moleculen op een specifiek punt bij een GNR hebben geobserveerd. In een dergelijke situatie kan de fluorescentieversterking onderzocht worden zonder fluctuaties ten gevolge van inhomogeniteiten van het lokale elektrisch veld. Men zou bijvoorbeeld de fluorescentieversterking kunnen onderzoeken van moleculen met verschillende kwantumrendementen doch geplaatst op dezelfde positie ten opzichte van de plasmonische nano-antenne.

In **hoofdstuk 3** laten we zien dat het mogelijk is om de redoxcycli van een enkel molecuul real-time te observeren door de fluorescentie te meten. We hebben afzonderlijke GNR's gebruikt om het fluorescentiesignaal van individuele redoxgevoelige methyleenblauwmoleculen te versterken zodat de elektrochemische eigenschappen van individuele moleculen bestudeerd konden worden. Door een enkel molecuul in de buurt van een GNR te fixeren zijn we in staat geweest om het aan- en uitgaan van de redox-geïnduceerde fluorescentie vast te leggen en te kwantificeren, en daarmee de midpuntspotentiaal van het molecuul te bepalen. De observatietijd van een molecuul wordt alleen beperkt door 'fotobleken' (uitdoven).

Individuele moleculen zijn lokale boodschappers binnen een complex systeem. Onze enkelmoleculaire elektrochemische techniek zou uitgebreid kunnen worden naar chemische en biologische systemen voor het meten van de lokale redoxpotentiaal. Op dit moment moeten metingen worden uitgevoerd in een systeem met een pH waarde van 2, om de midpuntspotentiaal van de elektronmediator overeen te laten komen met die van het methyleenblauw. In de toekomst zou het experimentele ontwerp geoptimaliseerd moeten worden zodat het ook werkt in fysiologische omstandigheden en daarmee toegepast kan worden in biologische systemen.

In **hoofdstuk 4** laten we zien dat GNR's in staat zijn de luminescentie van hetebandabsorptie te versterken. Hetebandabsorptie-geïnduceerde luminescentie laat een anti-Stokesverschuiving zien ten opzichte van de excitatiegolflengte. Op het eerste gezicht lijkt de anti-Stokesemissie veroorzaakt te worden door twee-fotonexcitatie vanwege de grote twee-foton absorptiedwarsdoorsnede van het bestudeerde squaraine fluorofoor, maar in werkelijkheid is het een één-fotonproces met een lineair verband tussen emissie-intensiteit en excitatievermogen. De anti-Stokes emissie kan worden geëxciteerd door zowel CW- als femtosecondelasers en de emissie-intensiteit is gelijk bij een gelijk excitatievermogen. Daarnaast hebben we een exponentiële temperatuurafhankelijkheid van hetebandabsorptie waargenomen.

Normaal gesproken is hetebandabsorptie een proces met een laag rendement. Dat komt doordat de optische excitatie moet beginnen bij een hoog vibratieniveau in de grondtoestand, en dat is energetisch niet gunstig. In dit hoofdstuk demonstreren we de haalbaarheid van het versterken van anti-Stokes luminescentie met een plasmonische GNR. In ons onderzoek hebben we een femtosecondelaser gebruikt, maar het zou ook moeten werken met een CW laser waarbij een soortgelijke versterking mag worden verwacht. Dit kan waardevol zijn voor fluorescentiemicroscopie omdat de lage achtergrond van anti-Stokes emissie verkregen kan worden zonder gebruik te hoeven maken van kostbare twee-foton microscopen.

Twee-foton geëxciteerde luminescentie komt vooral van pas bij het afbeelden van biologische monsters vanwege de geringe verstrooiing, groot doordringend vermogen en intrinsieke confocaliteit. Twee-fotonexcitatie zou moeten leiden tot een hogere excitatieversterkingsfactor dan één-fotonexcitatie vanwege het kwadratische verband tussen het excitatievermogen en de fluorescentie-intensiteit. Het is echter moeilijker om (bij enkelmoleculaire) twee-fotongeëxciteerde fluorescentie- / luminescentieversterking te demonstreren, omdat vorminstabiliteit van GNR's bij ultrasnelle laserbestraling het excitatievermogen en daarmee het emissiesignaal van fluoroforen beperkt. Dit is een probleem omdat elke keer wanneer een GNR van vorm verandert, de versterkingseigenschappen verzwakken vanwege de sterke invloed van de positie van de LSPR op de vorm van de GNR. In **hoofdstuk 5** demonstreren we met succes een tienduizendvoudige versterking van twee foton-geëxciteerde luminescentie van individuele quantumdots. Dit is mogelijk geweest dankzij de grotere twee-foton absorptiedwarsdoorsneden van quantumdots, die meestal duizend keer hoger zijn dan die van organische moleculen. De redelijke overeenkomst tussen de experimenteel verkregen versterkingsfactor en numerieke simulaties met behulp van elektromagnetische modellen bevestigt dat de kortstondige verbreding van de plasmonische resonantie door femtoseconde-excitatie geen beperkende factor is voor twee-foton geëxciteerde luminescentieversterking door individuele GNR's en dat een elektromagnetisch model voldoende is om de luminescentieversterking te beschrijven.

Naast fluorescentieversterking van quantumdots is het ook waardevol om de fluorescentie van twee-fotonexcitatie van organische kleurstoffen te versterken vanwege hun kleine afmetingen voor gebruik als labelprobe. In **hoofdstuk 6** bespreken we hoe we het probleem van GNR-vervorming hebben omzeild door de concentratie van moleculen te verhogen, waardoor we het versterkingseffect van een ensemble van moleculen bij een GNR hebben kunnen bestuderen. Metingen aan een enkele GNR hebben het mogelijk gemaakt om de invloed van fluorescentieversterking op de LSPR's van GNR's en het excitatievermogen systematisch te bestuderen. Verder bevestigen de resultaten dat, bij vermogens laag genoeg om geen vervorming te laten optreden, de twee-foton fluorescentieversterking niet merkbaar wordt beïnvloed door de plasmonische verbreding door femtosecondepulsen.

Vervolgonderzoek zou zich kunnen richten op het terugschalen van de huidige experimenten tot enkelmoleculair niveau. Daartoe moet, vanwege de zwakke twee-fotonemissie, een enkel molecuul dichtbij een GNR worden vastgemaakt zodat er genoeg tijd is om emissiefotonen van het molecuul te detecteren. Een veelbelovende optie is de DNA-transiënte bindingstechniek die wordt beschreven in hoofdstuk 2. De achtergrond van de GNR-luminescentie kan zowel spectraal worden gefilterd (door een banddoorlaatfilter) als tijdgebonden (luminescentie van GNR's is veel kortstondiger dan van fluorescente moleculen). Het verbeteren van de fotothermische stabiliteit van GNR's door bijvoorbeeld silica coating, zou de vermogensdrempel waarbij vervorming optreedt kunnen verhogen, en daarmee het aantal getelde fotonen van individuele moleculen. Daardoor zou het eenvoudiger zijn om twee foton-geëxciteerde fluorescentieversterking te observeren.

Dit proefschrift toont het potentieel van GNR's voor fluorescentieversterking. Het volgende doel van het project is om de plasmonische versterking uit te breiden naar zwakkere emitters zoals lanthanide-ionen. Twee-fotonexcitatie zal worden gebruikt om toegang te krijgen tot fluoroforen die absorberen in het nabije UV, tussen 300 en 400 nm. We zullen plasmonische resonanties bij rode golflengtes gebruiken voor de excitatieversterking, terwijl de emissieversterking voor de rode luminescentie behouden blijft. Plasmonische versterking zal enkelmoleculaire spectroscopie in potentie beschikbaar maken voor nog zwakkere emitters.

Curriculum Vitæ

I was born on 4th February 1989 in Anhui Province, China. I obtained my BSc degree in Optical Science at China Jiliang University (Hangzhou, China) in 2011. I then enrolled in a master project at Zhejiang University in the same city under the supervision of Prof. Dr. Min Qiu. I obtained my master's degree in March 2014 with the thesis entitled "Research on the photothermal properties of metal nanoparticles". In July 2014, I was awarded a scholarship from the China Scholarship Council and started my Ph.D. in the single-molecule optics group at Leiden University under the supervision of Prof. Dr. Michel Orrit. During my Ph.D. I studied the enhancement of linear and nonlinear light emission of single molecules by gold nanorods.

List of Publications

10. **W. Zhang**, M. Caldarola, X. Lu, M. Orrit, *Plasmonic Enhancement of Two-Photon-Excited Luminescence of Single Quantum Dots by Individual Gold Nanorod*, under review.

9. **W. Zhang**, M. Caldarola, X. Lu, B. Pradhan, M. Orrit, *Plasmonic enhancement of a near-infrared fluorophore using DNA transient binding*, under review.

8. **W. Zhang**, M. Caldarola, B. Pradhan, M. Orrit, *Gold Nanorod-Enhanced Fluorescence Enables Single-Molecule Electrochemistry of Methylene Blue*, Angewandte Chemie International Edition **56**, 3566 (2017).

7. **W. Zhang**, Q. Li, L. Meng, M. Qiu, *Universal scaling behavior of the temperature increase of a heat nanoparticle on a substrate*, Journal of Nanophotonics **9**, 093046 (2015).

6. Z. Liu, Q. Li, **W. Zhang**, Y. Yang, M. Qiu, *Nanoscale Control of Temperature Distribution Using a Plasmonic Trimer*, Plasmonics **10**, 900 (2015).

5. K. Du, Q. Li, **W. Zhang**, M. Qiu, *Wavelength and thermal distribution selectable microbolometers based on metamaterial absorbers*, Photonics Journal, IEEE **7**, 6800908 (2015).

4. Q. Li, **W. Zhang**, H. Zhao, M. Qiu, *Photothermal enhancement in core-shell structured plasmonic nanoparticles*, Plasmonics **9**, 623 (2014).

3. **W. Zhang**, Q. Li, M. Qiu, *A plasmon ruler based on nanoscale photothermal effect*, Optics Express **21**, 172 (2013).

2. Q. Wang, H. Zhao, X. Du, **W. Zhang**, M. Qiu, Q. Li, *Hybrid photonic-plasmonic molecule based on metal/Si disks*, Optics Express **21**, 11037 (2013).

1. Q. Li, **W. Zhang**, H. Zhao, M. Qiu, *Two-dimensional Analysis Photothermal Properties in Nanoscale Plasmonic Waveguides for Optical Interconnect*, Journal of Lightwave Technology **31**, 4051 (2013).

Acknowledgements

In the last four years, I shared a lot of sweet memories with many people in the beautiful city of Leiden. Many people helped me do my research and fit into the daily life in the Netherlands. I would like to gladly express my gratitude here.

My supervisor Prof. Michel Orrit deserves a big part of the credit for kindly and patiently guiding me throughout my Ph.D. journey. He is always able to give me insightful ideas and practical instructions on my project. I feel honored to be able to work with him on the exciting field of single-molecule spectroscopy.

I am thankful to my copromotor, Dr. Martín Caldarola, who contributed significantly to all the chapters in the thesis. As an experienced researcher, he has taught me a lot of experimental skills as wells as scientific thoughts. Thank you for day-to-day discussion at work and for being a good friend outside work.

The experimental work would not have been possible without the contributions of the technical support people at the Leiden Institute of Physics. I would like to thank Henriëtte van Leeuwen for carefully handling so much paperwork, Harmen van der Meer for making mechanical components essential for the microscope, Peter van Veldhuizen and Arno van Amersfoort for fixing the electronics, Lionel Ndamba and Marcel Winter for maintaining an organized chemical lab, and Anne France Beker and Thomas Mechielsen for the instructions on the fabrication and characterization facilities.

I appreciate my students Dieuwertje Modder and Jessamy Mol's work during their master and bachelor projects that contributed to the two-photon part of the thesis. I thank Dr. Saumyakanti Khatua for guiding me in the lab at the beginning of my Ph.D. I thank Xuxing Lu for his contributions on the numerical simulations, which constitute a considerable part of the thesis. I am indebted to Dr. Xueyan Miao, who helped me a lot on sample preparation and other experiments. Her work on Prussian Blue and amylose did not finally find its way into this thesis. A special acknowledgement goes to Dr. Biswajit Pradhan for providing me gold nanorods as wells as numerous great suggestions on my experiments. His creative ideas contributed a lot to several chapters of this thesis. I thank many colleagues including Henk Snijders, Redmar Vlieg, Dr. Lei Hou, with whom I had fruitful discussion and fantastic time together. I specially thank Redmar Vlieg and Jeroen Rosier for the Dutch translation of the summary. I acknowledge the entire MoNOS group for always providing a perfect atmosphere for research. I thank all the members for the good company. I won't forget the discussion, coffee, barbecues, borrels, drinks and parties we had together! The list could go on and on; to all of you I say: thanks!

My gratitude should go beyond Ph.D. period. I am grateful to all the teachers during my career as a student. Every progress I made would not have happened without the knowledge they taught me. At the end, I would like to express my heartfelt thanks to my family for their continuous love and support. Yudan, it was your love and encouragement that made this dissertation possible and my life so wonderful. Thank you.